Photon Counting and Deep Learning in CT

Marc Kachelrieß

German Cancer Research Center (DKFZ)
Heidelberg, Germany
www.dkfz.de/ct

DEUTSCHES
KREBSFORSCHUNGSZENTRUM
IN DER HELMHOLTZ-GEMEINSCHAFT

Photon Counting CT

Indirect Conversion (Today) | Direct Conversion (Future)

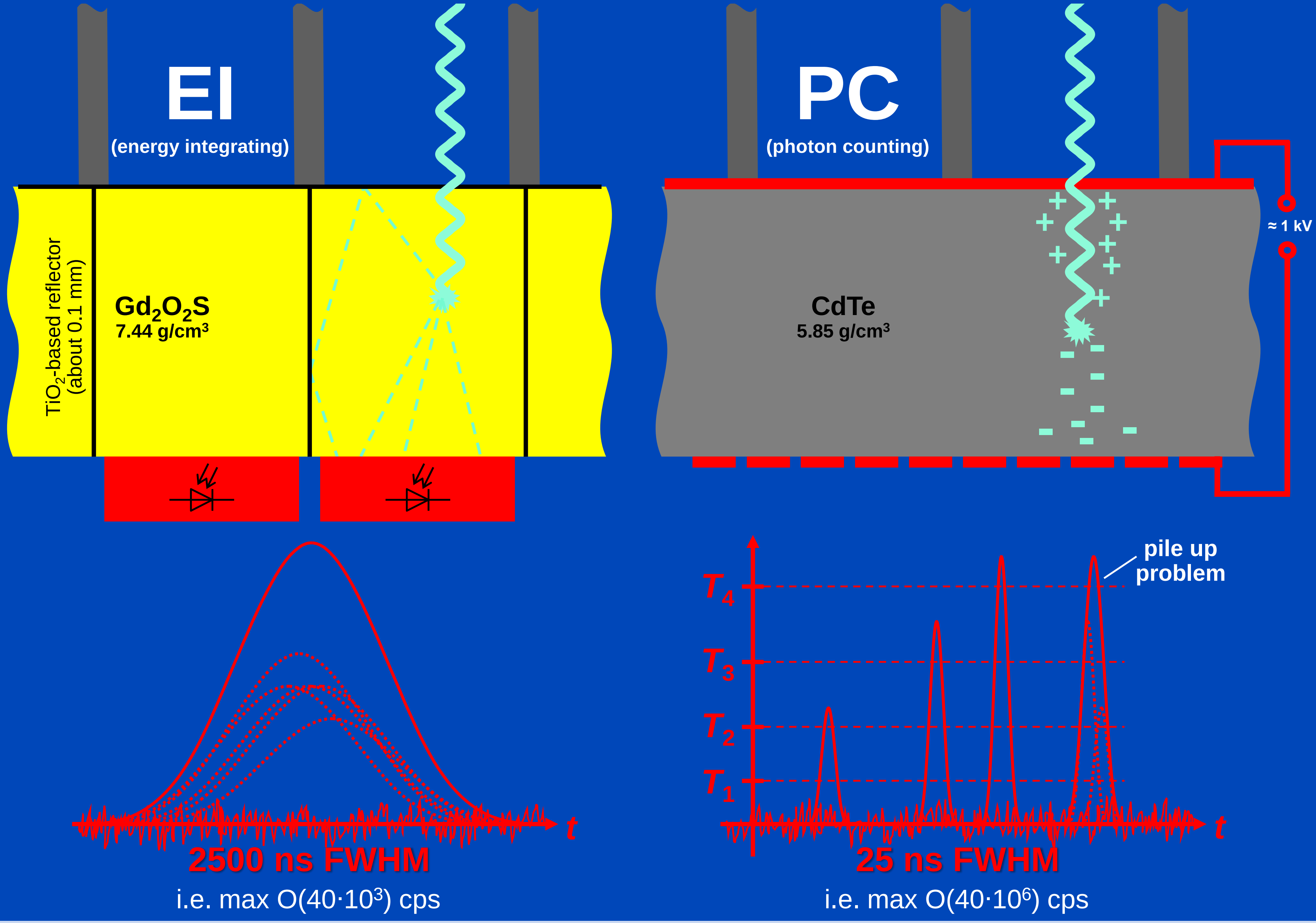

Requirements for CT: up to 10^9 x-ray photon counts per second per mm². Hence, photon counting only achievable for direct converters.

dkfz.

Energy-Selective Detectors: Improved Spectroscopy, Reduced Dose?

Ideally, bin spectra do not overlap, …

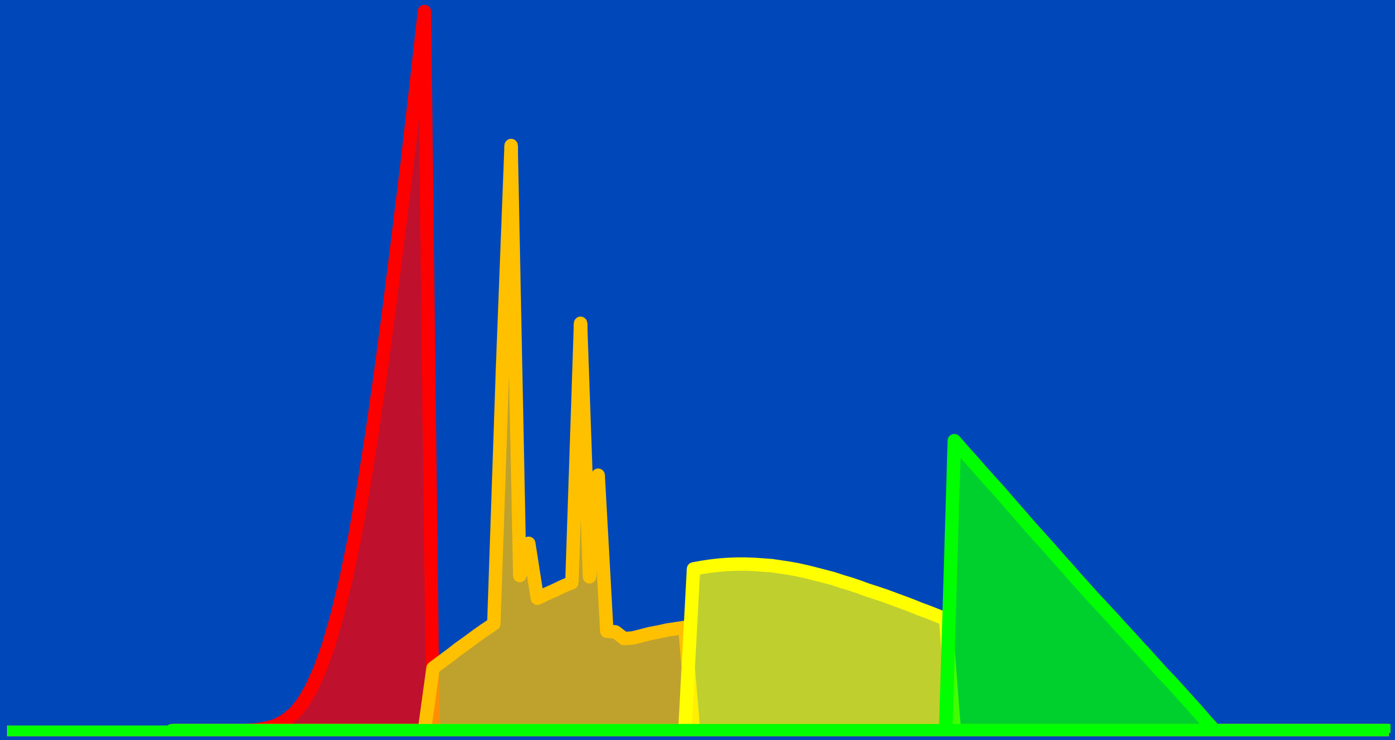

Spectra as seen after having passed a 32 cm water layer.

Energy-Selective Detectors: Improved Spectroscopy, Reduced Dose?

… realistically, however, they do!

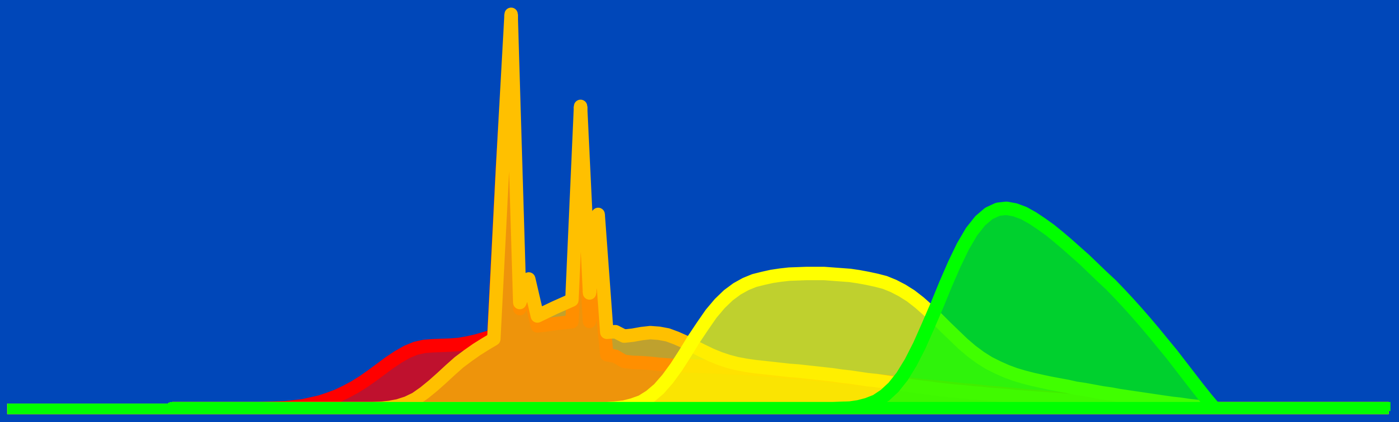

Spectra as seen after having passed a 32 cm water layer.

Photon Events

- Detection process in the sensor
- Photoelectric effect (e.g. 80 keV)

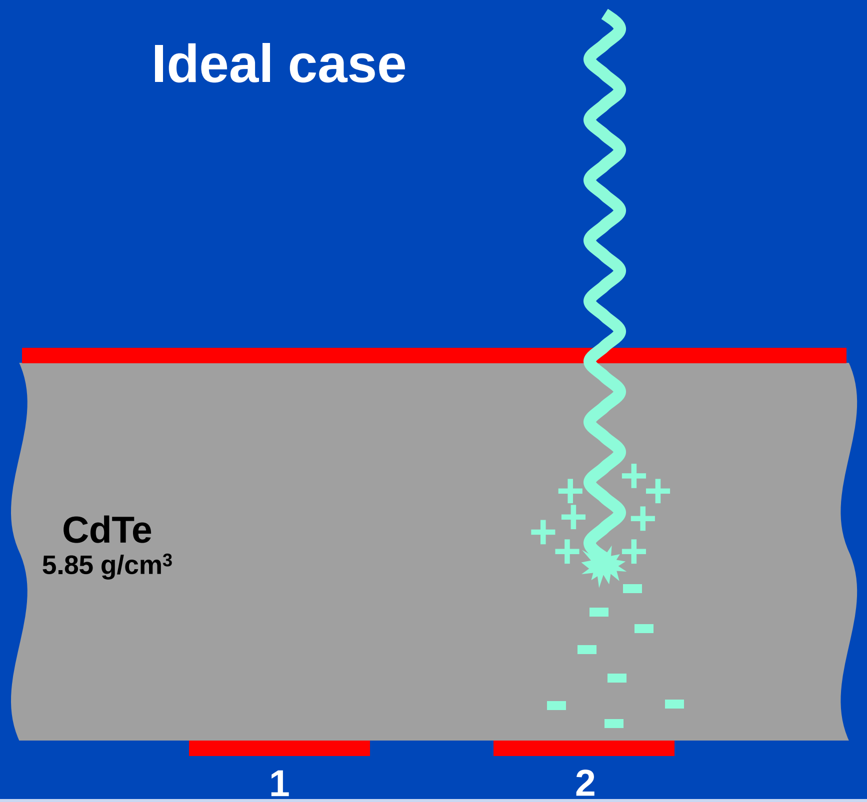

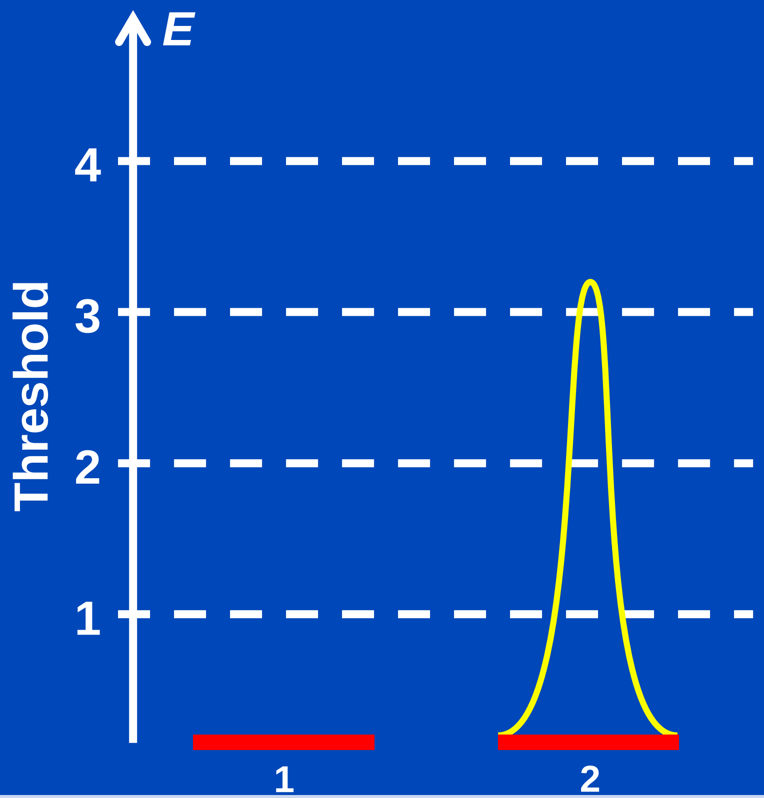

Photon Events

- Detection process in the sensor
- Compton scattering or K-fluorescence (e.g. 80 keV)

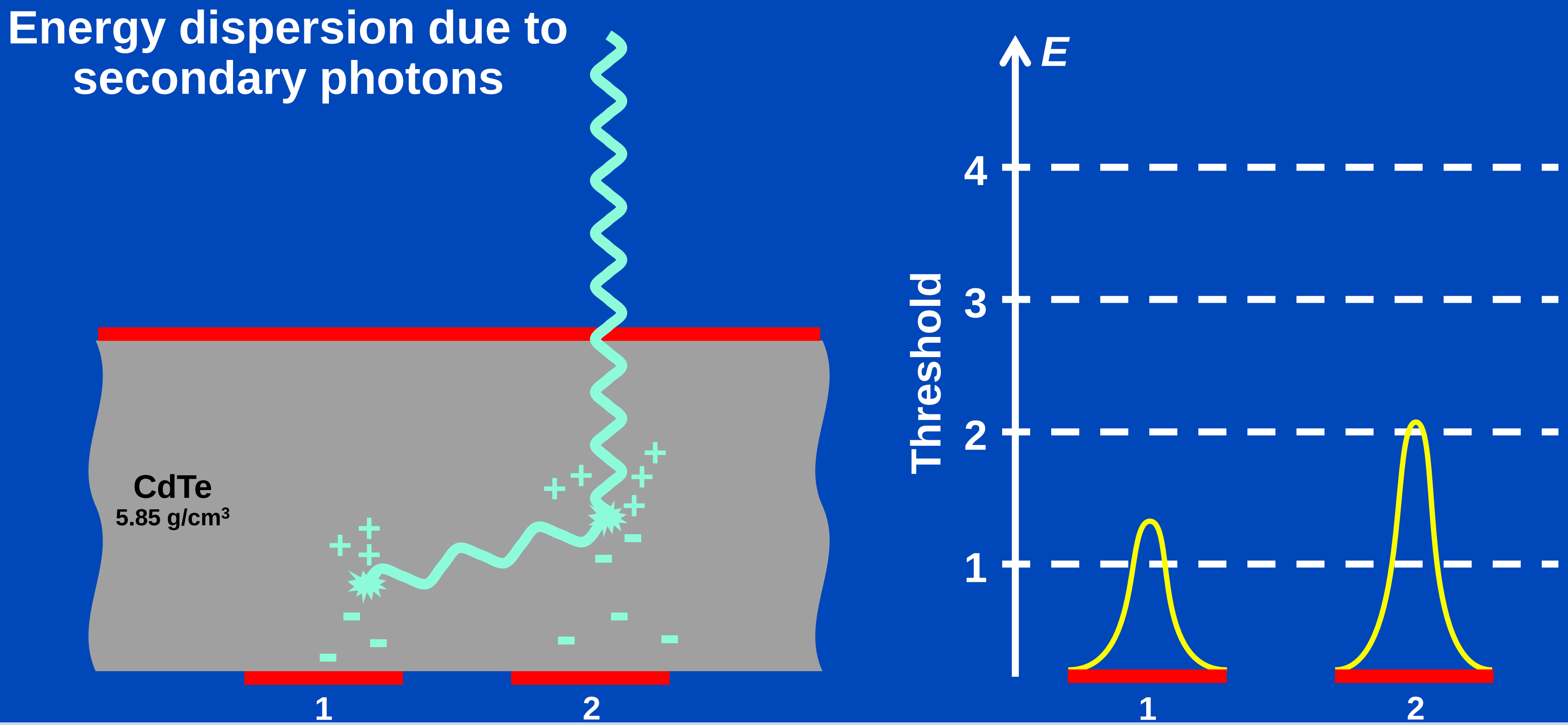

Photon Events

- Detection process in the sensor
- Photoelectric effect (e.g. 30 keV), charge sharing

Energy dispersion due to charge diffusion

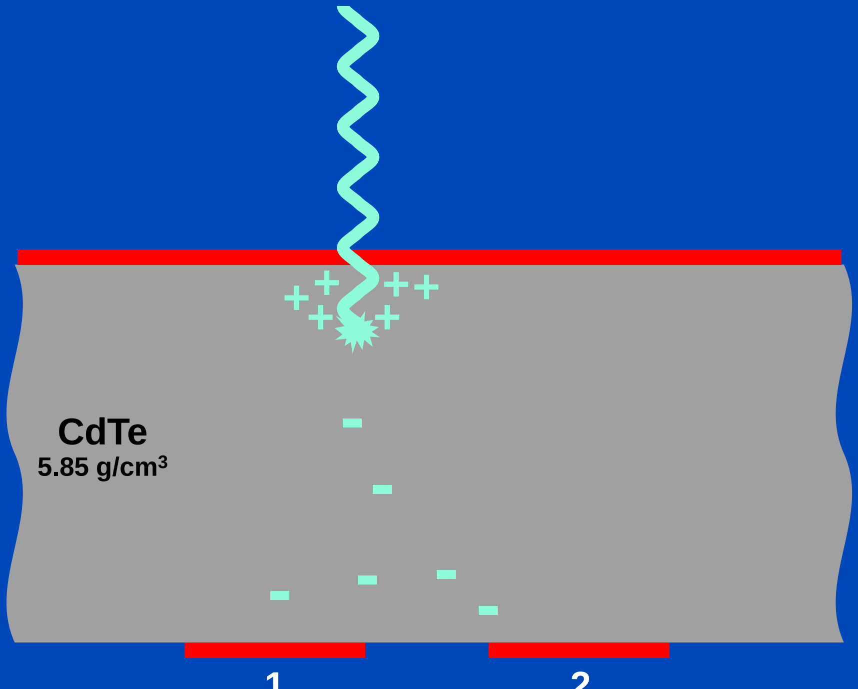

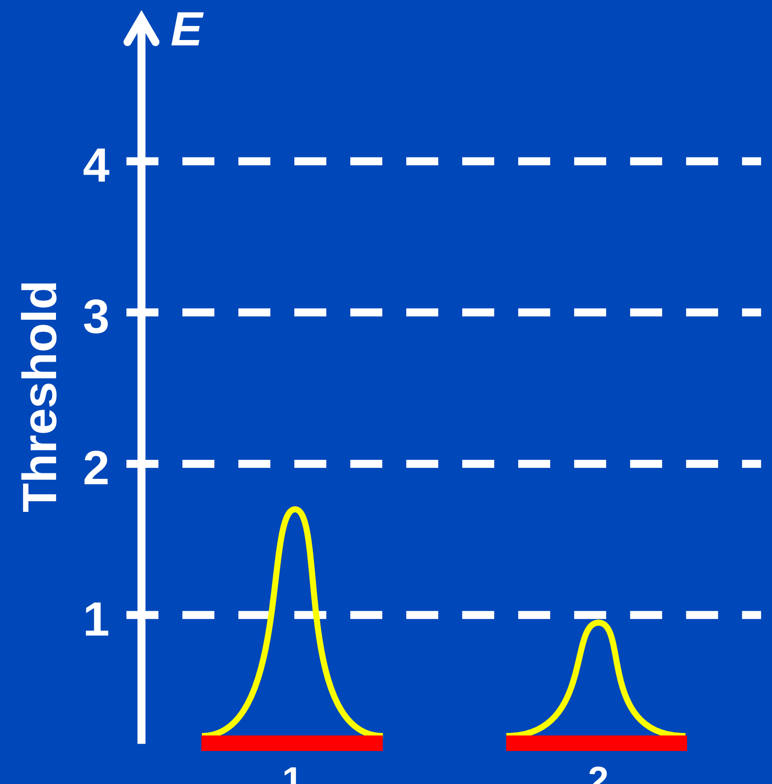


SIEMENS
SOMATOM CounT
@ dkfz.

Siemens CounT CT System

Gantry from a clinical dual source scanner

A: conventional CT detector (50.0 cm FOV)

B: Photon counting detector (27.5 cm FOV)

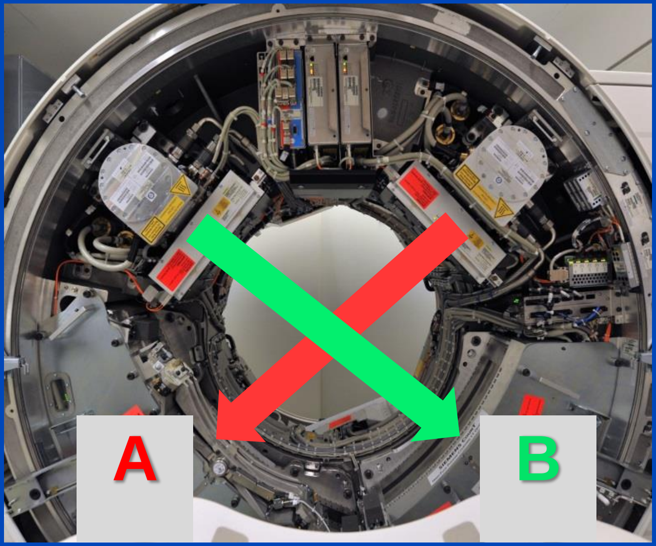

Readout Modes of the CounT

PC-UHR Mode
0.25 mm pixel size

PC-Macro Mode
0.50 mm pixel size

EI detector
0.60 mm pixel size

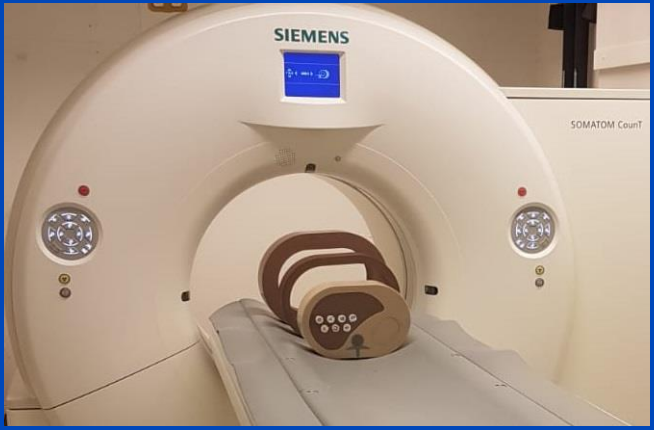

Readout Modes of the Siemens CounT

Macro Mode
0.9 × 1.1 mm focus
2 readouts
16 mm z-coverage

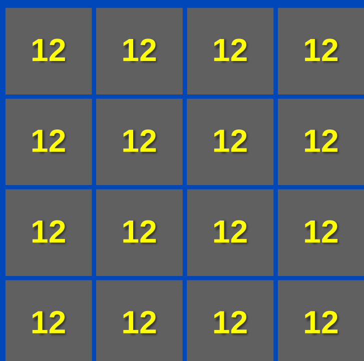

Chess Mode
0.9 × 1.1 mm focus
4 readouts
16 mm z-coverage

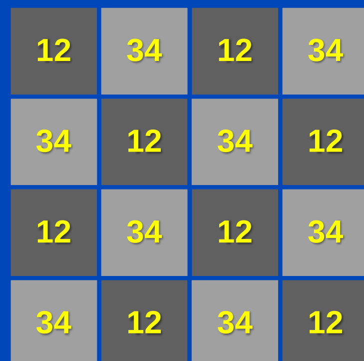

Sharp Mode
0.9 × 1.1 mm focus
5 readouts
12 mm z-coverage

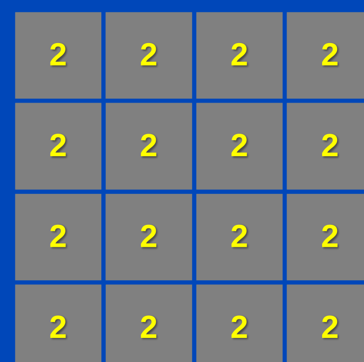

UHR Mode
0.7 × 0.7 mm focus
8 readouts
8 mm z-coverage

1.6 mm CdTe sensor. No FFS on detector B (photon counting detector). 4×4 subpixels of 225 µm size = 0.9 mm pixels (0.5 mm at isocenter). An additional 225 µm gap (e.g. for anti scatter grid) yields a pixel pitch of 1.125 mm.The whole detector consists of 128×1920 subpixels = 32×480 macro pixels.

This photon-counting whole-body CT prototype, installed at the Mayo Clinic, at the NIH and at the DKFZ is a DSCT system. However, it is restricted to run in single source mode. The second source is used for data completion and for comparisons with EI detectors.

Siemens Naeotom Alpha
The World‘s First Photon-Counting CT

Detector Pixel Force vs. Alpha

Force
920 × 96 detector pixels
pixel size 0.52 × 0.56 mm at iso
avg. sampling 0.56 × 0.6 mm at iso
57.6 mm z-coverage

Alpha (Quantum Plus)
1376 × 144 macro pixels
pixel size 0.3 × 0.352 mm at iso
avg. sampling 0.344 × 0.4 mm at iso
57.6 mm z-coverage

Alpha (UHR)
2752 × 120 pixels
pixel size 0.15 × 0.176 mm at iso
avg. sampling 0.172 × 0.2 mm at iso
24 mm z-coverage

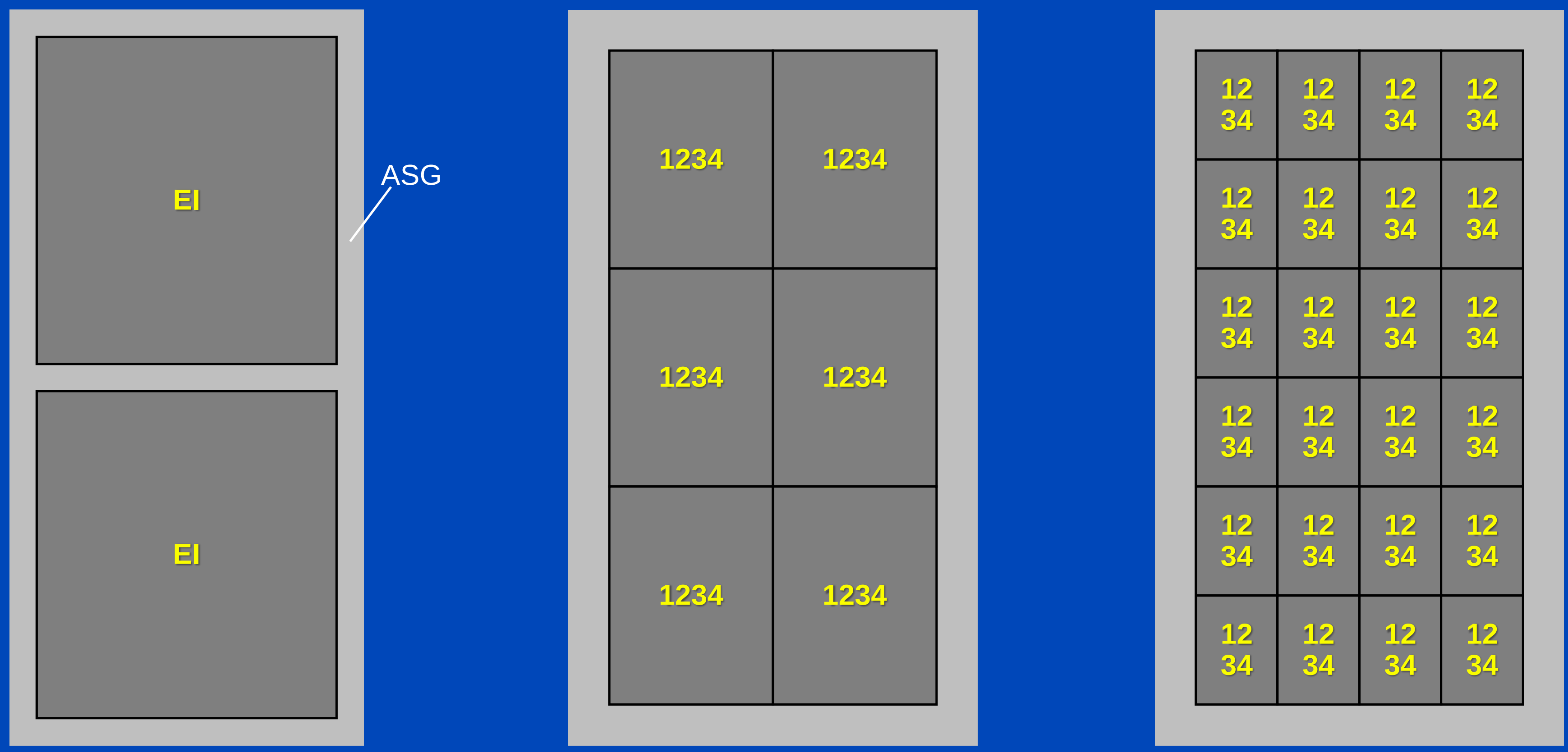

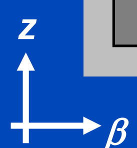

Focus sizes (Vectron): 0.181×0.226 mm, 0.271×0.7316 mm, 0.362×0.497 mm at iso
which are 0.4×0.5 mm, 0.6×0.7 mm, 0.8×1.1 mm at focal spot

ASG information taken from [J. Ferda et al. Computed tomography with a full FOV photon-counting detector in a clinical setting, the first experience. European Journal of Radiology 137:109614, 2021]

Evolution of Spatial Resolution

similar to
2005: Somatom Flash (B70)

Pixel size 0.181 mm
Slice thickness 0.60 mm
Slice increment 0.30 mm
$MTF_{50\%}$ = 8.0 lp/cm
$MTF_{10\%}$ = 9.2 lp/cm

similar to
2014: Somatom CounT (U70)

Pixel size 0.181 mm
Slice thickness 0.20 mm
Slice increment 0.10 mm
$MTF_{50\%}$ = 12.1 lp/cm
$MTF_{10\%}$ = 16.0 lp/cm

scanned at
2021: Naeotom Alpha (Br98u)

Pixel size 0.181 mm
Slice thickness 0.20 mm
Slice increment 0.10 mm
$MTF_{50\%}$ = 39.0 lp/cm
$MTF_{10\%}$ = 42.9 lp/cm

All measurements at Naeotom Alpha, Siemens Healthineers. QIR Reconstructions such that the maximum spatial resolution of Flash, CounT and Alpha is demonstrated on the same sample. *C* = 1200 HU, *W* = 4000 HU

dkfz.

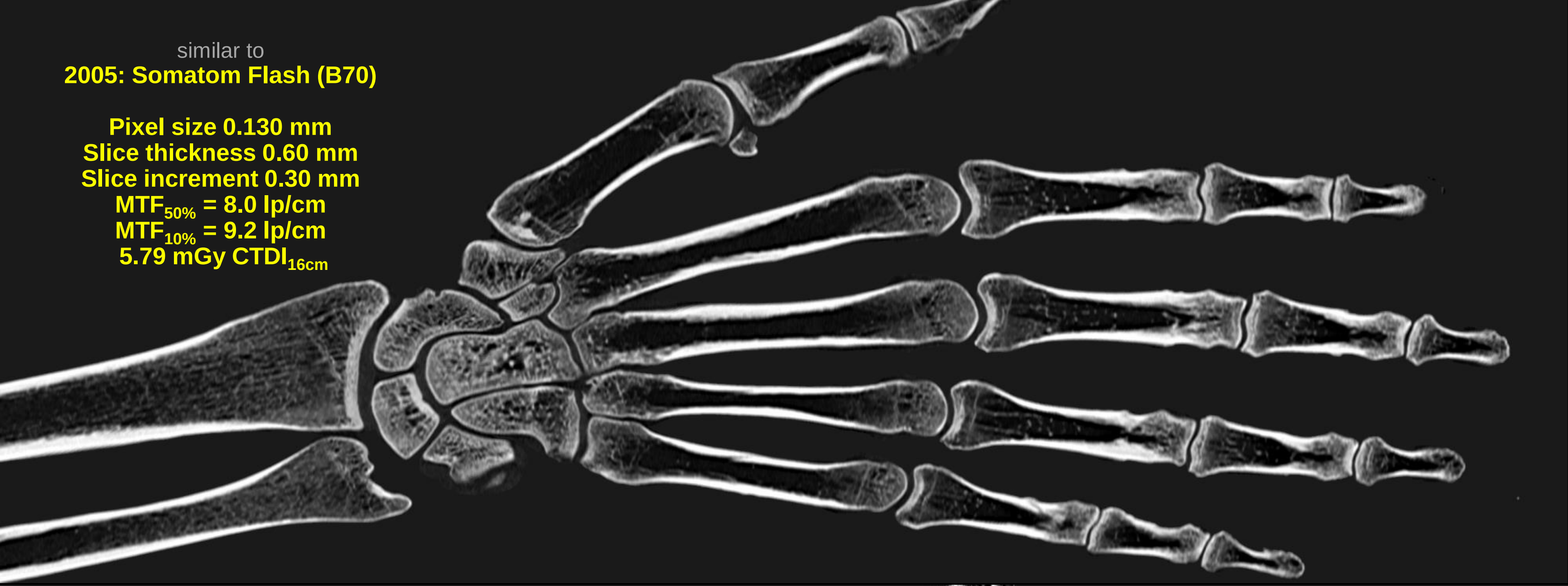
similar to
2005: Somatom Flash (B70)
Pixel size 0.130 mm
Slice thickness 0.60 mm
Slice increment 0.30 mm
$MTF_{50\%}$ = 8.0 lp/cm
$MTF_{10\%}$ = 9.2 lp/cm
5.79 mGy $CTDI_{16cm}$

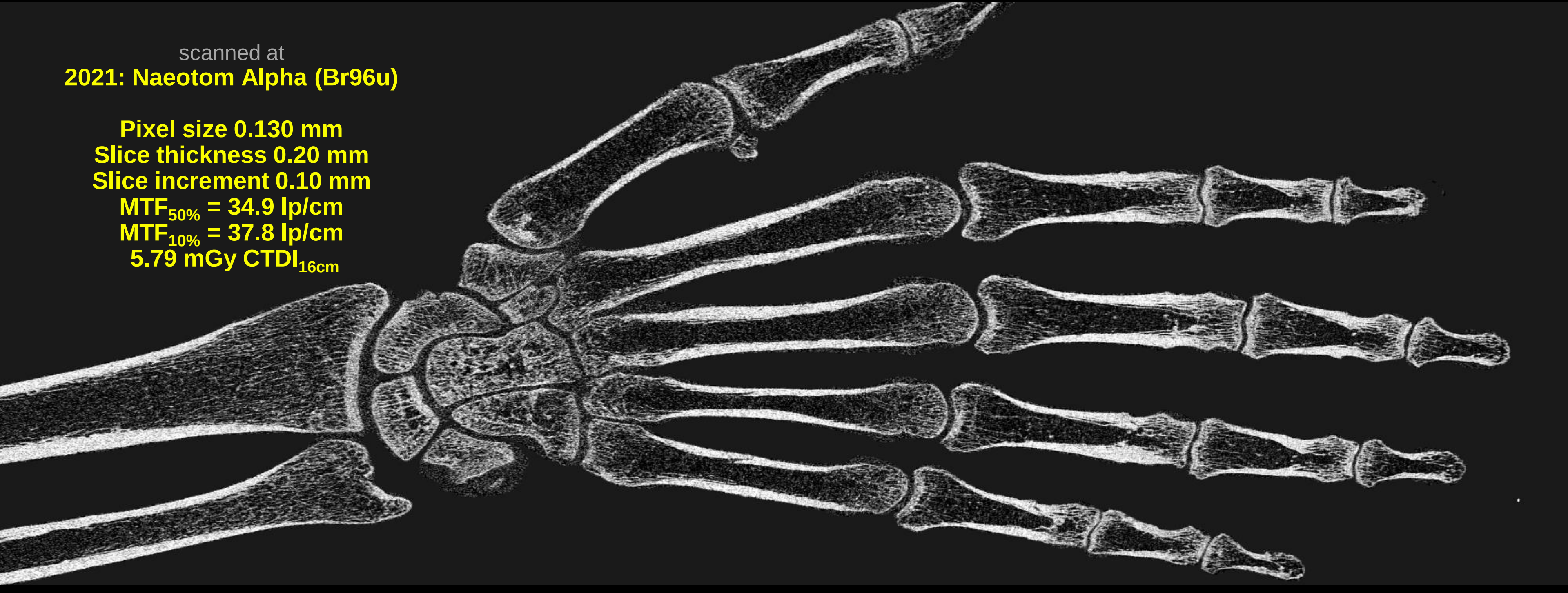
scanned at
2021: Naeotom Alpha (Br96u)
Pixel size 0.130 mm
Slice thickness 0.20 mm
Slice increment 0.10 mm
$MTF_{50\%}$ = 34.9 lp/cm
$MTF_{10\%}$ = 37.8 lp/cm
5.79 mGy $CTDI_{16cm}$

Advantages of Photon Counting CT

- No reflective gaps between detector pixels
  - Higher geometrical efficiency
  - Less dose
- No electronic noise
  - Less dose for infants
  - Less noise for obese patients
- Counting
  - Swank factor = 1 = maximal
  - “Iodine effect“ due to higher weights on low energies
- Energy bin weighting
  - Lower dose/noise
  - Improved iodine CNR
- Smaller pixels (to avoid pileup)
  - Higher spatial resolution
  - “Small pixel effect” i.e. lower dose/noise at conventional resolution
- Spectral information on demand
  - Dual Energy CT (DECT)
  - Multi Energy CT (MECT)

No Electronic Noise!

- **Photon counting detectors have no electronic noise.**
- **Extreme low dose situations will benefit**
  - **Pediadric scans at even lower dose**
  - **Obese patients with less noise**
  - **…**

EI (Dexela)

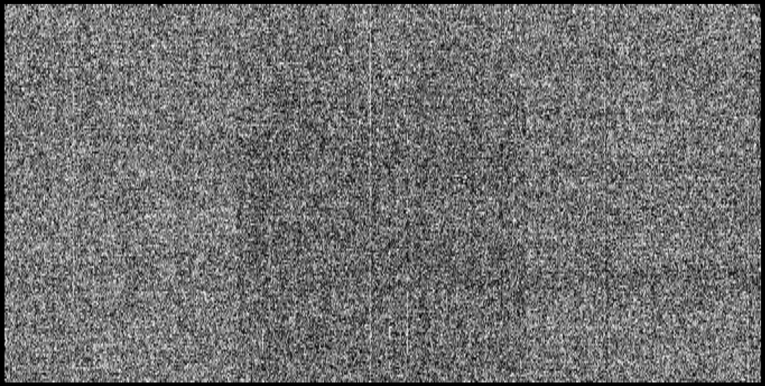

Readout noise only. Single events hidden!

PC (Dectris)

No readout noise. Single events visible!

18 frames, 5 min integration time per frame, x-ray off

Energy Integrating
(Detected Spectra at 100 kV and 140 kV)

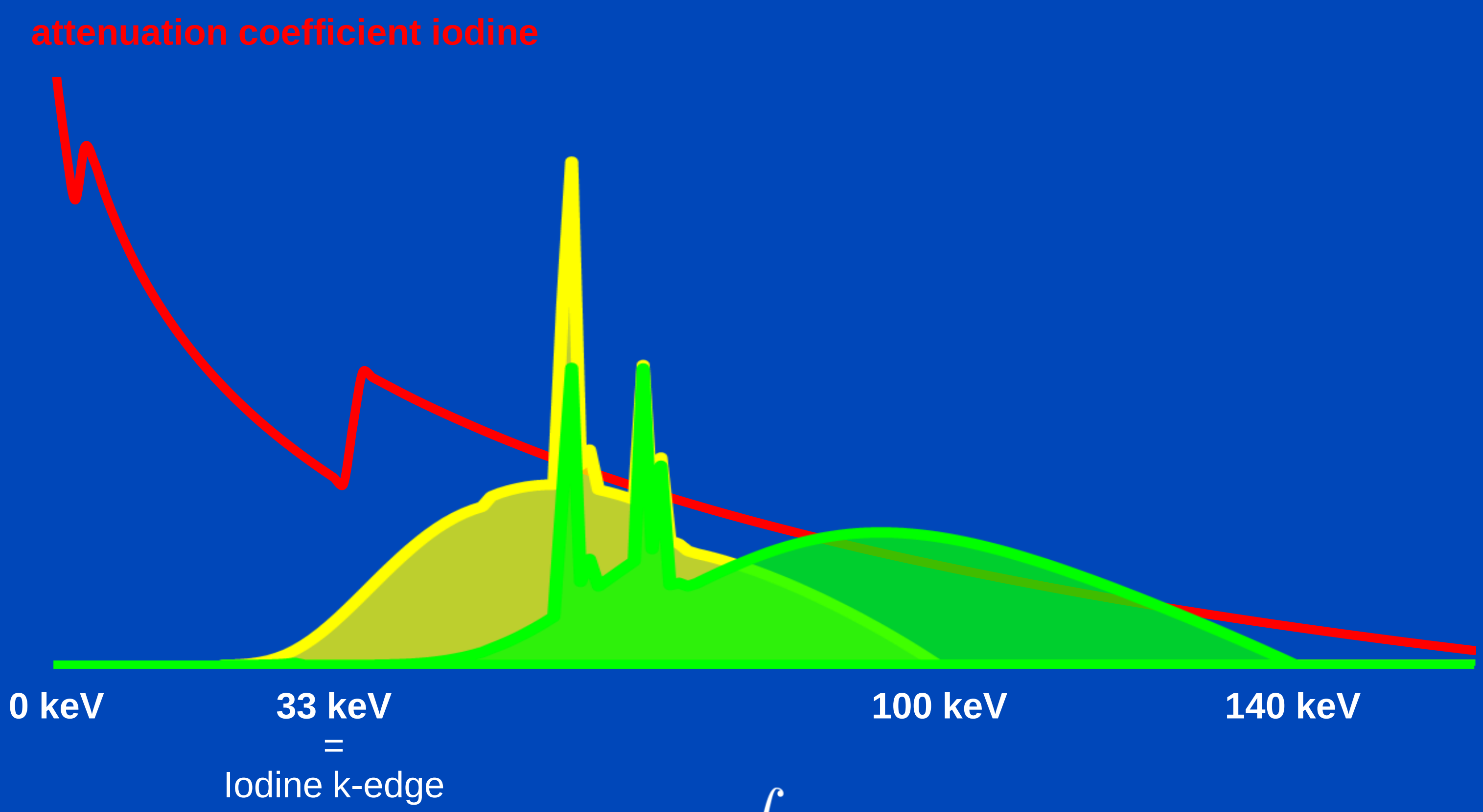

$$\mathrm{Signal}_{\mathrm{EI}} = \int dE \, E \; N(E)$$

Spectra as seen after having passed a 32 cm water layer.

Photon Counting
(Detected Spectra at 100 kV and 140 kV)

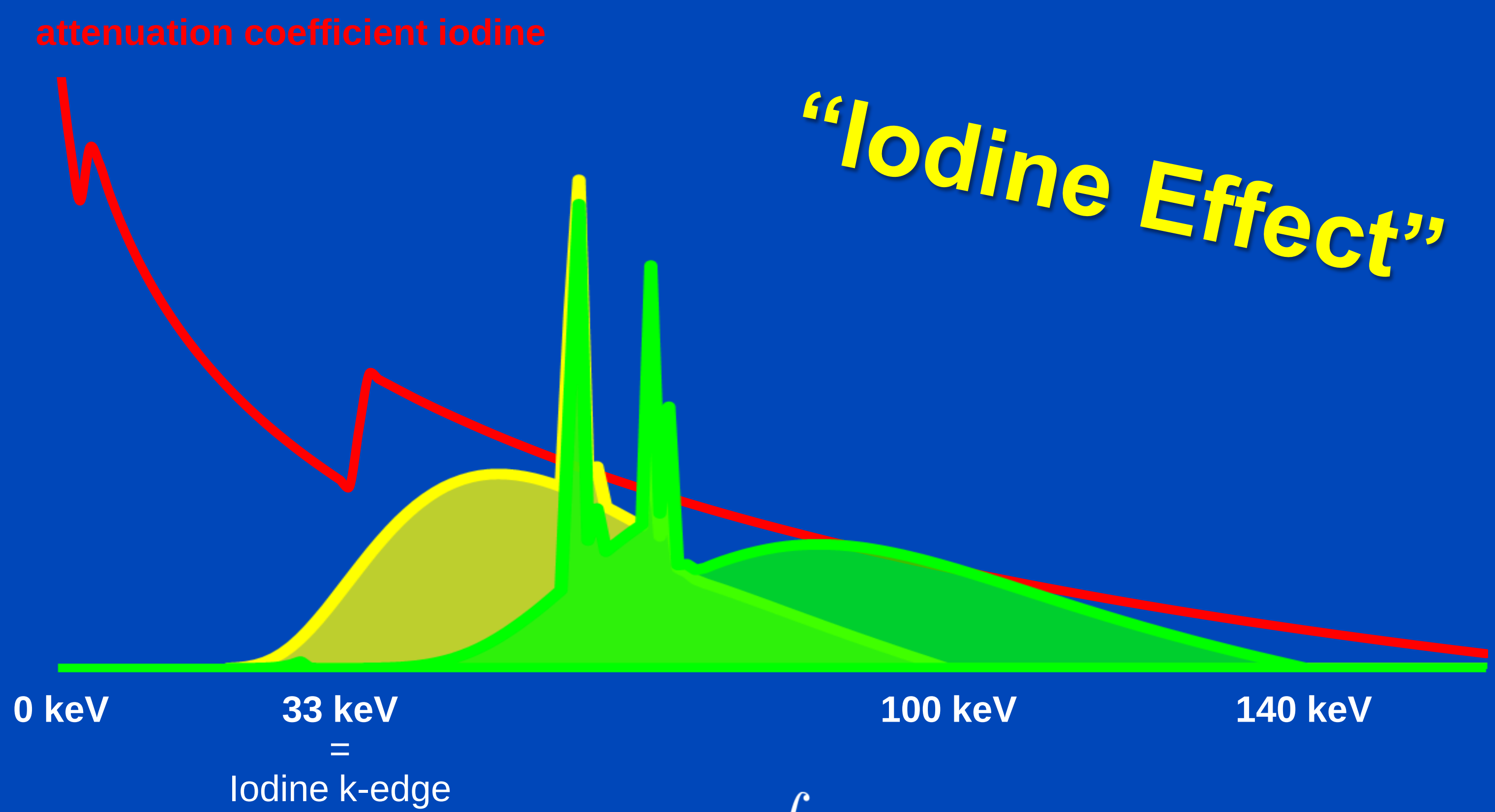

$$\mathrm{Signal}_{\mathrm{PC}} = \int dE\, 1\;\; N(E)$$

Spectra as seen after having passed a 32 cm water layer.

Swank Factor

- The Swank factor measures the relative SNR^2, and thus the relative dose efficiency between photon counting (PC) and energy integrating (EI).
- PC always has the highest SNR.

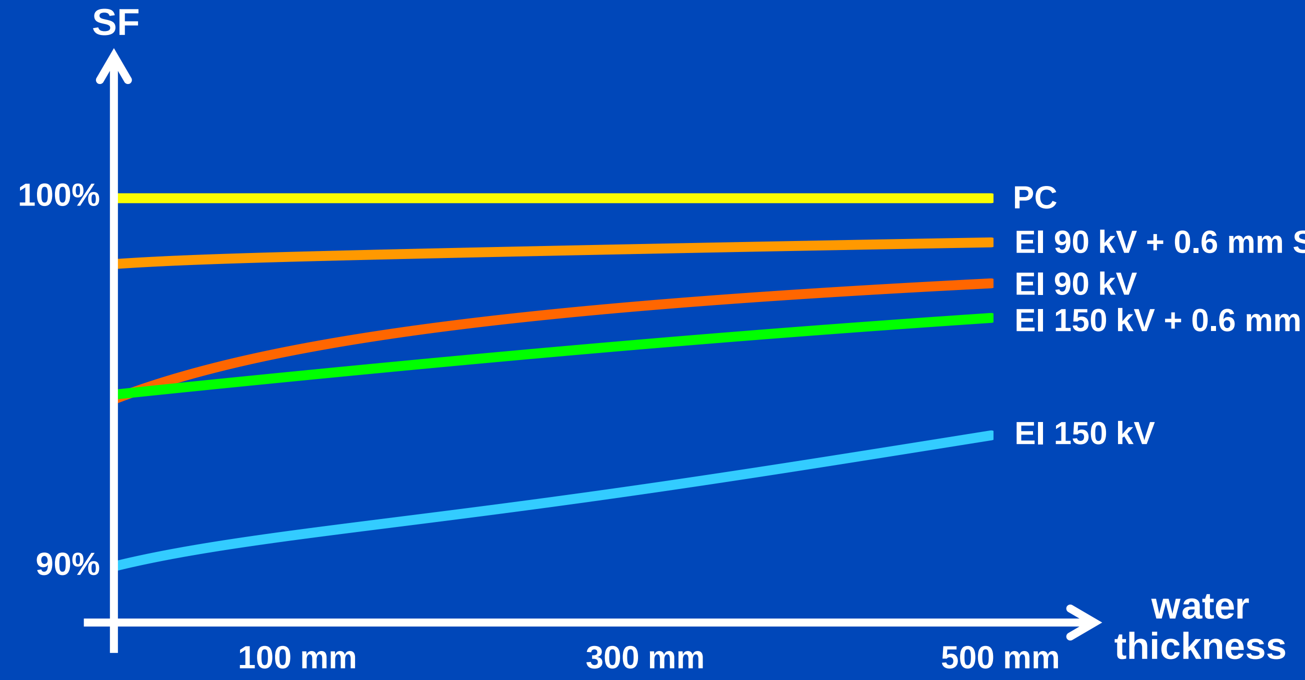

$$\mathrm{SF} = \frac{\mathrm{SNR}^2_{\mathrm{EI}}}{\mathrm{SNR}^2_{\mathrm{PC}}} = \frac{\left(\int dE\, E N(E)\right)^2}{\left(\int dE\, N(E)\right)\left(\int dE\, E^2 N(E)\right)} \leq 1$$

due to Schwarz' inequality

Photon Counting used to Maximize CNR

- With PC, energy bin sinograms can be weighted individually, i.e. by a weighted summation
- To optimize the CNR the optimal bin weighting factor w_b is given by (weighting after log):

$$w_b \propto \frac{C_b}{V_b}$$

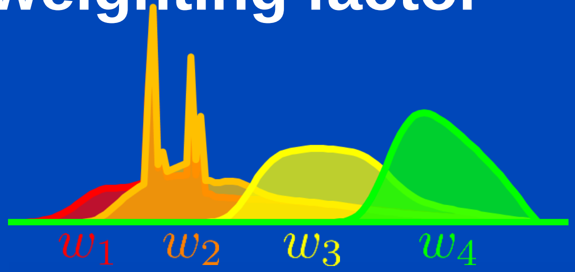

- The resulting CNR is

$$\mathrm{CNR}^2 = \frac{\left(\sum_b w_b C_b\right)^2}{\sum_b w_b^2 V_b}$$

- At the optimum this evaluates to

$$\mathrm{CNR}^2 = \sum_{b=1}^{B} \mathrm{CNR}_b^2$$

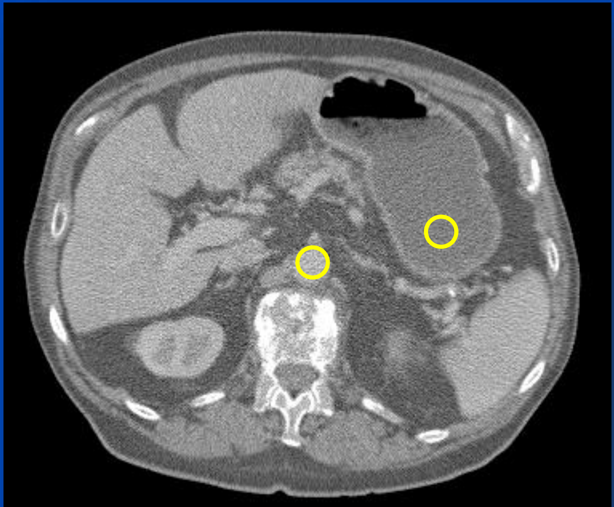

The two ROIs are used to measure the CNR.

Energy Integrating vs. Photon Counting
with 1 bin from 20 to 140 keV

Energy Integrating

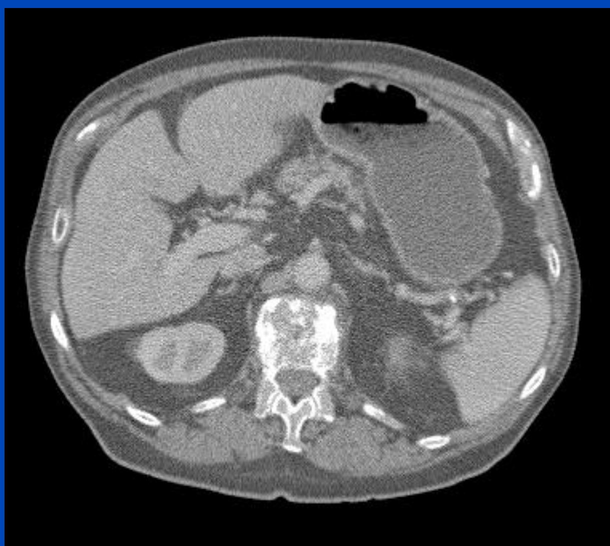

CNR = 2.11

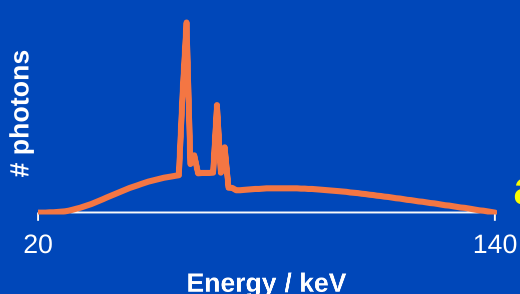

PC minus EI

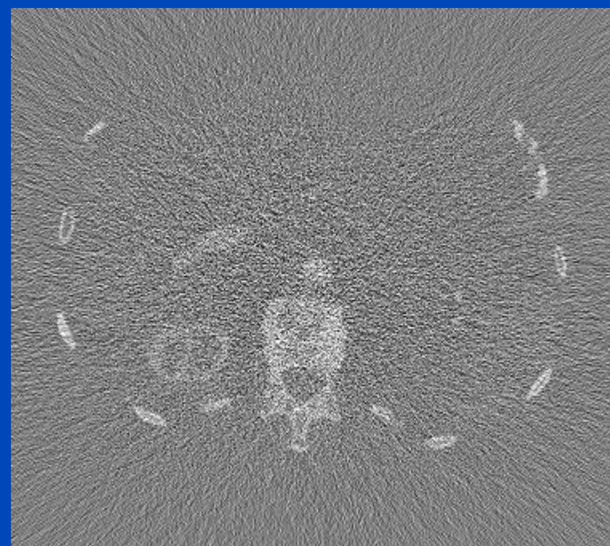

Photon Counting

CNR = 2.95

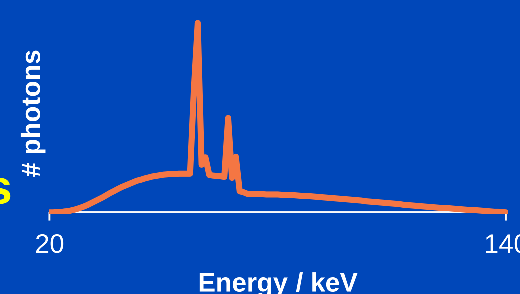

40% CNR improvement or 49% dose reduction achievable due to improved Swank factor and more weight on low energies (iodine contrast benefits).

Images: *C* = 0 HU, *W* = 700 HU, difference image: *C* = 0 HU, *W* = 350 HU, bins start at 20 keV

Energy Integrating vs. Photon Counting
with 4 bins from 20 to 140 keV

Energy Integrating

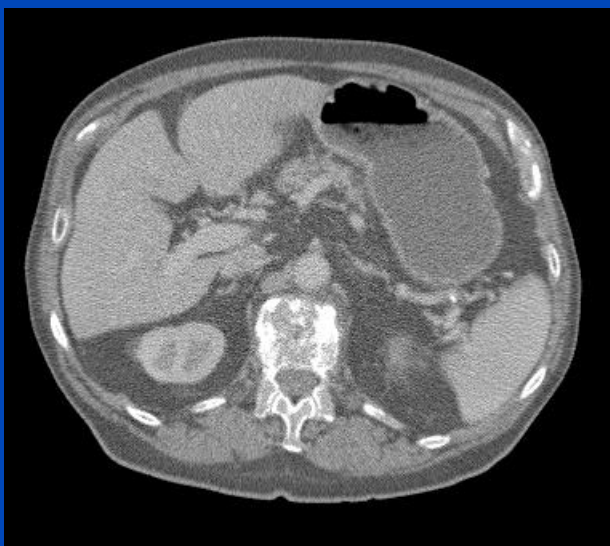

PC minus EI

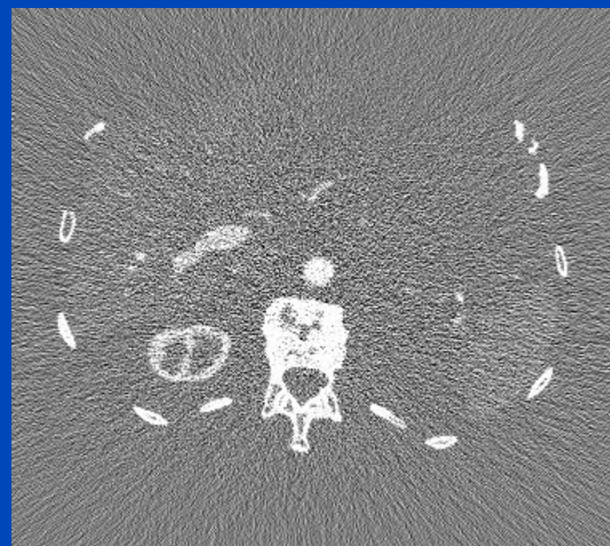

Photon Counting

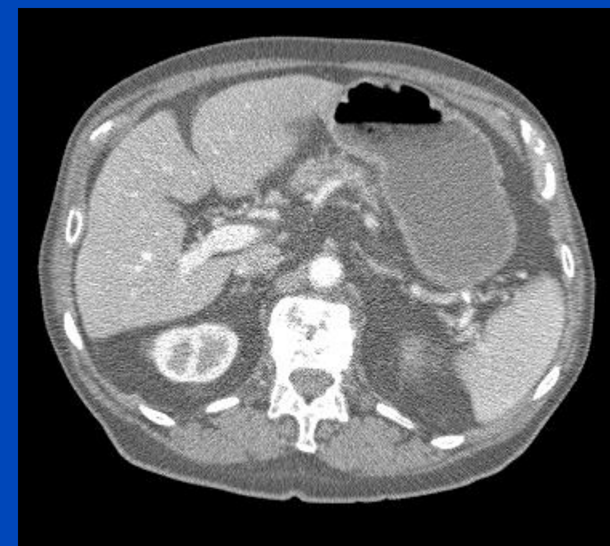

CNR = 2.11

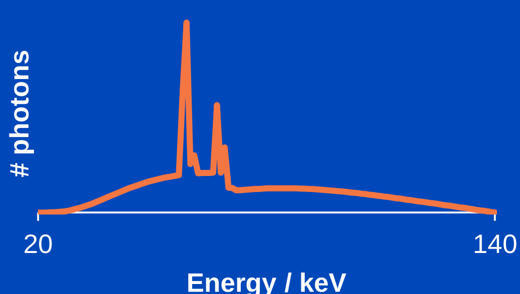

**99% CNR improvement or
75% dose reduction achievable
due to improved Swank factor
and optimized energy weighting.**

CNR = 4.19

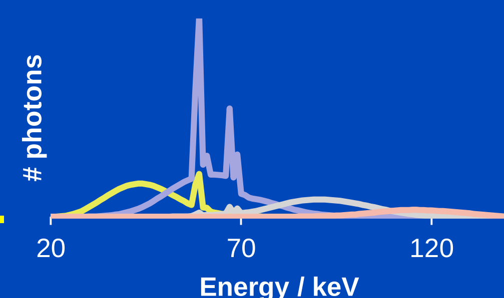

Images: *C* = 0 HU, *W* = 700 HU, difference image: *C* = 0 HU, *W* = 350 HU, bins start at 20 keV

Iodine CNRD Assessment

Reconstruction Examples @ 80 kV

Small (200 × 300 mm)

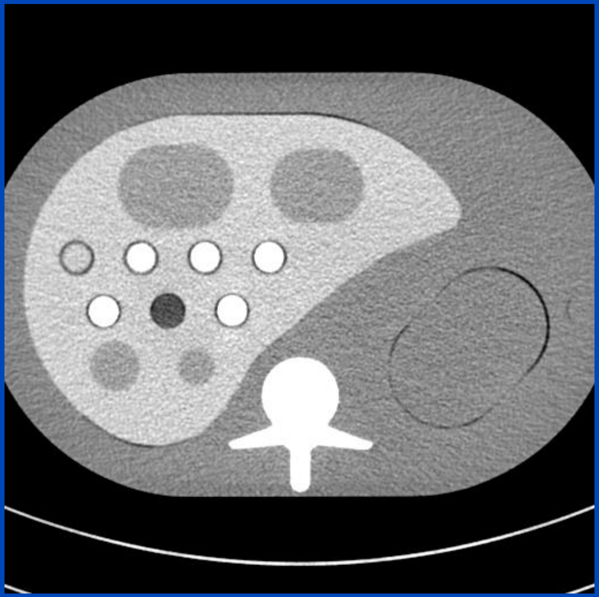

Medium (250 × 350 mm)

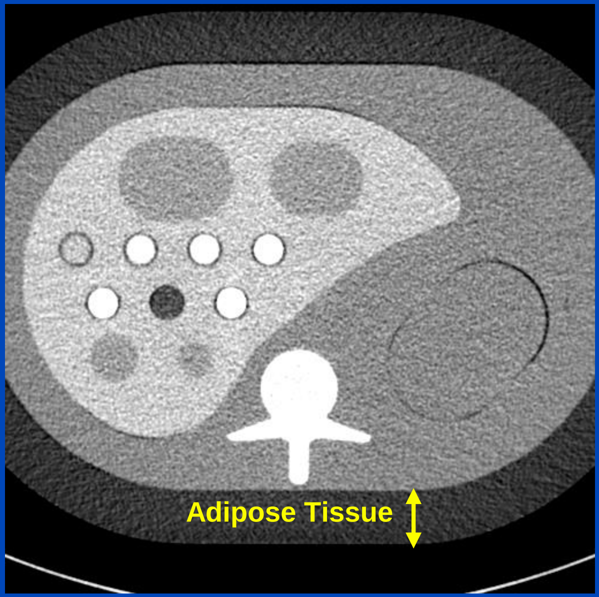

Large (300 × 400 mm)

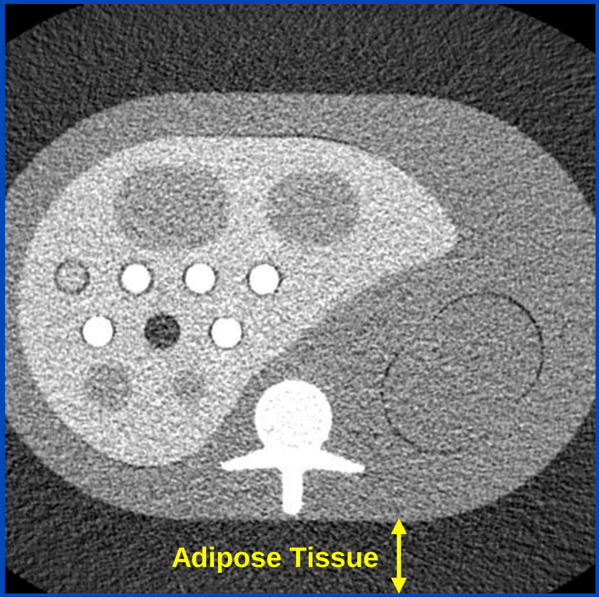

C/W=0 HU/400HU

Iodine CNRD Assessment

Regions of Interest

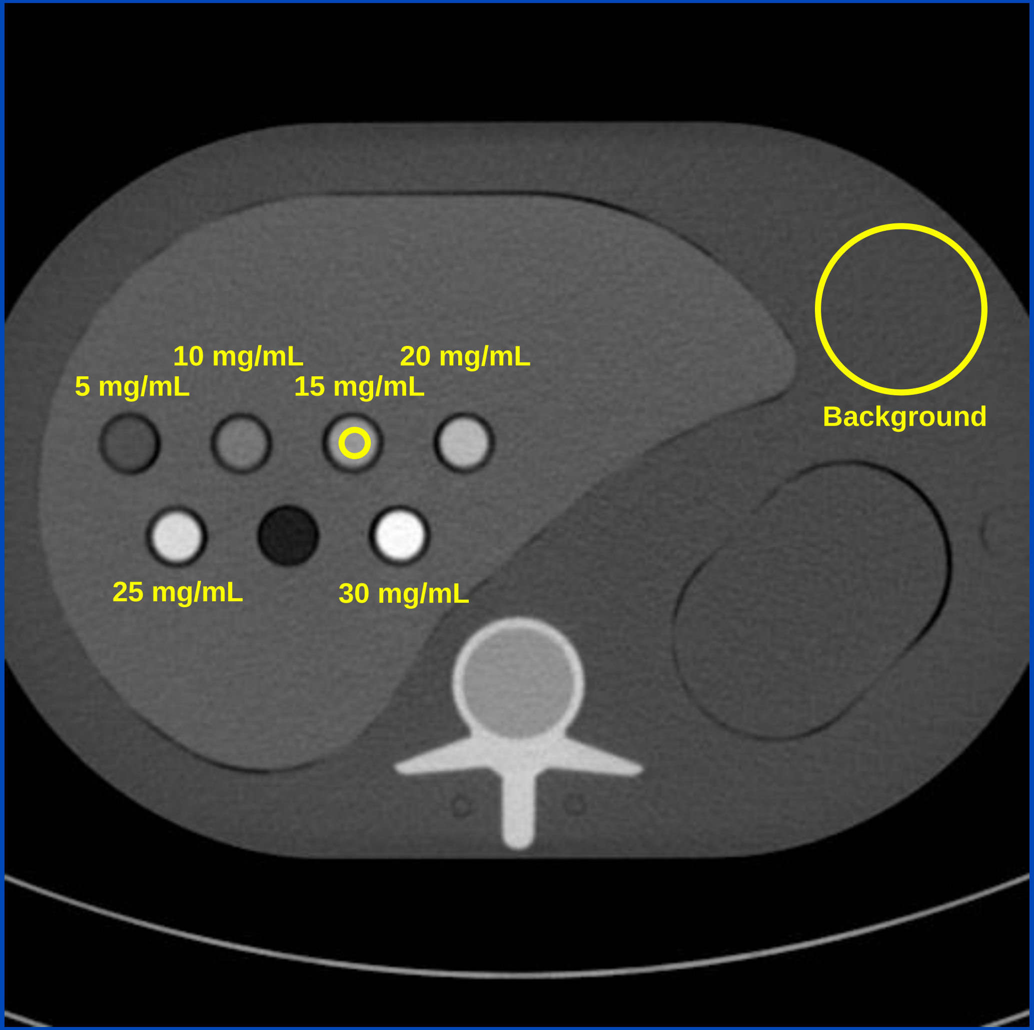

C/W=180 HU/600HU

PC with 1 Bin vs. EI

Potential Dose Reduction

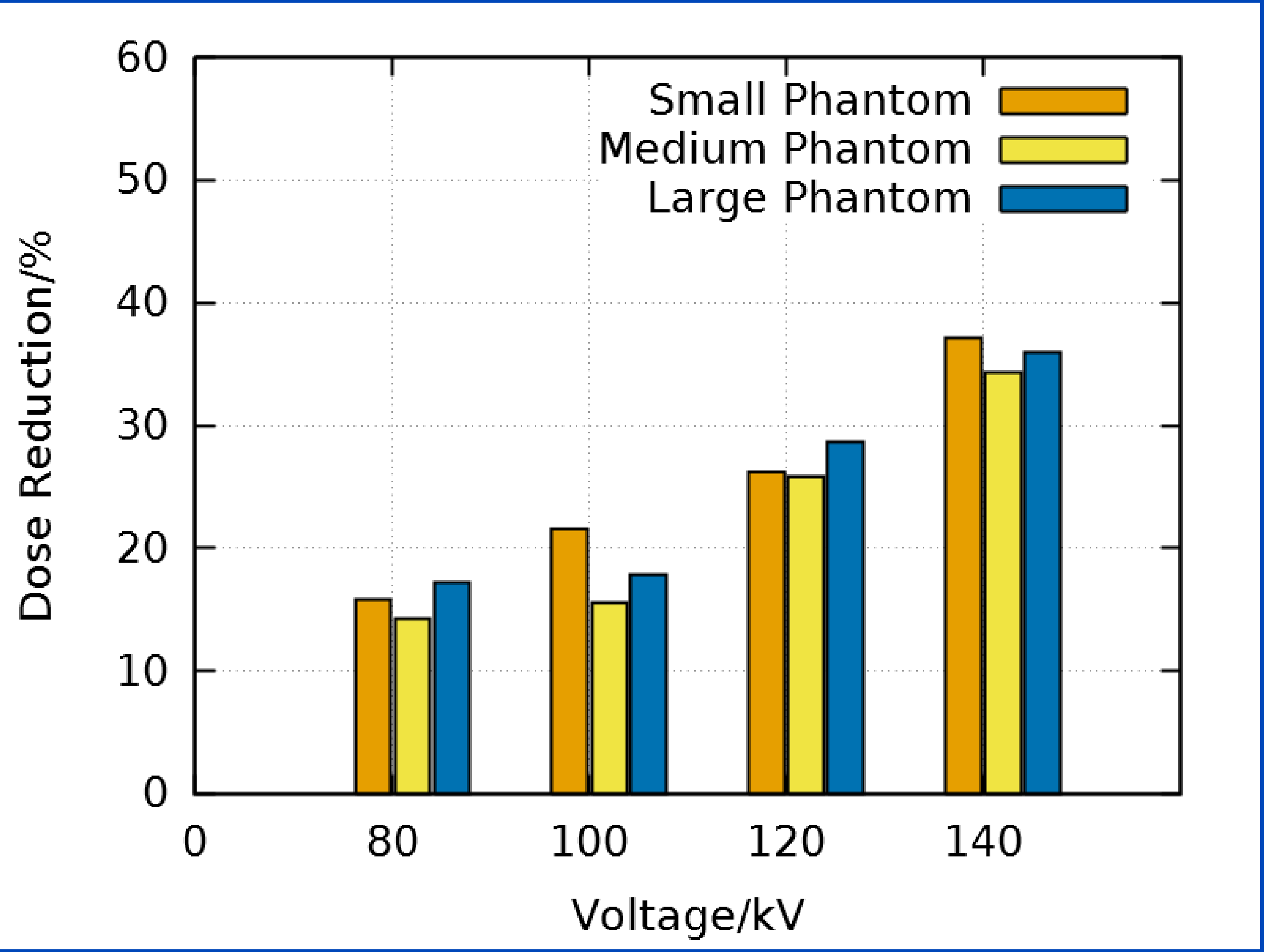

PC with 2 Bins vs. EI

Potential Dose Reduction

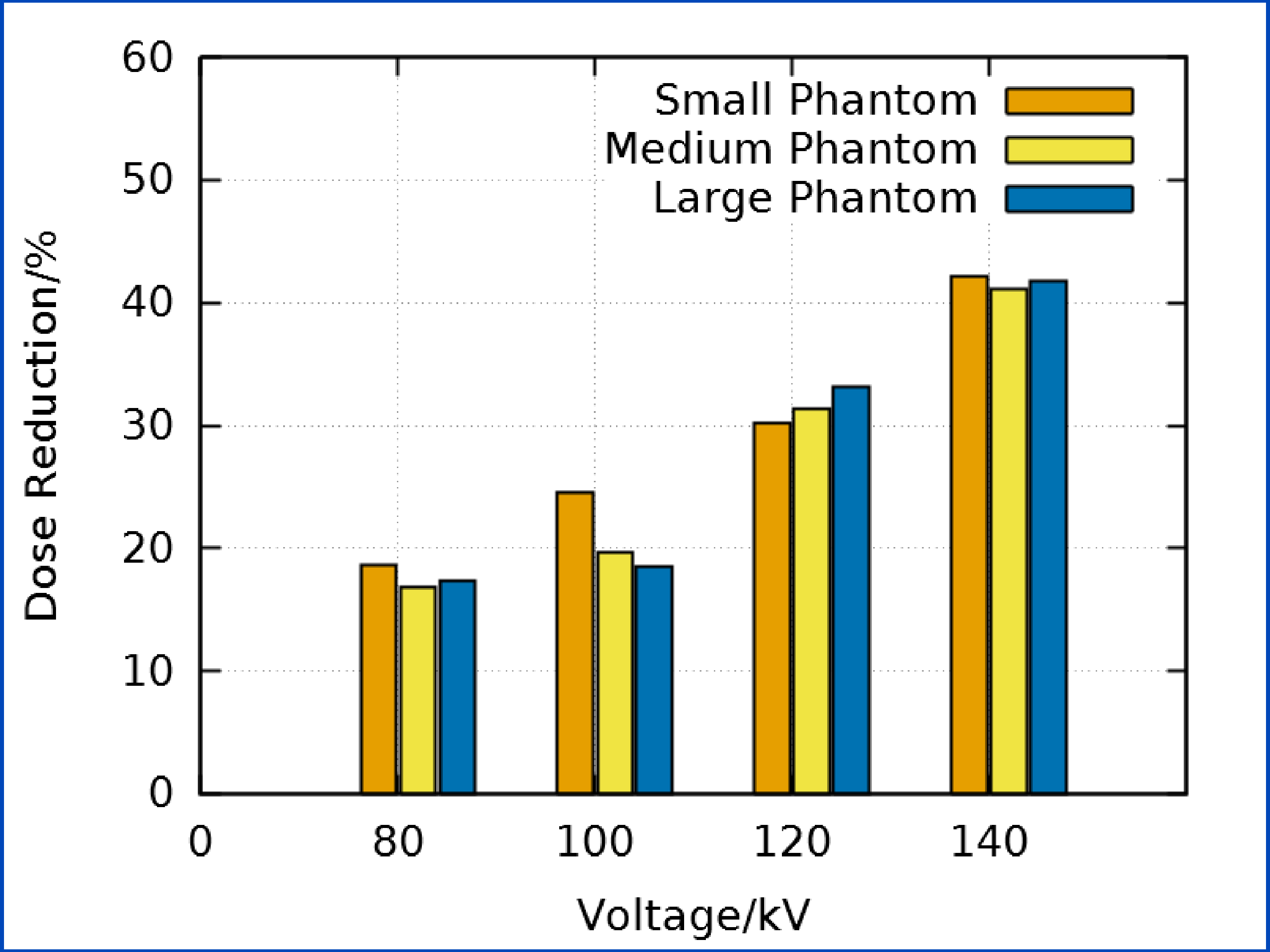

Ultra-High Spatial Resolution on Demand!

- Small electrodes are necessary to avoid pile-up.
- High bias voltages (around 300 V) limit charge diffusion and thus blurring in the non-structured semiconductor layer.
- Thus, higher spatial resolution is achievable.

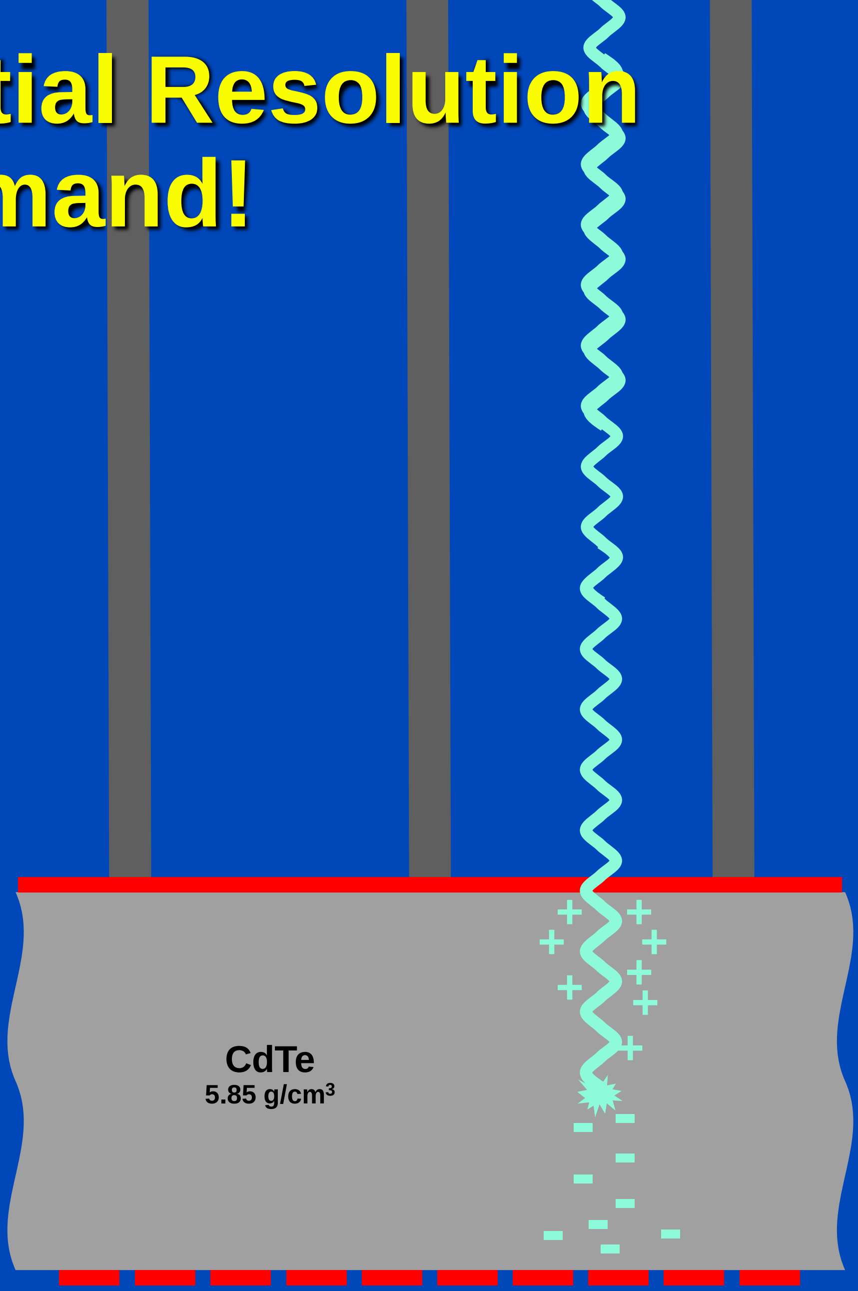

The “Small Pixel Effect”

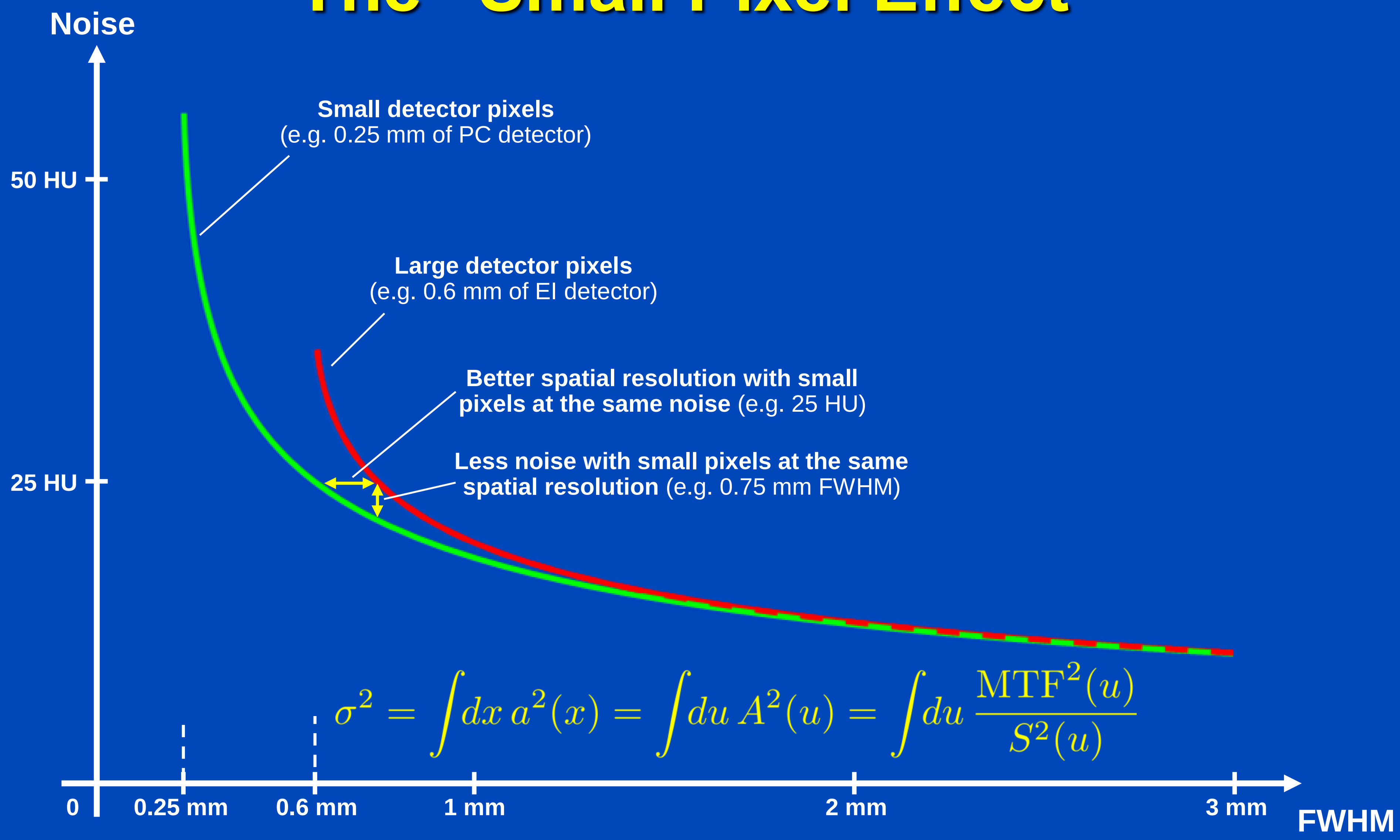

$$\sigma^2 = \int dx\, a^2(x) = \int du\, A^2(u) = \int du\, \frac{\mathrm{MTF}^2(u)}{S^2(u)}$$

Kachelrieß, Kalender. Med. Phys. 32(5):1321-1334, May 2005

All images reconstructed with 1024² matrix and 0.15 mm slice increment.
C = 1000 HU
W = 3500 HU

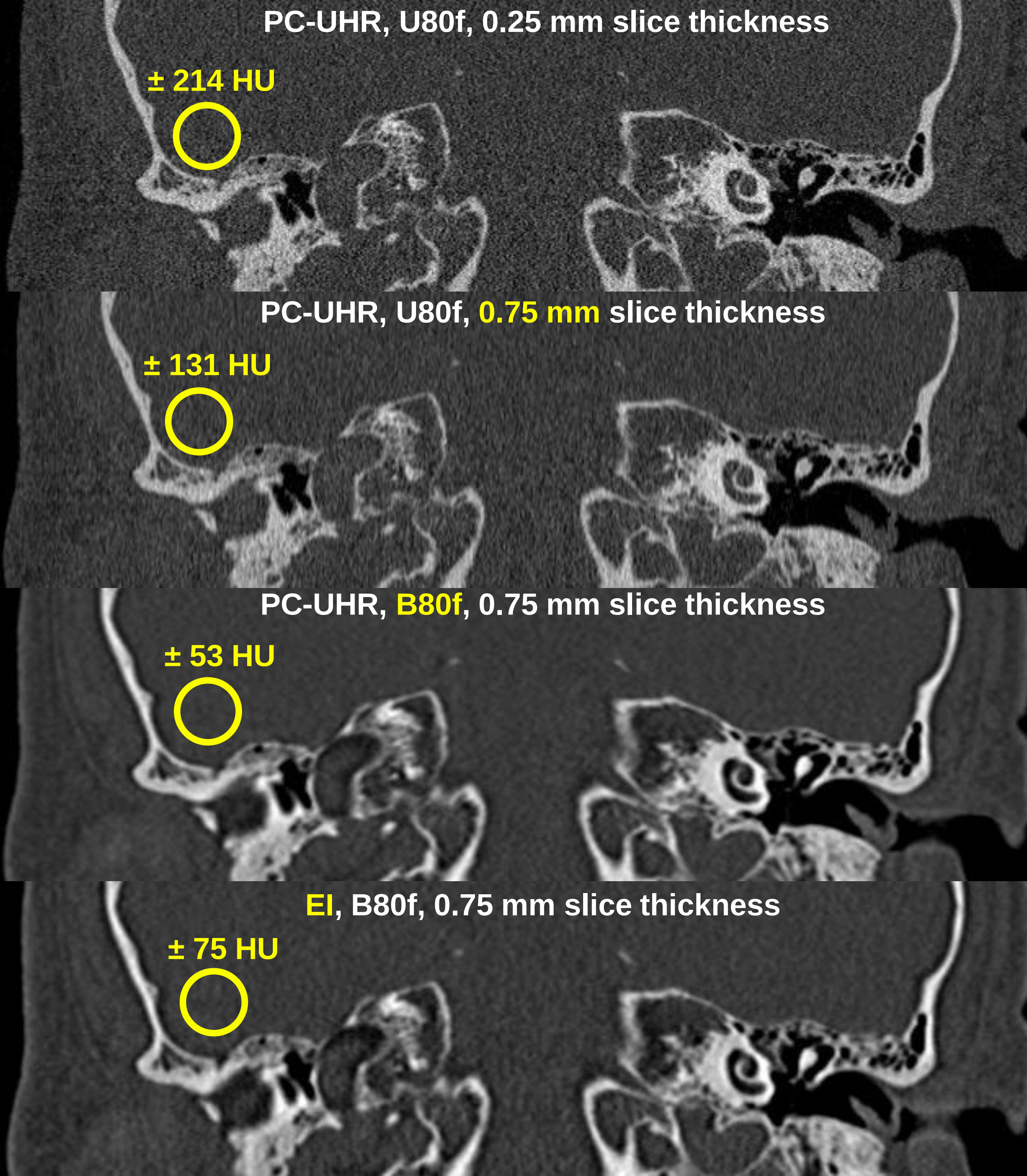

z
x

10% MTF: 19.1 lp/cm
10% MTF:17.2 lp/cm
xy FWHM: 0.48 mm
z FWHM: 0.40 mm
$CTDI_{vol}$: 16.0 mGy

10% MTF: 19.1 lp/cm
10% MTF:17.2 lp/cm
xy FWHM: 0.48 mm
z FWHM: 0.67 mm
$CTDI_{vol}$: 16.0 mGy

10% MTF: 9.3 lp/cm
10% MTF:10.5 lp/cm
xy FWHM: 0.71 mm
z FWHM: 0.67 mm
$CTDI_{vol}$: 16.0 mGy

10% MTF: 9.3 lp/cm
10% MTF:10.5 lp/cm
xy FWHM: 0.71 mm
z FWHM: 0.67 mm
$CTDI_{vol}$: 16.0 mGy

Data courtesy of the Institute of Forensic Medicine of the University of Heidelberg and of the Division of Radiology of the German Cancer Research Center (DKFZ)

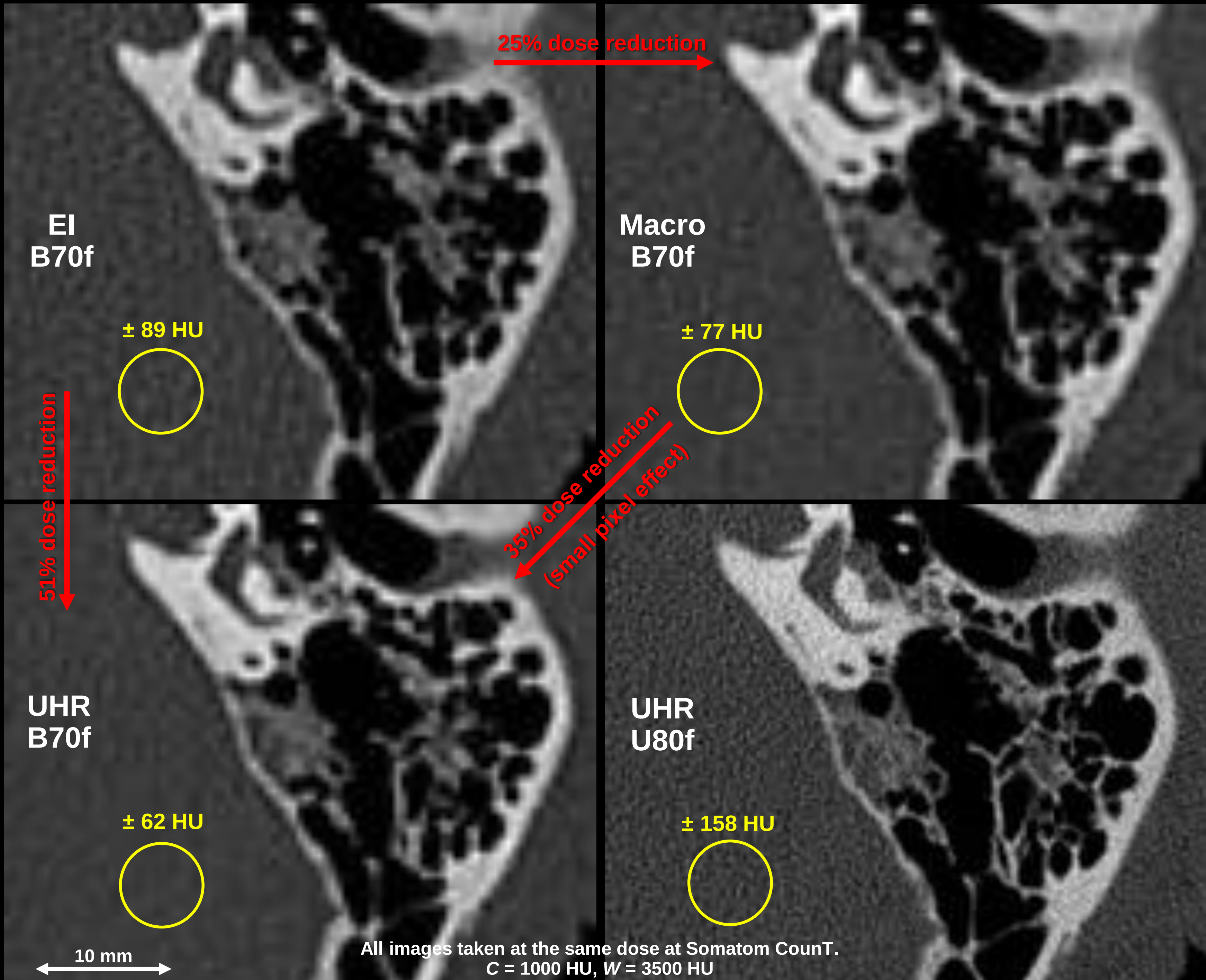

25% dose reduction
EI
B70f
± 89 HU
Macro
B70f
± 77 HU
51% dose reduction
35% dose reduction
(small pixel effect)
UHR
B70f
± 62 HU
UHR
U80f
± 158 HU
10 mm
All images taken at the same dose at Somatom CounT.
C = 1000 HU, W = 3500 HU

L. Klein, C. Amato, S. Heinze, M. Uhrig, H.-P. Schlemmer, M. Kachelrieß, and S. Sawall. **Effects of Detector Sampling on Noise Reduction in a Clinical Photon Counting Whole-Body CT**. Investigative Radiology, vol. 55(2):111-119, February 2020.

Energy Integrating Detector (B70f)

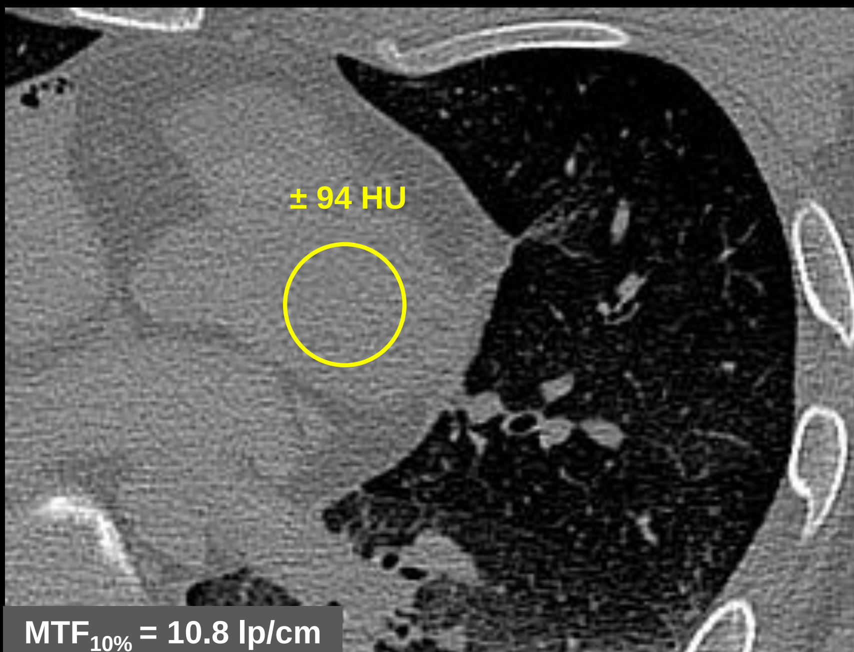

Photon Counting Detector (B70f)

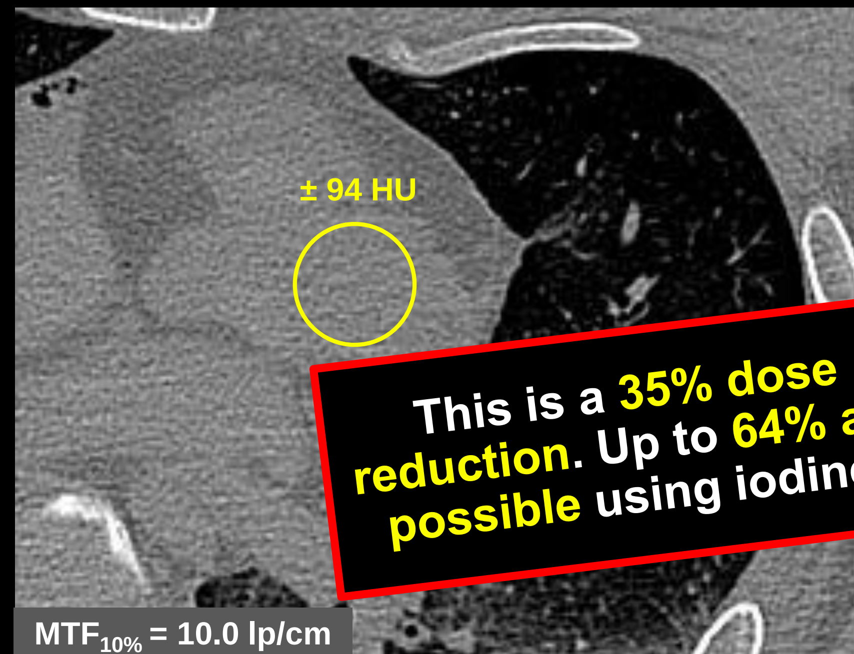

Acquisition with EI:
- **Tube voltage of 120 kV**
- **Tube current of 300 mAs**
- **Resulting dose of $\mathrm{CTDI}_{\mathrm{vol\ 32\ cm}}$ = 22.6 mGy**

Acquisition with UHR:
- **Tube voltage of 120 kV**
- **Tube current of 180 mAs**
- **Resulting dose of $\mathrm{CTDI}_{\mathrm{vol\ 32\ cm}}$ = 14.6 mGy**

C = 50 HU, W = 1500 HU

dkfz.

X-Ray Dose Reduction of B70f

PC vs. PC
("small pixel effect only")

UHR vs. Macro	80 kV	100 kV	120 kV	140 kV
S	**23%** ± 12%	**34%** ± 10%	**35%** ± 11%	**25%** ± 10%
M	**32%** ± 10%	**32%** ± 8%	**35%** ± 8%	**34%** ± 9%
L	**35%** ± 10%	**29%** ± 15%	**27%** ± 9%	**31%** ± 11%

PC vs. EI
("small pixel effect"
and "iodine effect")

UHR vs. EI	80 kV	100 kV	120 kV	140 kV
S	**33%** ± 9%	**52%** ± 5%	**57%** ± 7%	**57%** ± 6%
M	**41%** ± 8%	**47%** ± 7%	**60%** ± 6%	**62%** ± 4%
L	**48%** ± 8%	**43%** ± 10%	**54%** ± 6%	**63%** ± 5%

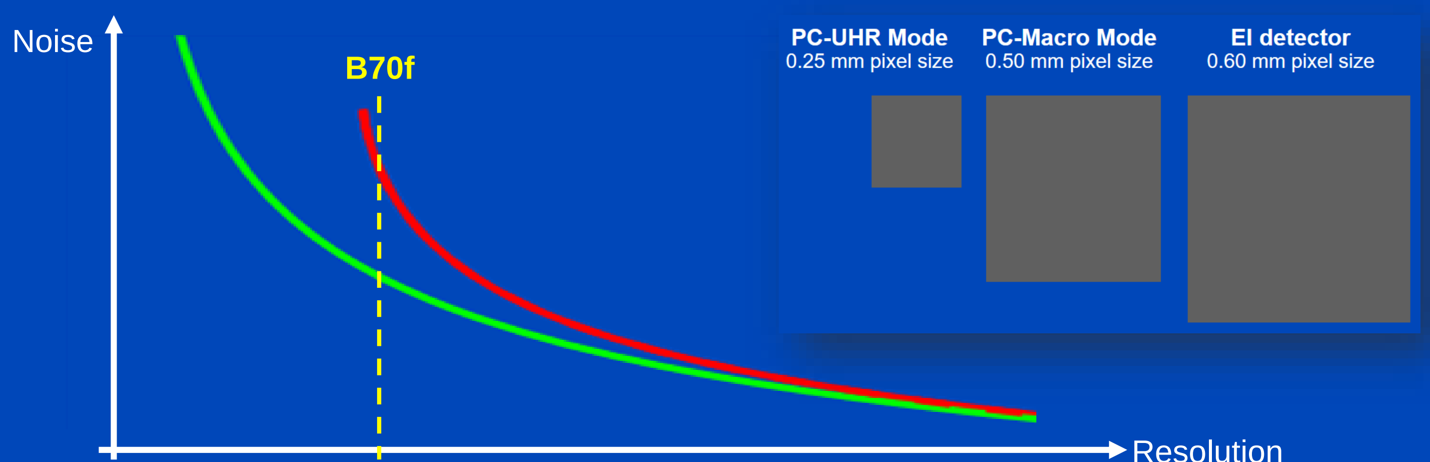

Klein, Kachelrieß, Sawall et al. Invest. Radiol. 55(2), Feb 2020

dkfz.

K-Edges: More than Dual Energy CT?

$$\mu(\boldsymbol{r},E) = f_1(\boldsymbol{r})\psi_1(E) + f_2(\boldsymbol{r})\psi_2(E) + \cancel{f_3(\boldsymbol{r})\psi_3(E)} + \ldots$$

Apart from special applications, e.g.
Iodine k-edge imaging of the breast

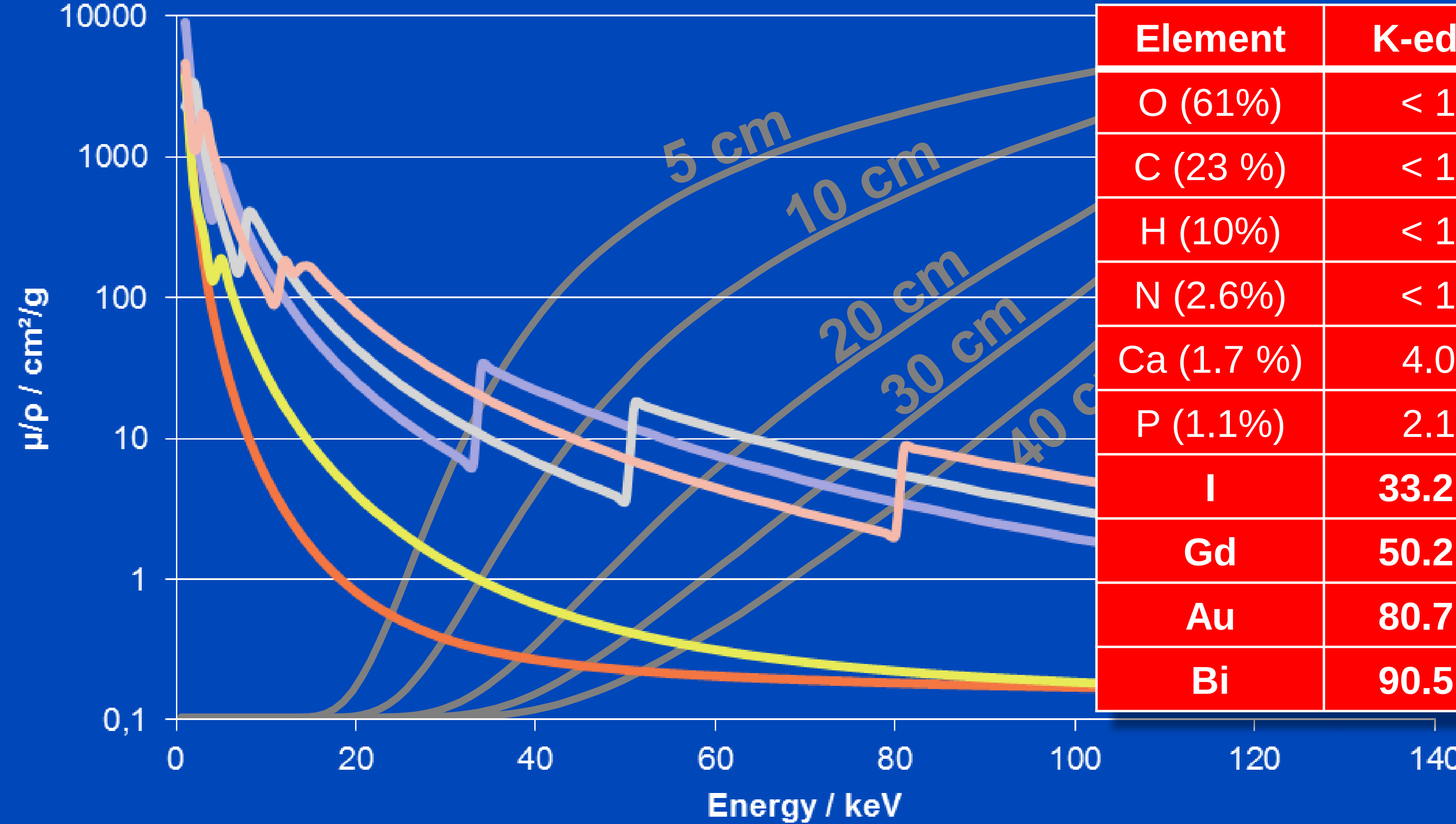

Element	K-edge
O (61%)	< 1 keV
C (23 %)	< 1 keV
H (10%)	< 1 keV
N (2.6%)	< 1 keV
Ca (1.7 %)	4.0 keV
P (1.1%)	2.1 keV
I	**33.2 keV**
Gd	**50.2 keV**
Au	**80.7 keV**
Bi	**90.5 keV**

Gray curves: 120 kV water transmission on a non-logarithmic ordinate individually normalized to 1 at 140 keV.

DECT

Ca-I Decomposition

Macro mode
140 kV, 25/65 keV
C = 0 HU, W = 1200 HU

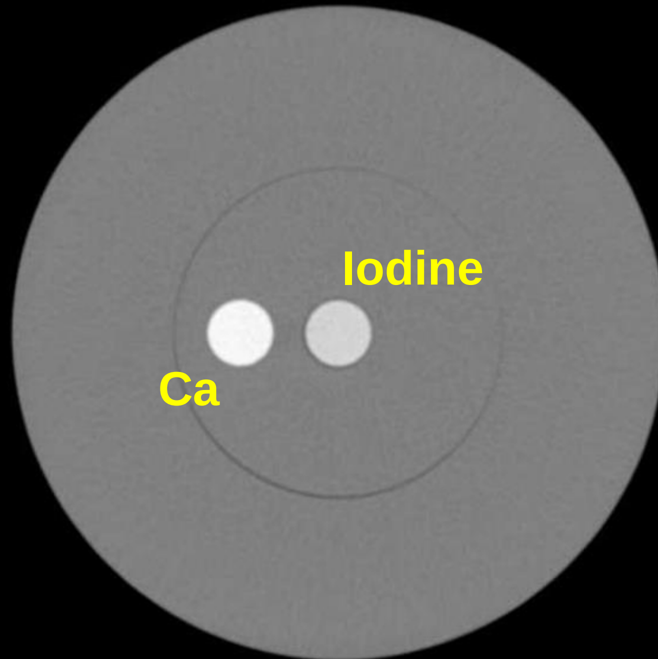

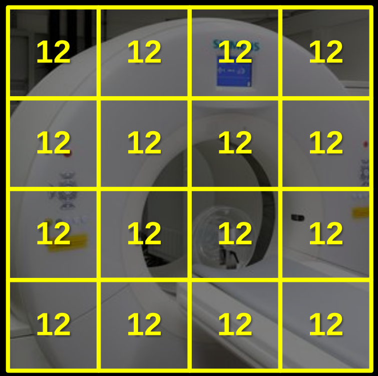

Calcium image

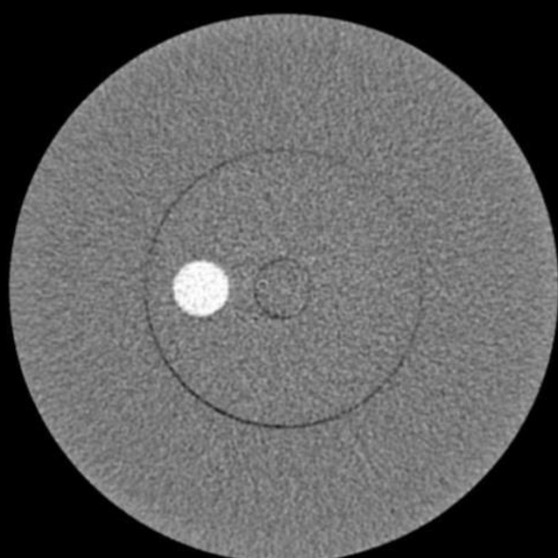

Iodine image

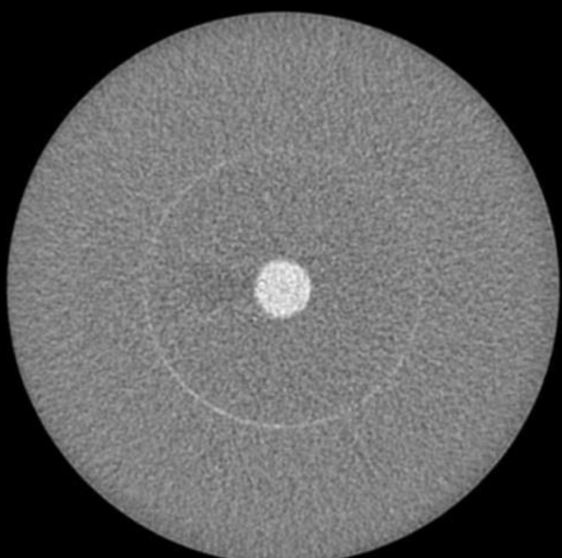

Courtesy of Siemens Healthcare

MECT

Ca-Gd-I Decomposition

Chess pattern mode
140 kV, 20/35/50/65 keV
***C* = 0 HU, *W* = 1200 HU**

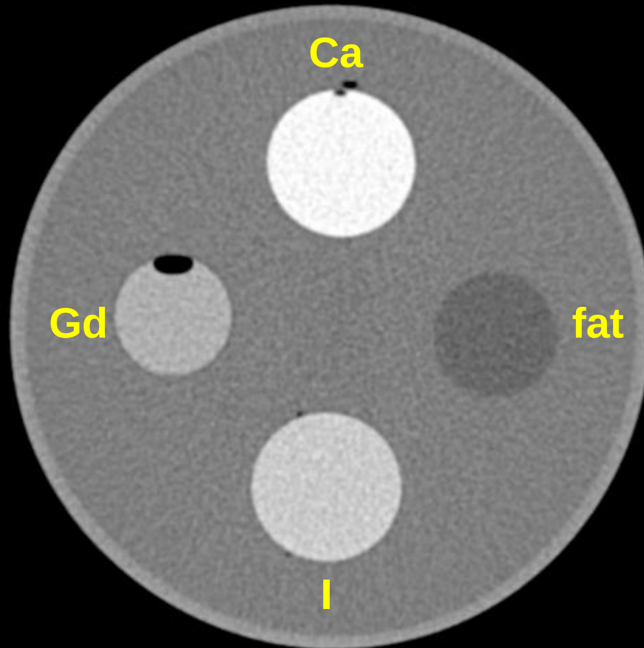

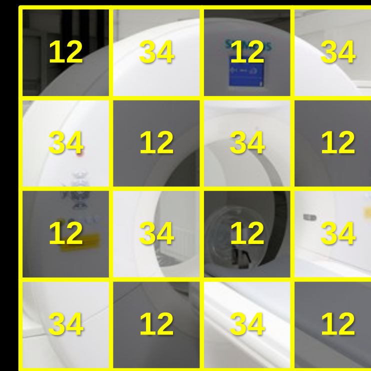

Calcium image

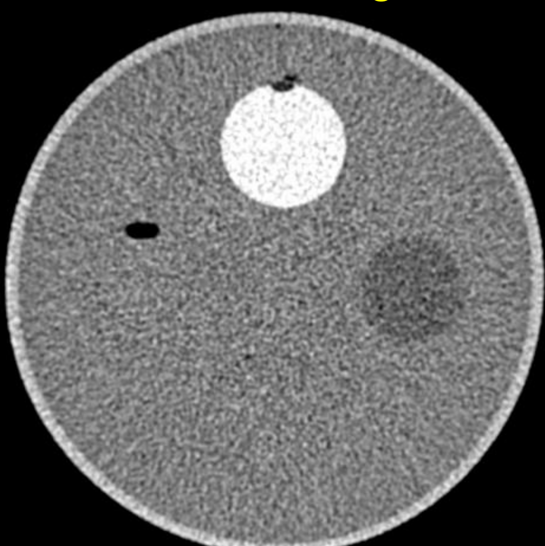

Gadolinium image

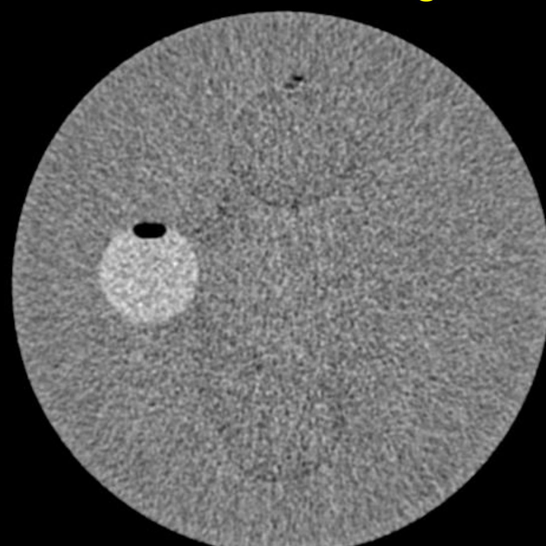

Iodine image

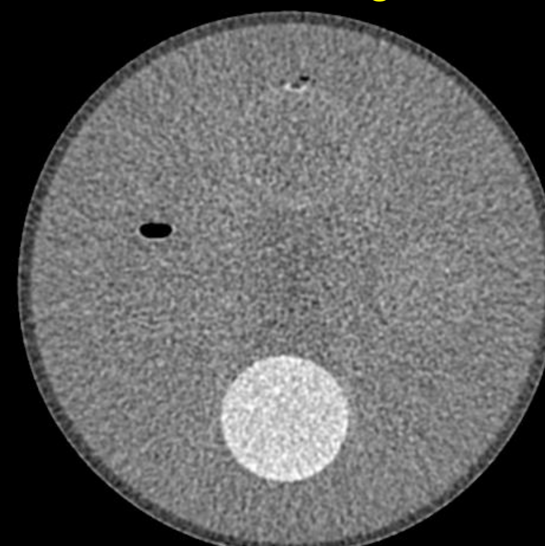

Courtesy of Siemens Healthcare

Preclinical Study

(40 kg swine, iodine contrast)

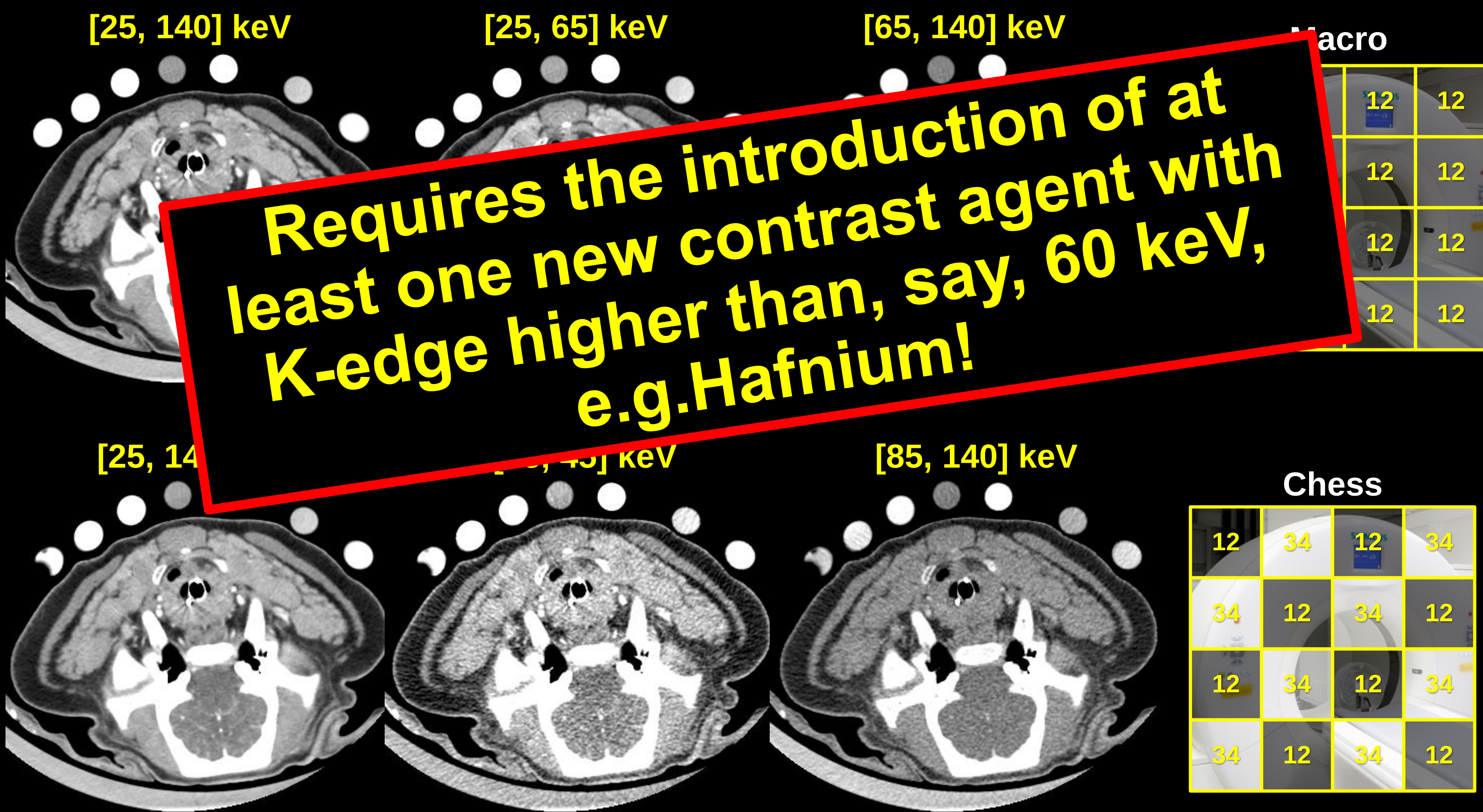

Requires the introduction of at least one new contrast agent with K-edge higher than, say, 60 keV, e.g.Hafnium!

Courtesy of Mayo Clinic Rochester, USA, and of Siemens Healthcare, Forchheim, Germany

Deep Learning in CT Image Formation

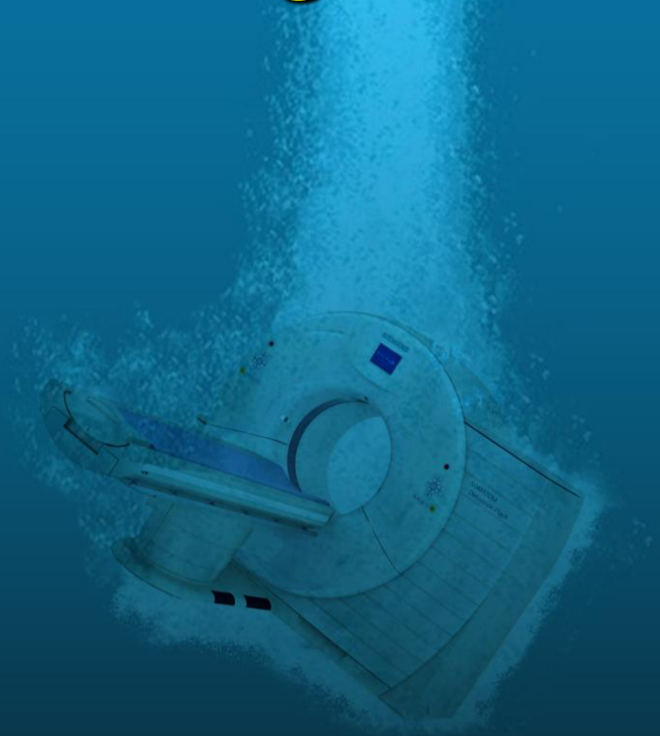

Canon‘s AiCE

- Advanced intelligent Clear-IQ Engine (AiCE)
- Trained to restore low-dose CT data to match the properties of FIRST, the model-based IR of Canon.
- FIRST is applied to high-dose CT images to obtain a high fidelity training target

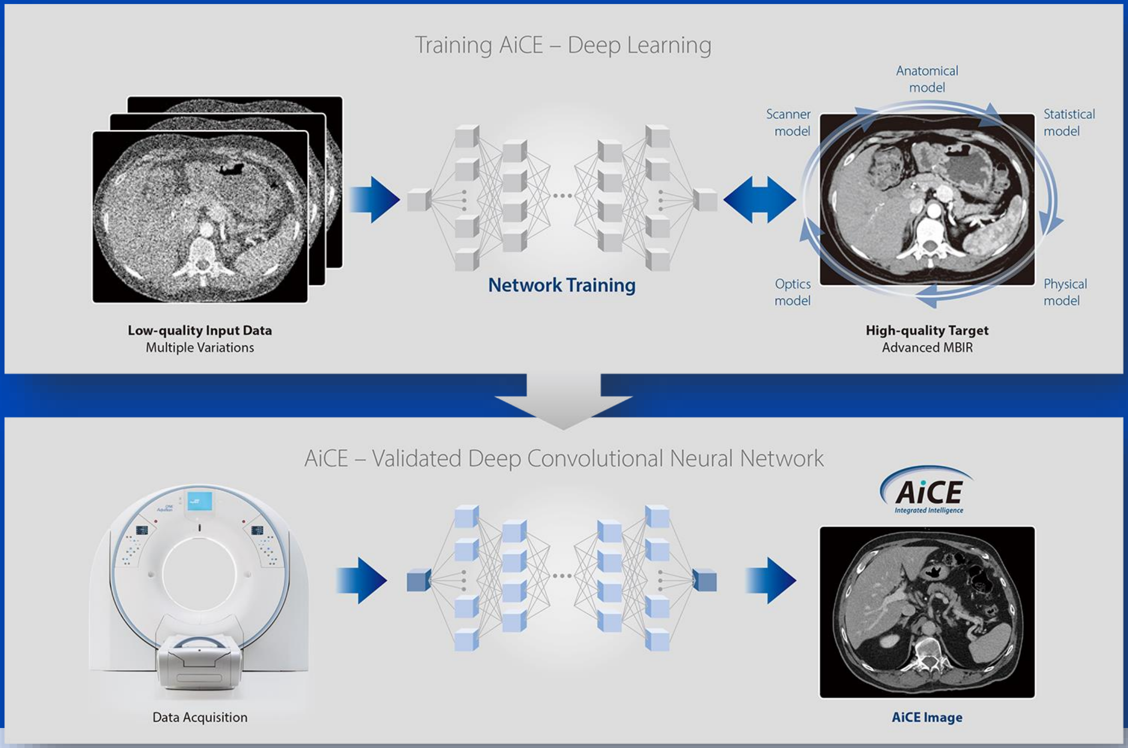

Information taken from https://global.medical.canon/products/computed-tomography/aice_dlr

U = 100 kV
CTDI = 0.6 mGy
DLP = 24.7 mGy·cm
D_{eff} = 0.35 mSv

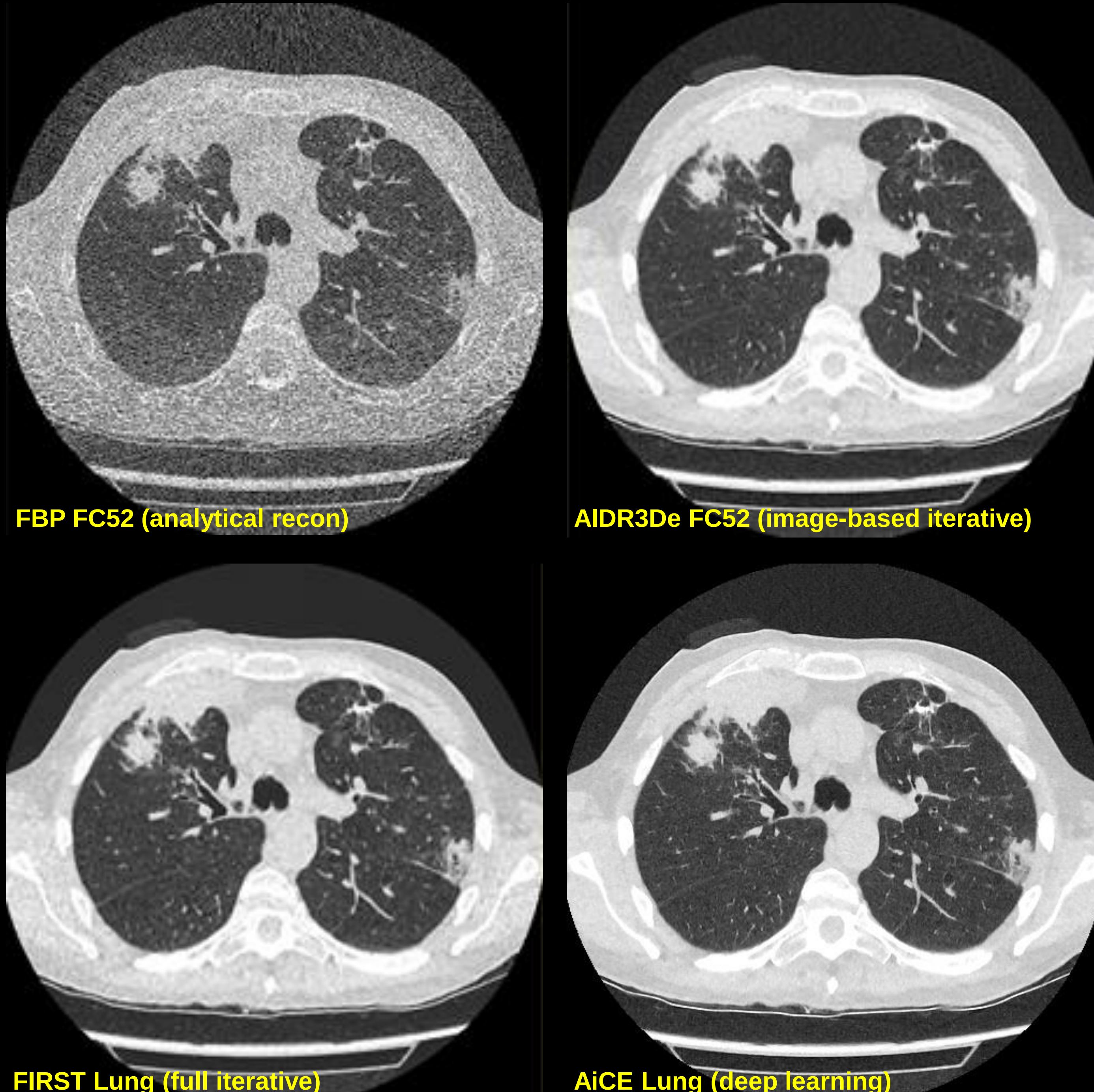

Courtesy of
Radboudumc,
the Netherlands

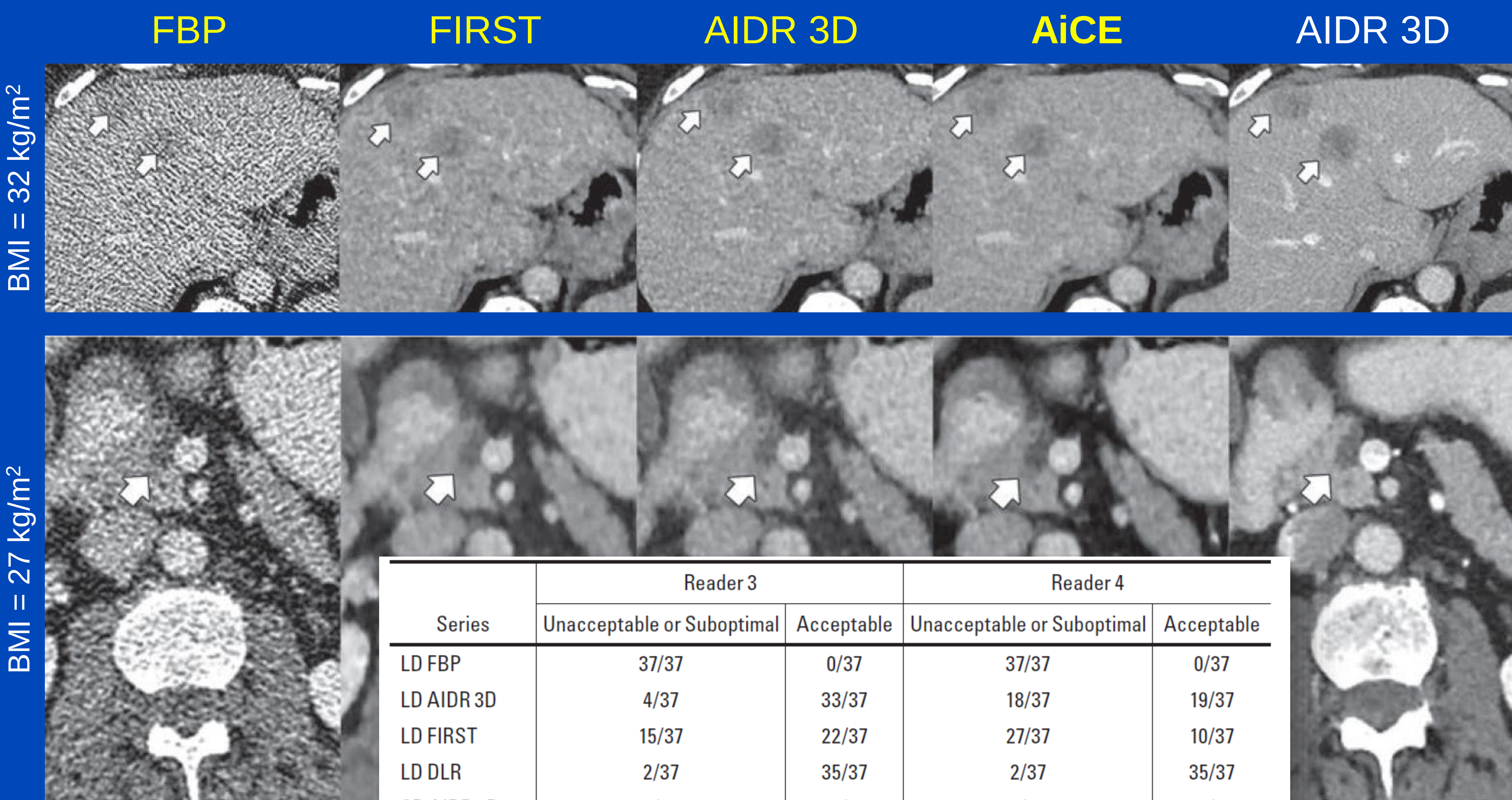

Series	Reader 3		Reader 4	
	Unacceptable or Suboptimal	Acceptable	Unacceptable or Suboptimal	Acceptable
LD FBP	37/37	0/37	37/37	0/37
LD AIDR 3D	4/37	33/37	18/37	19/37
LD FIRST	15/37	22/37	27/37	10/37
LD DLR	2/37	35/37	2/37	35/37
SD AIDR 3D	0/37	37/37	0/37	37/37

Low Dose CT
2 mGy CTDI (top)
3 mGy CTDI (bottom)

Standard Dose CT
19 mGy CTDI (top)
18 mGy CTDI (bottom)

Noise Removal Example 7
GE‘s True Fidelity

- Based on a deep CNN
- Trained to restore low-dose CT data to match the properties of Veo, the model-based IR of GE.
- No information can be obtained in how the training is conducted for the product implementation.

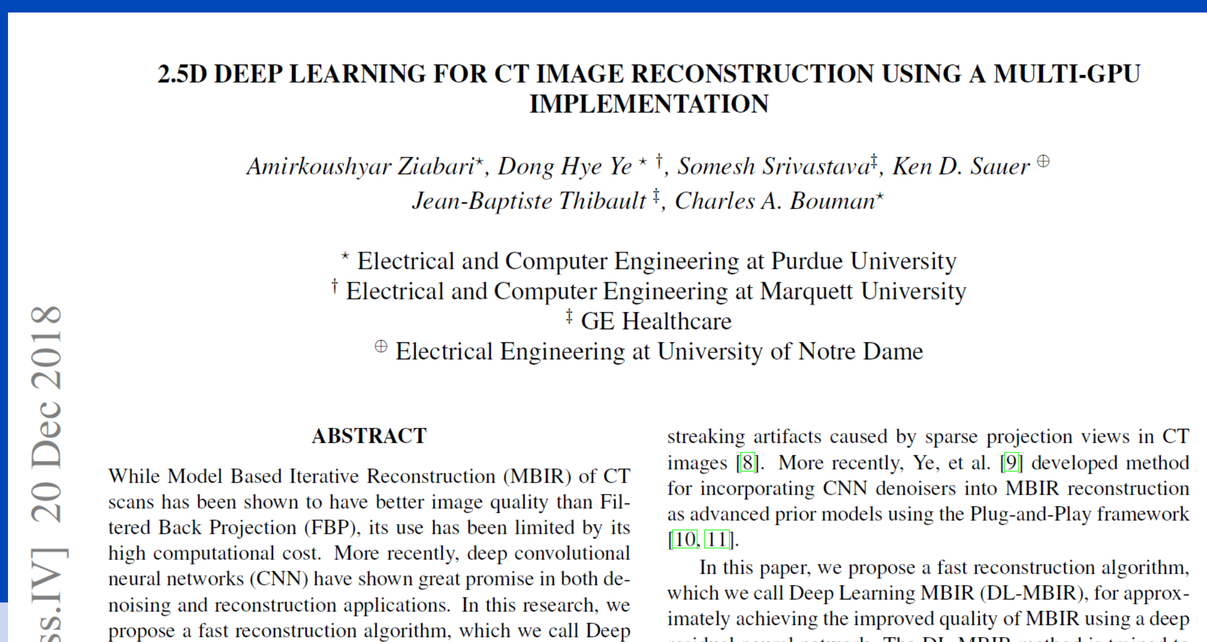

2.5D DEEP LEARNING FOR CT IMAGE RECONSTRUCTION USING A MULTI-GPU IMPLEMENTATION

Amirkoushyar Ziabari[⋆], *Dong Hye Ye*[⋆ †], *Somesh Srivastava*[‡], *Ken D. Sauer*[⊕]
Jean-Baptiste Thibault[‡], *Charles A. Bouman*[⋆]

[⋆] Electrical and Computer Engineering at Purdue University
[†] Electrical and Computer Engineering at Marquett University
[‡] GE Healthcare
[⊕] Electrical Engineering at University of Notre Dame

ABSTRACT

While Model Based Iterative Reconstruction (MBIR) of CT scans has been shown to have better image quality than Filtered Back Projection (FBP), its use has been limited by its high computational cost. More recently, deep convolutional neural networks (CNN) have shown great promise in both denoising and reconstruction applications. In this research, we propose a fast reconstruction algorithm, which we call Deep

streaking artifacts caused by sparse projection views in CT images [8]. More recently, Ye, et al. [9] developed method for incorporating CNN denoisers into MBIR reconstruction as advanced prior models using the Plug-and-Play framework [10, 11].

In this paper, we propose a fast reconstruction algorithm, which we call Deep Learning MBIR (DL-MBIR), for approximately achieving the improved quality of MBIR using a deep residual neural network. The DL-MBIR method is trained to

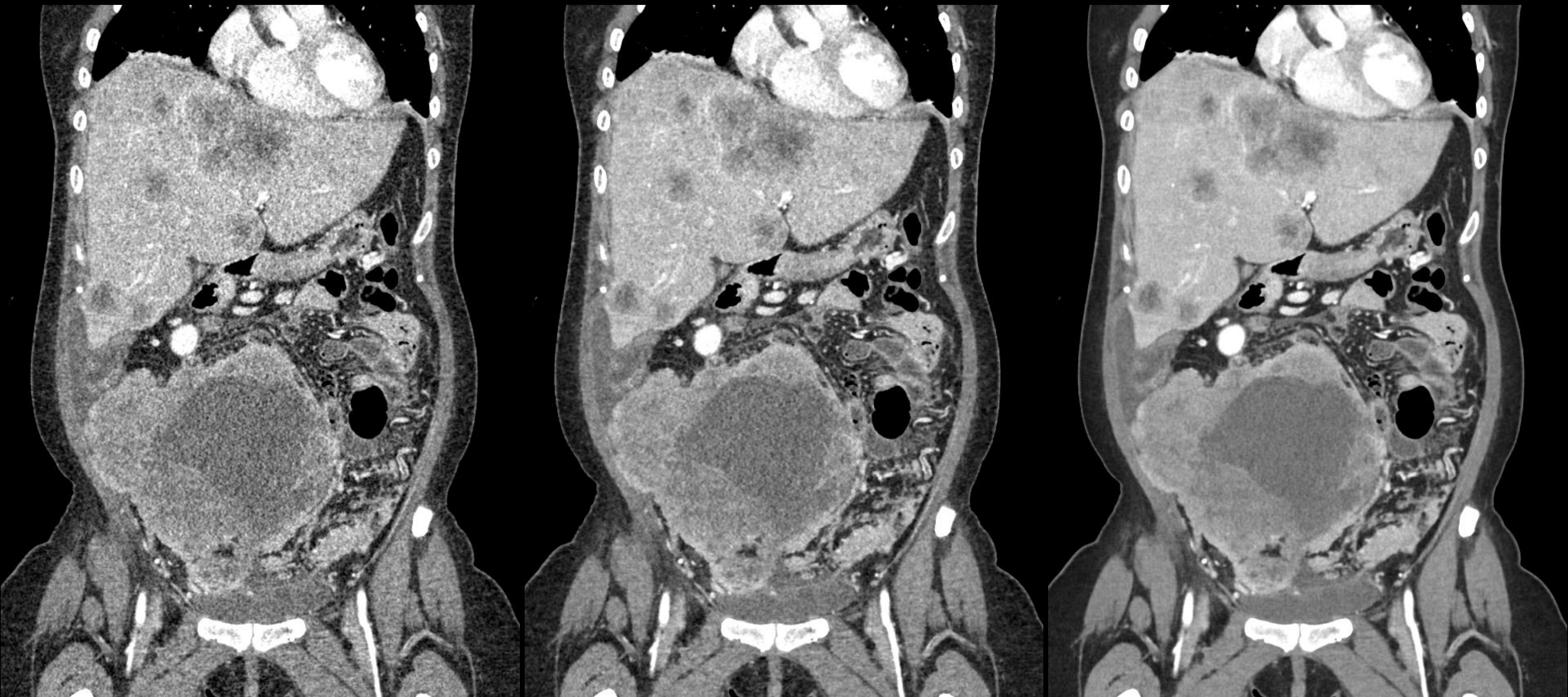

FBP **ASIR V 50%** **True Fidelity**

Deep Scatter Estimation (DSE)

TOP DOWNLOADED PAPER 2018-2019

CONGRATULATIONS TO

Marc Kachelriess

whose paper has been recognized as
one of the most read in

Medical Physics

WILEY

MEDICAL PHYSICS

The International Journal of Medical Physics Research and Practice

Congratulations — your work was one of the top downloaded in recent publication history!

Dear MARC,

We are excited to share that your research, published in *Medical Physics*, is among the top 10% most downloaded papers!

- **Real-time scatter estimation for medical CT using the deep ... imation: Method and robustness analysis with ... different anatomies, dose levels, tube voltages, and ... tion**

This work received the
Behnken-Berger Award
at the DGMP annual meeting 2021

TOP DOWNLOADED PAPER 2018-2019

CONGRATULATIONS TO

Joscha Maier

whose paper has been recognized as
one of the most read in

Medical Physics

Motivation

- X-ray scatter is a major cause of image quality degradation in CT and CBCT.
- Appropriate scatter correction is crucial to maintain the diagnostic value of the CT examination.

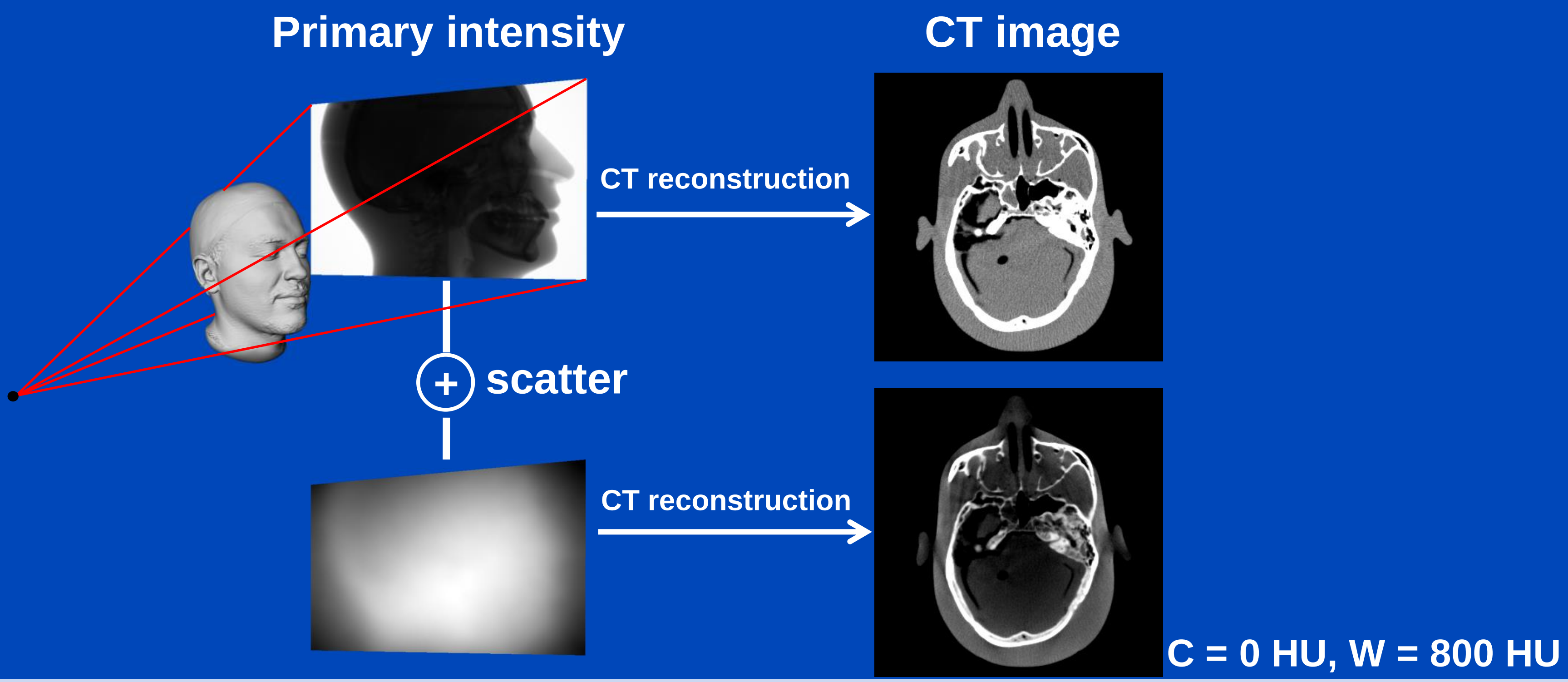

Monte Carlo Scatter Estimation

- Simulation of photon trajectories according to physical interaction probabilities.
- Simulating a large numb ries well approximat

1 to 10 hours per tomographic data set

mplete scatter distribution

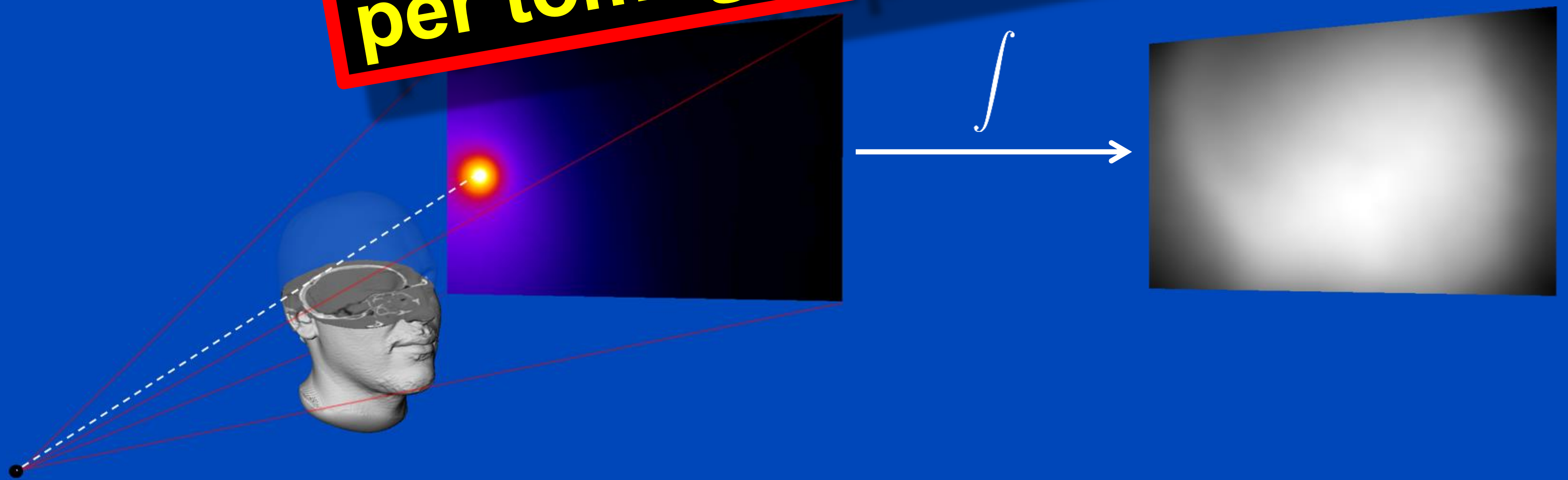

Deep Scatter Estimation

Network architecture & scatter estimation framework

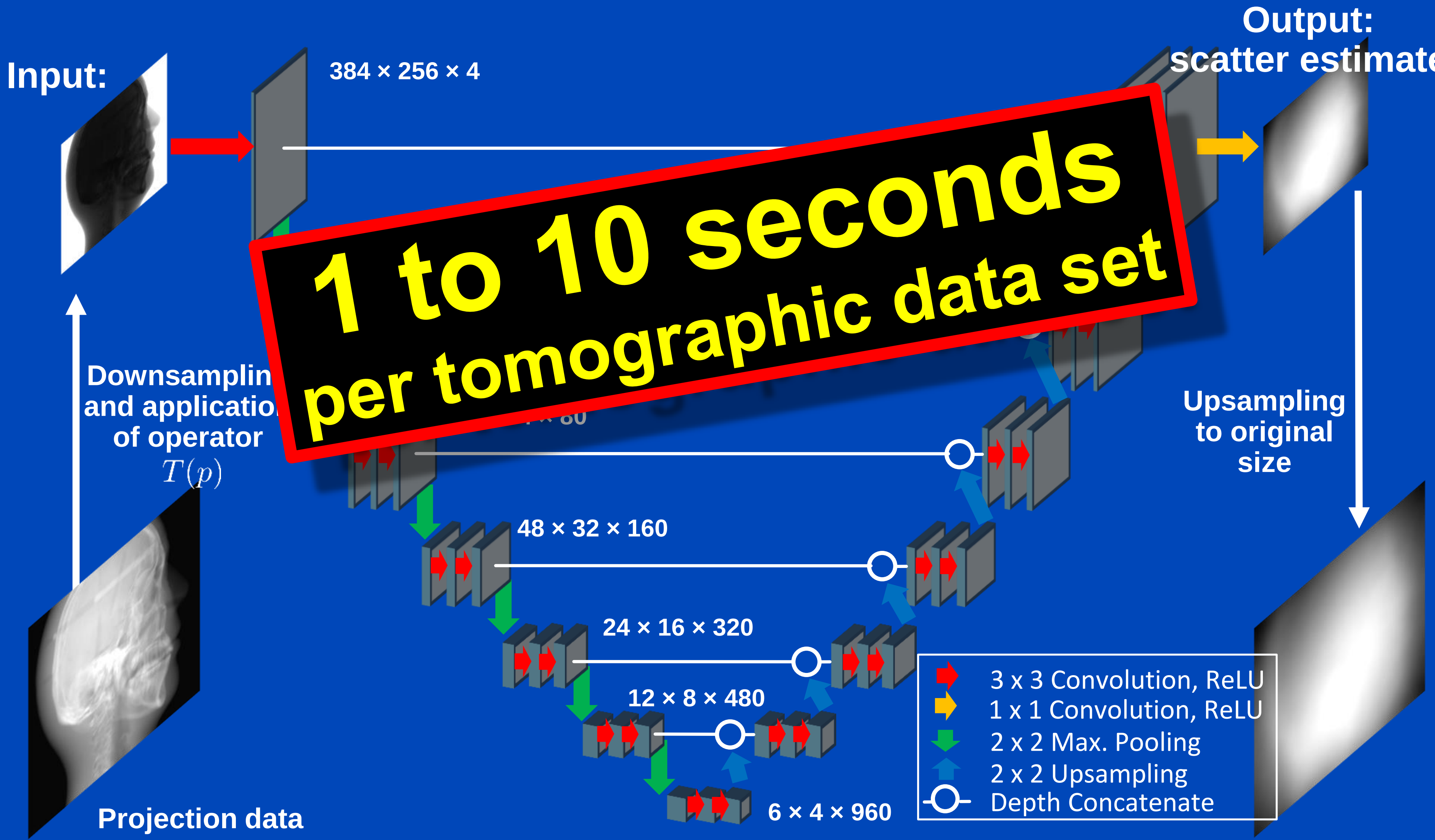

J. Maier, M. Kachelrieß et al. Deep scatter estimation (DSE). SPIE 2017 and Journal of Nondestructive Evaluation 37:57, July 2018.
J. Maier, M. Kachelrieß et al. Robustness of DSE. Med. Phys. 46(1):238-249, January 2019.

Results on Simulated Projection Data

Primary intensity | Scatter ground truth (GT) | (Kernel – GT) / GT | (Hybrid - GT) / GT | (DSE – GT) / GT

View #1
View #2
View #3
View #4
View #5

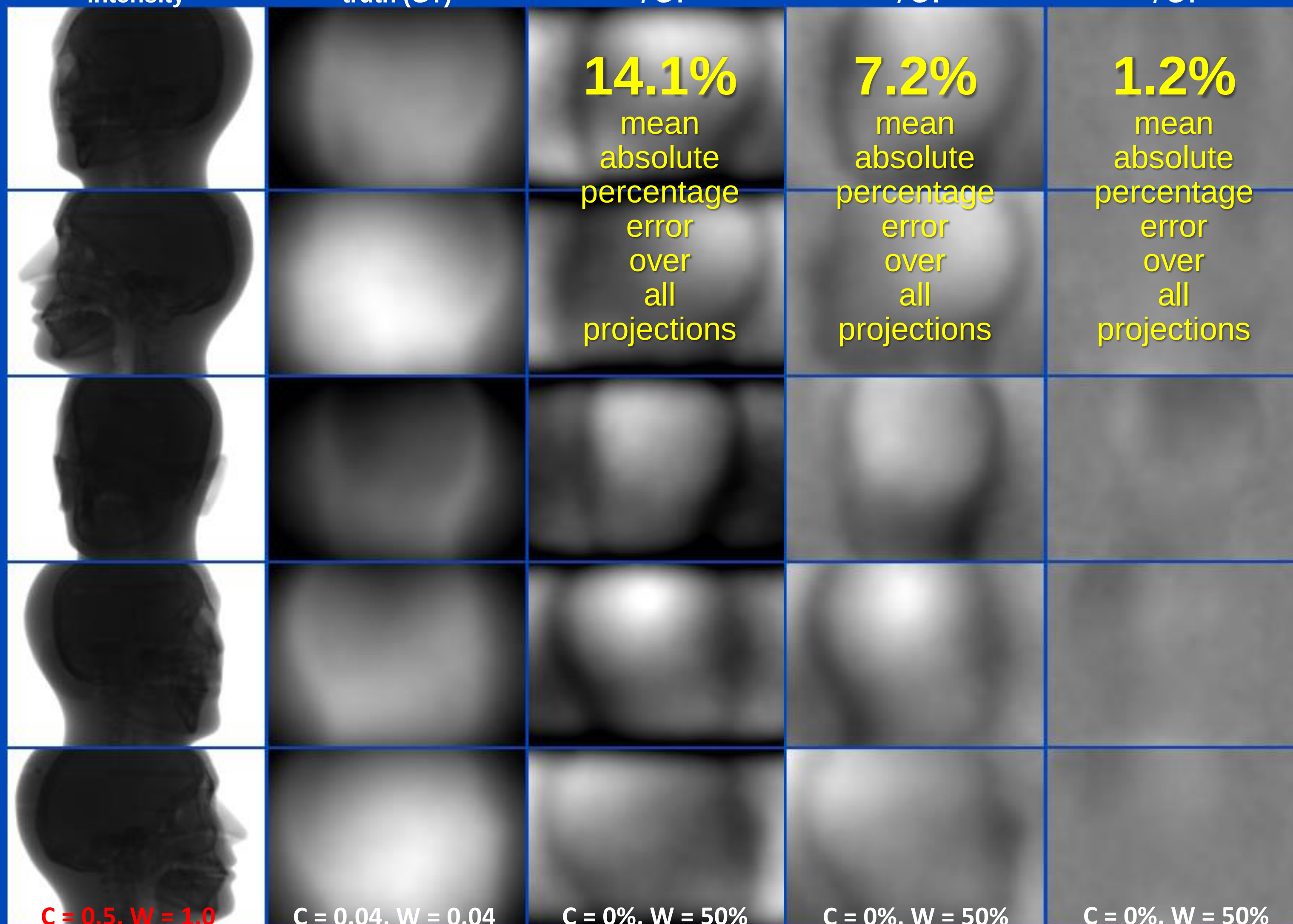

DSE trained to estimate scatter from **primary plus scatter**: High accuracy

Results on Simulated Projection Data

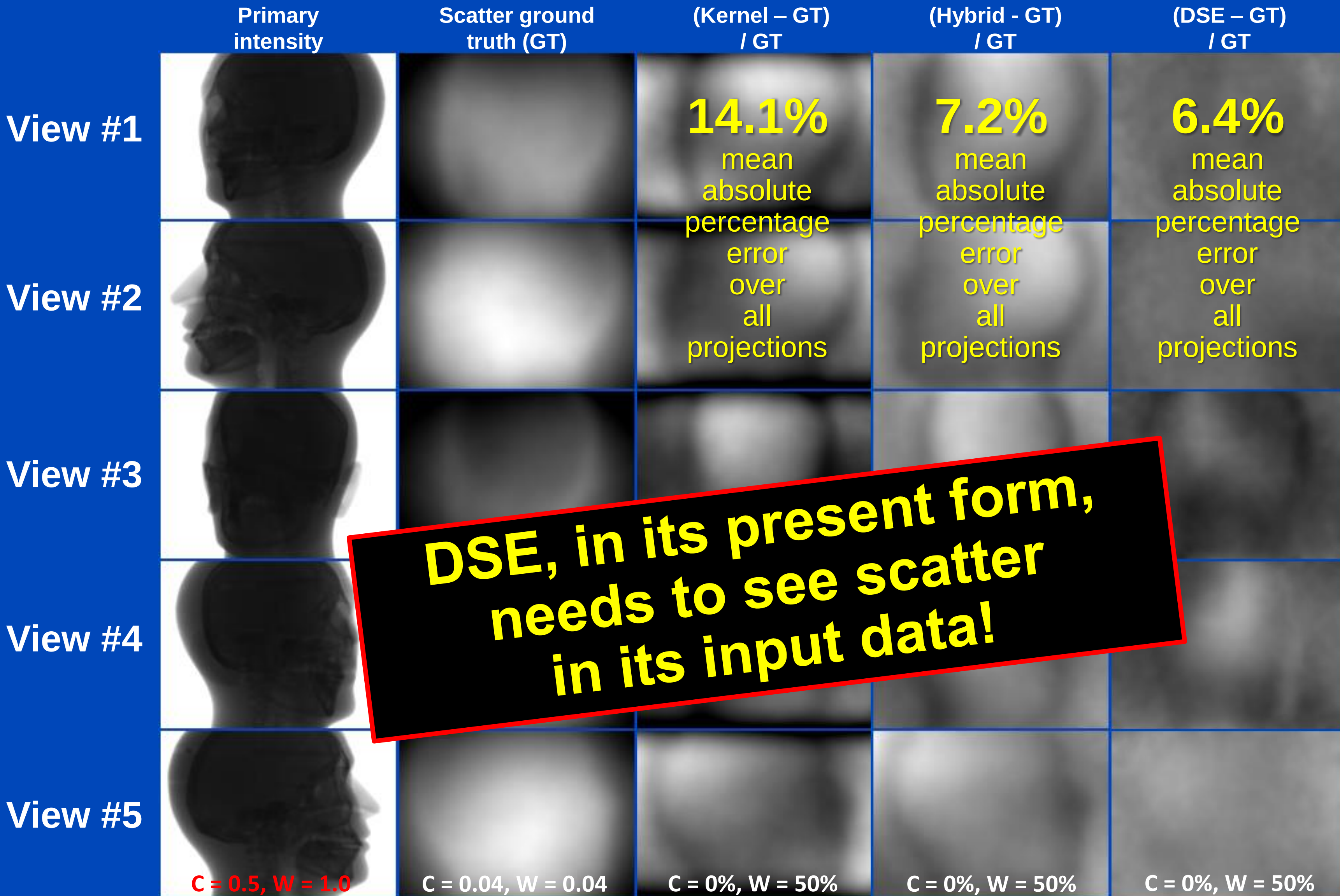

DSE trained to estimate scatter from **primary only**: Low accuracy

Results on Simulated Projection Data

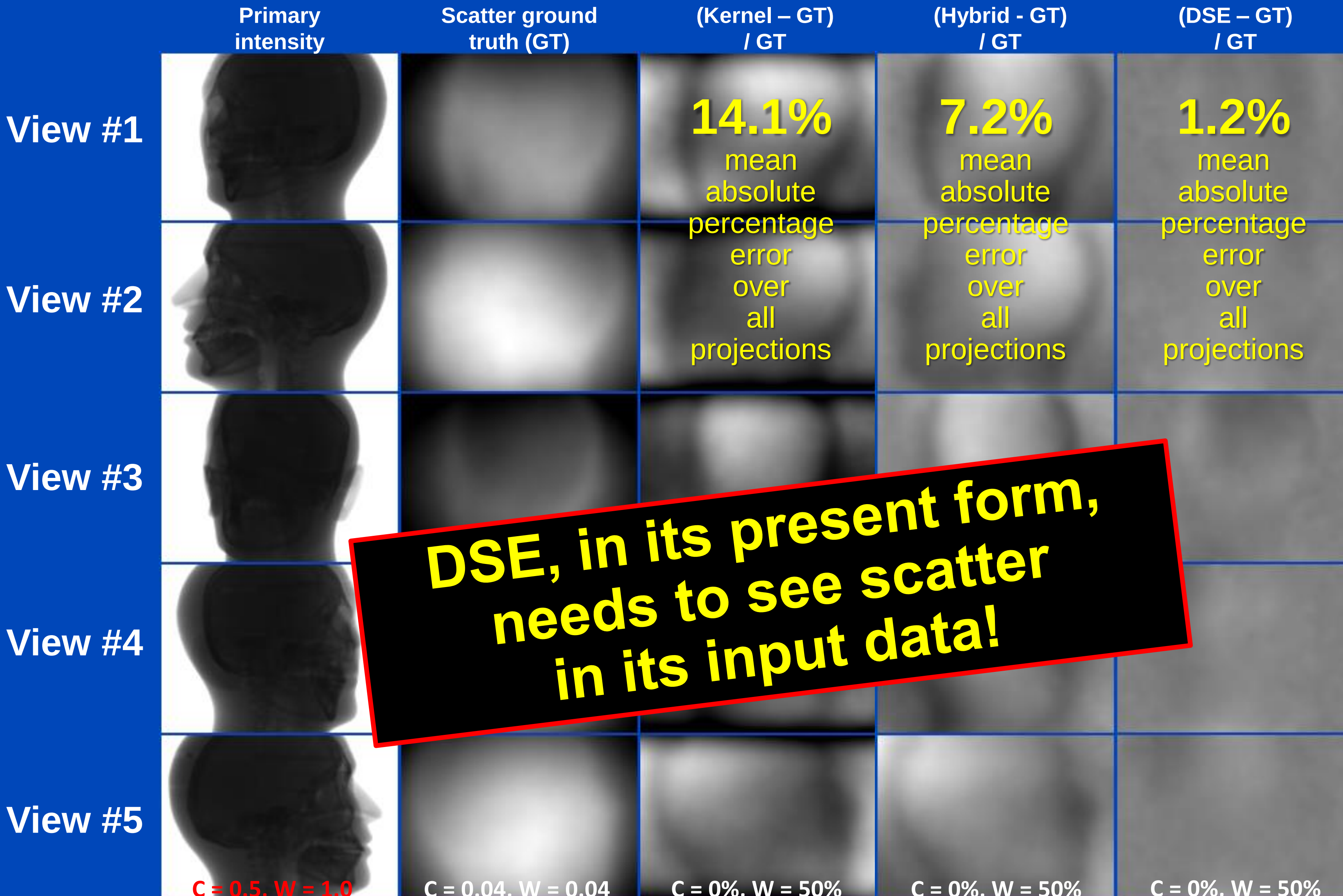

DSE trained to estimate scatter from **primary plus scatter**: High accuracy

Reconstructions of Simulated Data

Ground Truth | No Correction | Kernel-Based Scatter Estimation | Hybrid Scatter Estimation | Deep Scatter Estimation

CT Reconstruction

Difference to ideal simulation

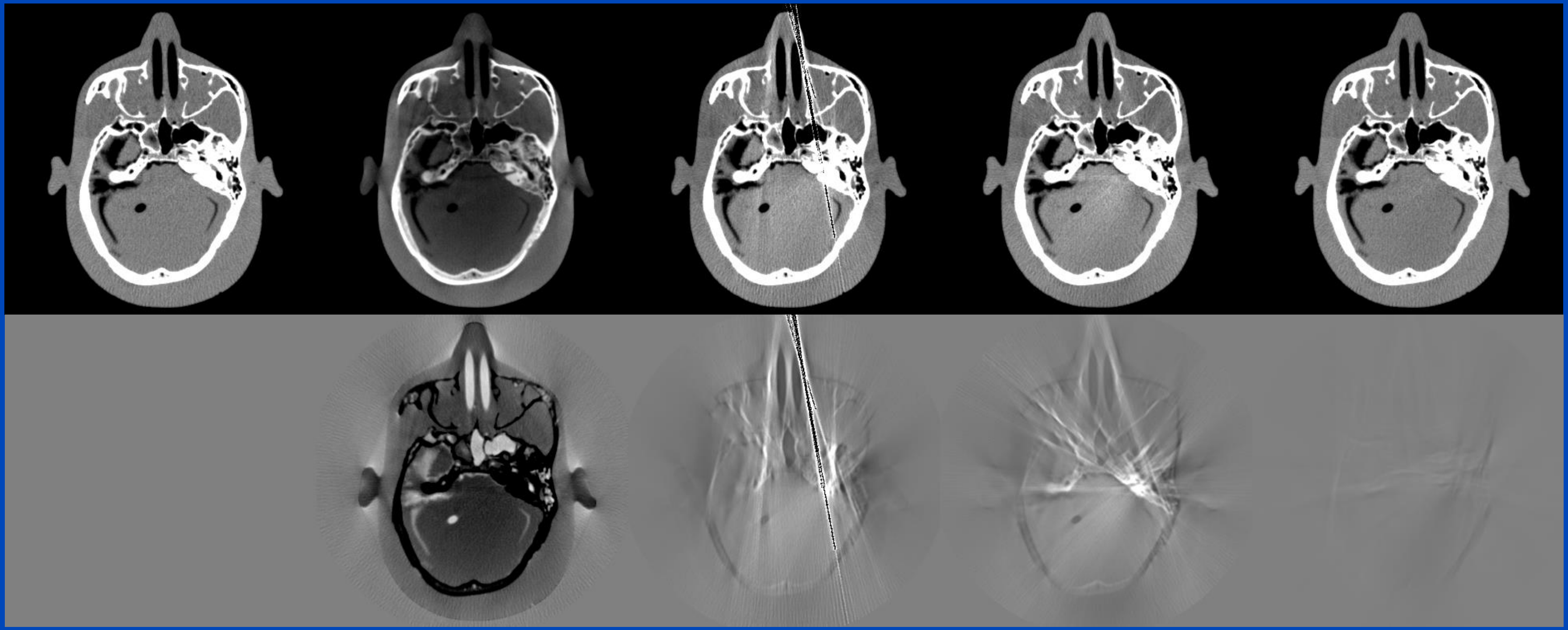

C = 0 HU, W = 1000 HU

J. Maier, M. Kachelrieß et al. Deep scatter estimation (DSE). SPIE 2017 and Journal of Nondestructive Evaluation 37:57, July 2018.
J. Maier, M. Kachelrieß et al. Robustness of DSE. Med. Phys. 46(1):238-249, January 2019.

Testing of the DSE Network for Measured Data (120 kV)

DKFZ table-top CT

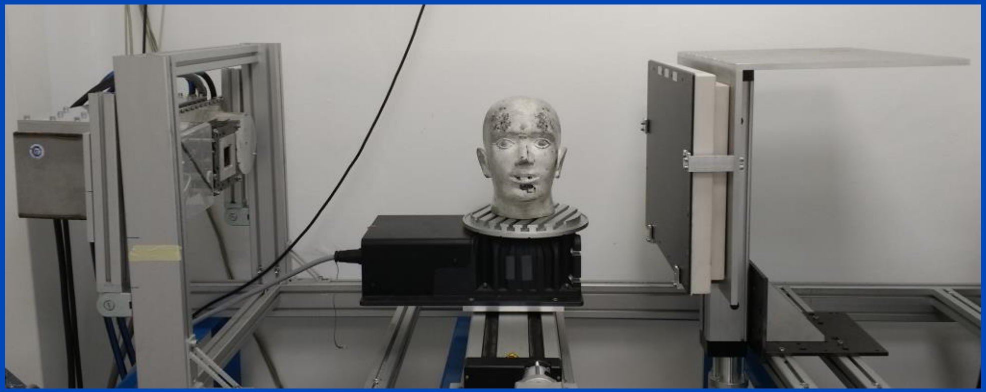

- Measurement of a head phantom at our in-house table-top CT.
- Slit scan measurement serves as ground truth.

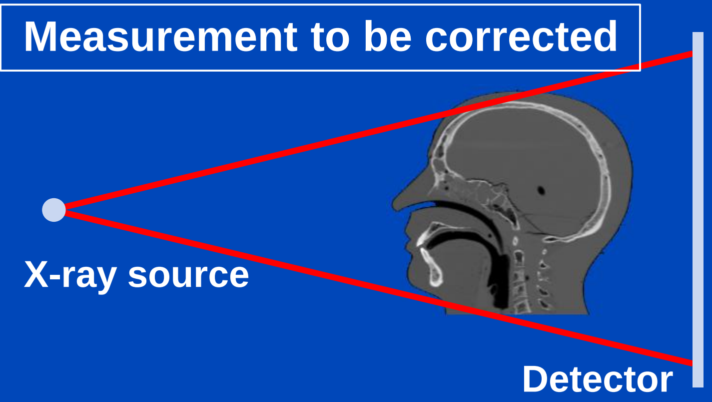

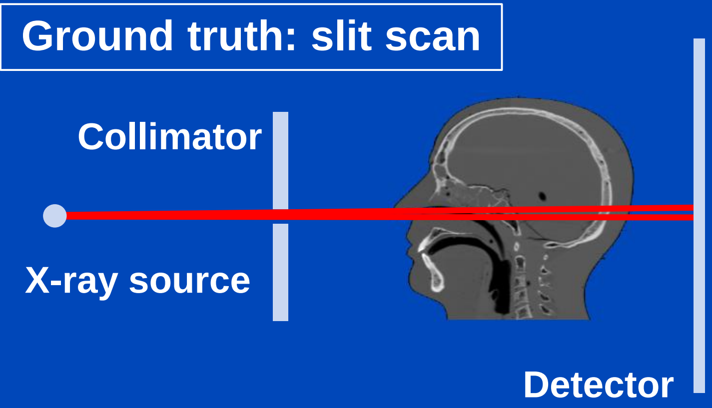

J. Maier, M. Kachelrieß et al. Deep scatter estimation (DSE). SPIE 2017 and Journal of Nondestructive Evaluation 37:57, July 2018.
J. Maier, M. Kachelrieß et al. Robustness of DSE. Med. Phys. 46(1):238-249, January 2019.

Reconstructions of Measured Data

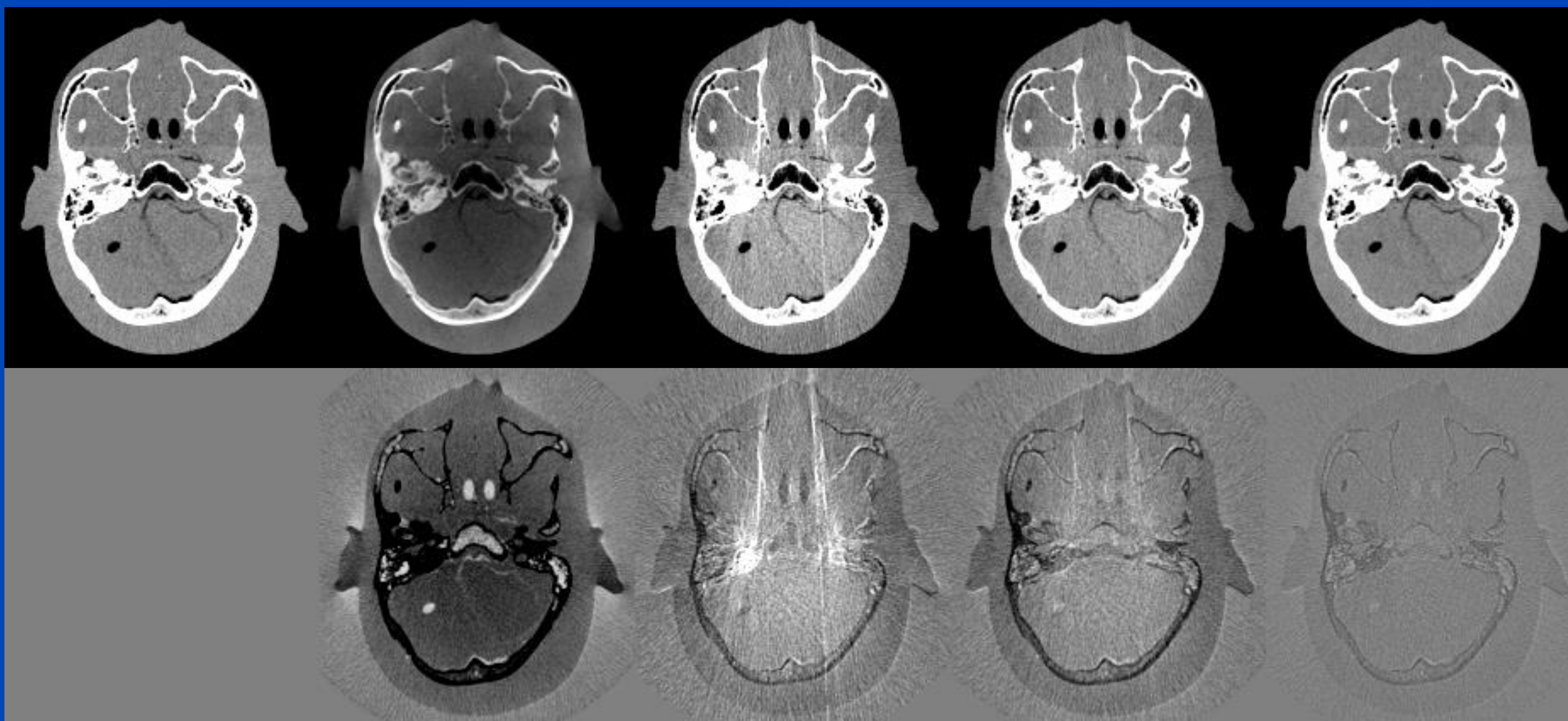

C = 0 HU, W = 1000 HU

J. Maier, M. Kachelrieß et al. Deep scatter estimation (DSE). SPIE 2017 and Journal of Nondestructive Evaluation 37:57, July 2018.
J. Maier, M. Kachelrieß et al. Robustness of DSE. Med. Phys. 46(1):238-249, January 2019.

A simple detruncation was applied to the rawdata before reconstruction. Images were clipped to the FOM before display. C = -200 HU, W = 1000 HU.

Truncated DSE

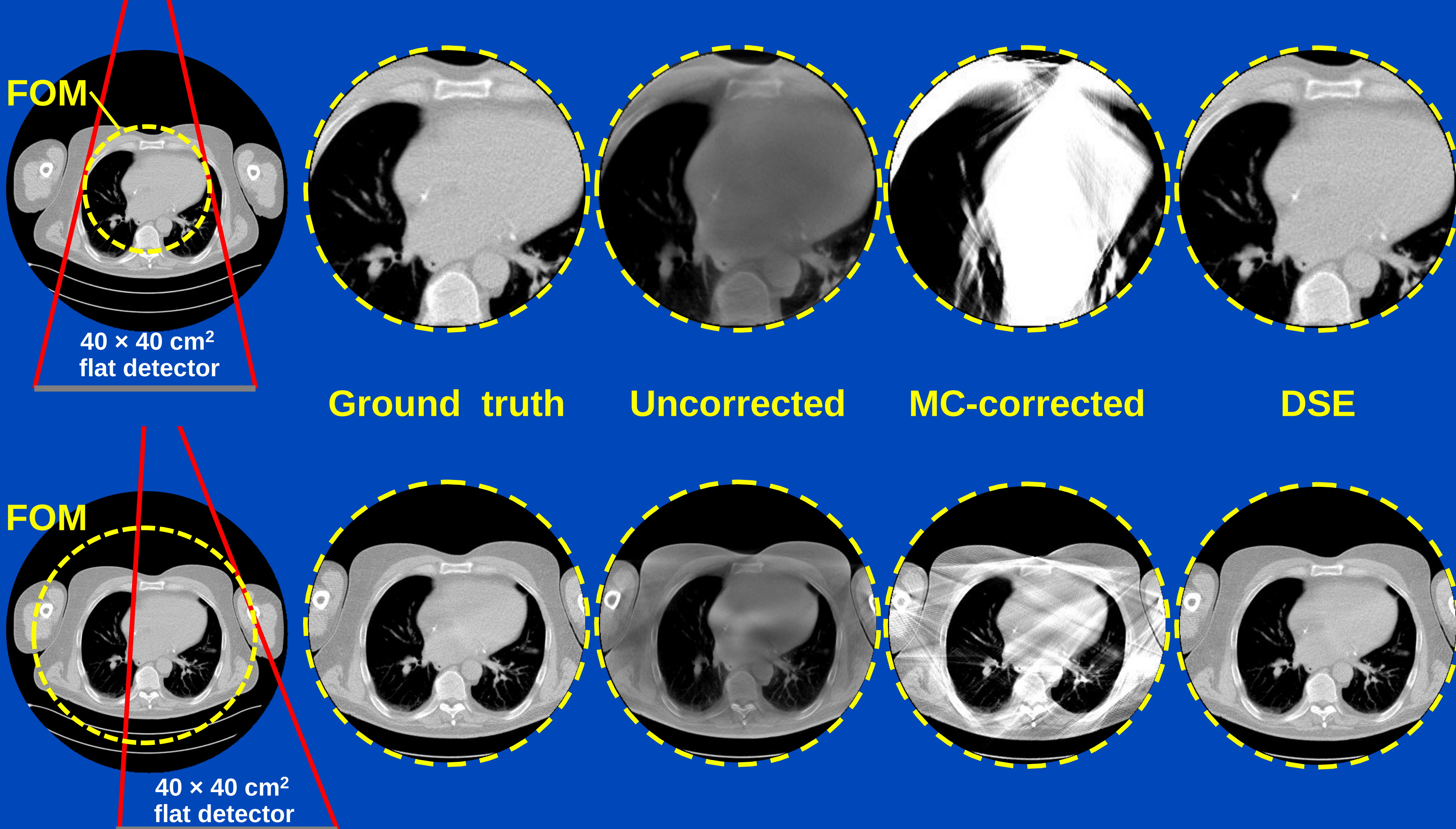

To learn why MC fails at truncated data and what significant efforts are necessary to cope with that situation see [Kachelrieß et al. Effect of detruncation on the accuracy of MC-based scatter estimation in truncated CBCT. Med. Phys. 45(8):3574-3590, August 2018].

J. Maier, M. Kachelrieß et al. Deep scatter estimation (DSE). SPIE 2017 and Journal of Nondestructive Evaluation 37:57, July 2018.
J. Maier, M. Kachelrieß et al. Robustness of DSE. Med. Phys. 46(1):238-249, January 2019.

Conclusions on DSE

- DSE needs about 3 ms per CT and 10 ms per CBCT projection (as of 2020).
- DSE is a fast and accurate alternative to MC simulations.
- DSE outperforms kernel-based approaches in terms of accuracy and speed.
- Facts:
  - DSE can estimate scatter from a single (!) x-ray image.
  - DSE can accurately estimate scatter from a primary+scatter image.
  - DSE generalizes to all anatomical regions.
  - DSE works for geometries and beam qualities differing from training.
  - DSE may outperform MC even though DSE is trained with MC.
- DSE is not restricted to reproducing MC scatter estimates.
- DSE can rather be trained with any other scatter estimate, including those based on measurements.

J. Maier, M. Kachelrieß et al. Deep scatter estimation (DSE). SPIE 2017 and Journal of Nondestructive Evaluation 37:57, July 2018.
J. Maier, M. Kachelrieß et al. Robustness of DSE. Med. Phys. 46(1):238-249, January 2019.

Deep Dose Estimation

???

In real time?

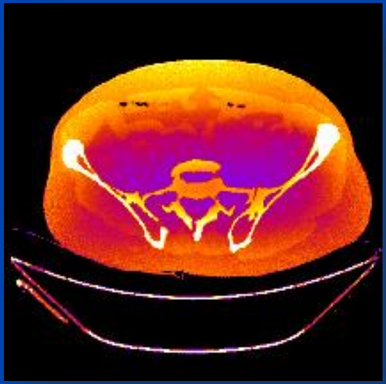

MC Dose Simulation for a 360° Scan

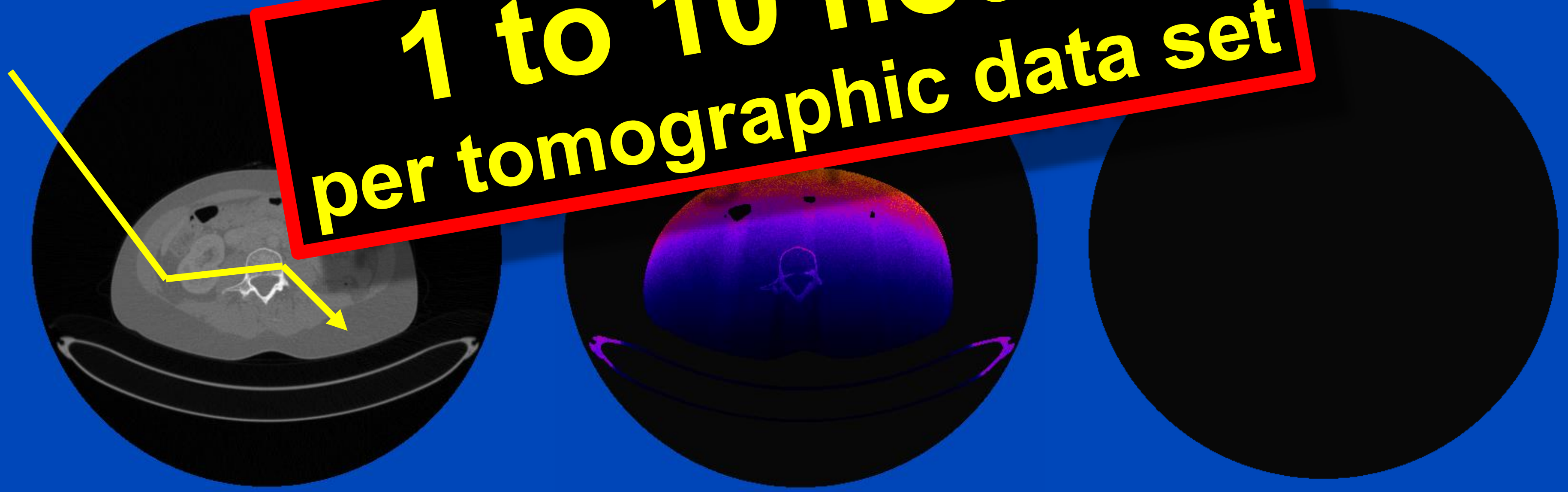

1 to 10 hours
per tomographic data set

J. Maier, L. Klein, E. Eulig, S. Sawall, and M. Kachelrieß. Real-time estimation of patient-specific dose distributions for medical CT using the deep dose estimation. Med. Phys. 49(4):2259-2269, April 2022. *Best Paper within Machine Learning at ECR 2019!*

Deep Dose Estimation (DDE)

- Combine fast and accurate CT dose estimation using a deep convolutional neural network.
- Train the network to re… …mates given the CT … …mate.

1 to 10 seconds per tomographic data set

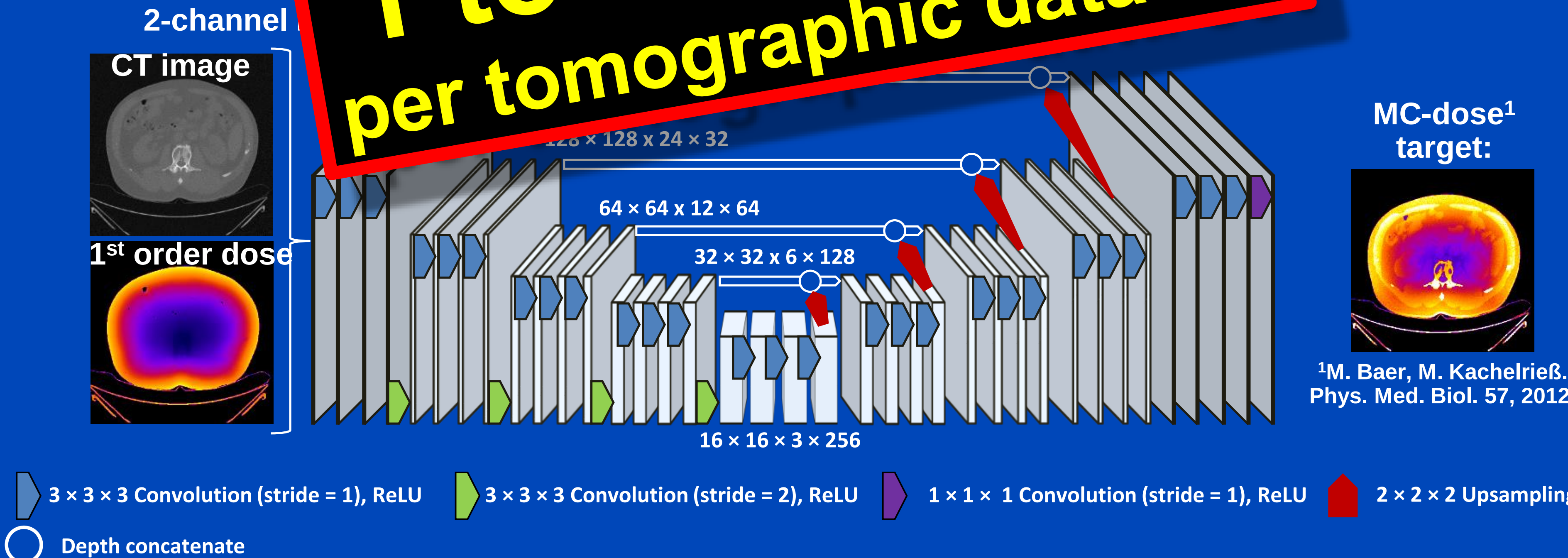

[1]M. Baer, M. Kachelrieß. Phys. Med. Biol. 57, 2012.

Results

Thorax, tube A, 120 kV, with bowtie

CT image

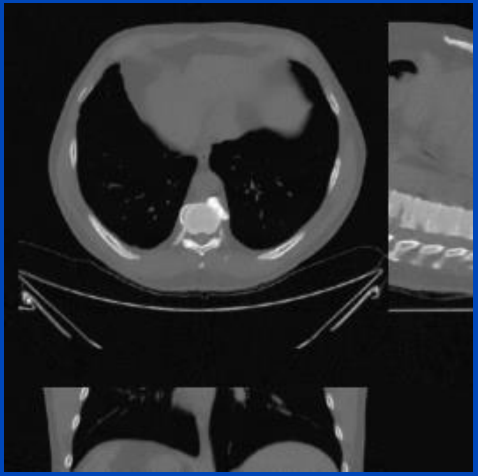

First order dose

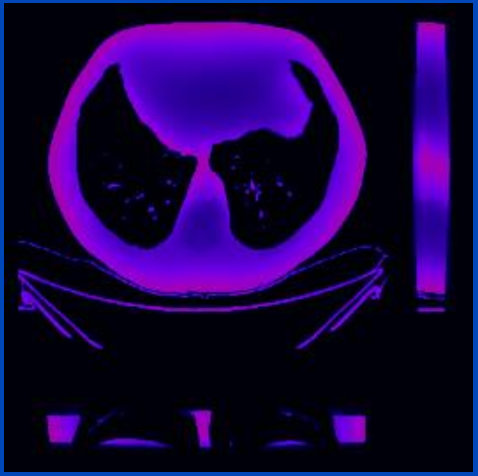

	MC	DDE
48 slices	1 h	0.25 s
whole body	20 h	5 s

MC uses 16 CPU kernels
DDE uses one Nvidia Quadro P600 GPU

DDE training took 74 h for 300 epochs, 1440 samples, 48 slices per sample

MC ground truth

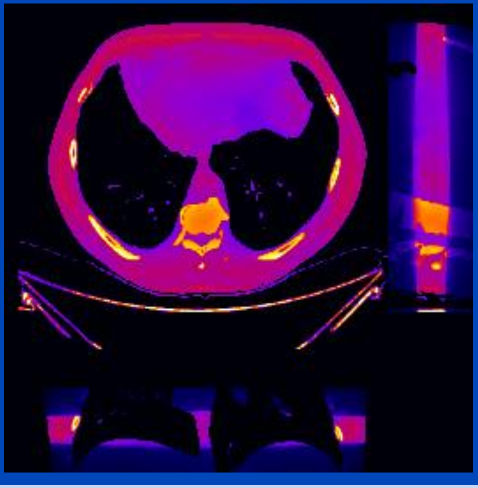

DDE

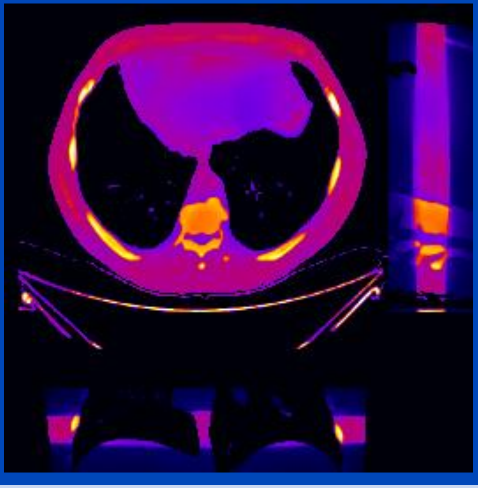

Relative error

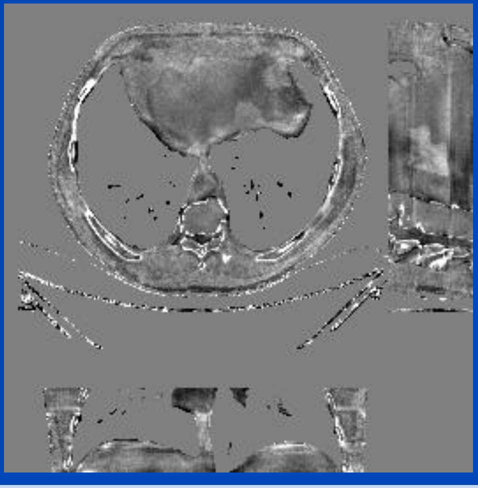

C = 0%
W = 40%

J. Maier, L. Klein, E. Eulig, S. Sawall, and M. Kachelrieß. Real-time estimation of patient-specific dose distributions for medical CT using the deep dose estimation. Med. Phys. 49(4):2259-2269, April 2022. *Best Paper within Machine Learning at ECR 2019!*

Results

Thorax, tube A, 120 kV, no bowtie

CT image

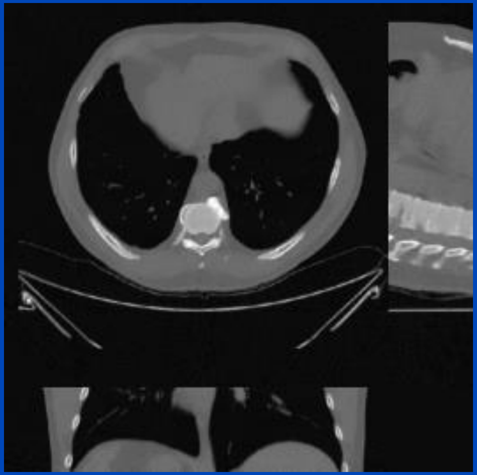

First order dose

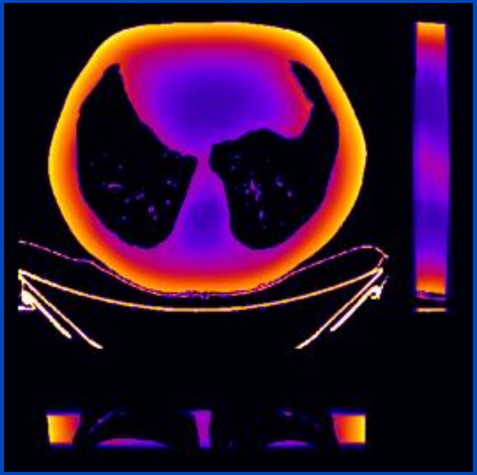

	MC	DDE
48 slices	1 h	0.25 s
whole body	20 h	5 s

MC uses 16 CPU kernels
DDE uses one Nvidia Quadro P600 GPU

DDE training took 74 h for 300 epochs, 1440 samples, 48 slices per sample

MC ground truth

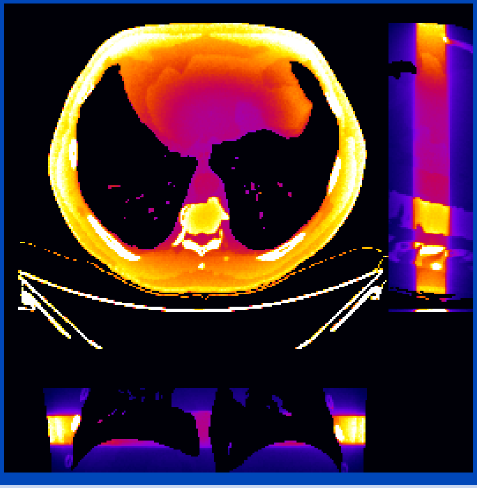

DDE

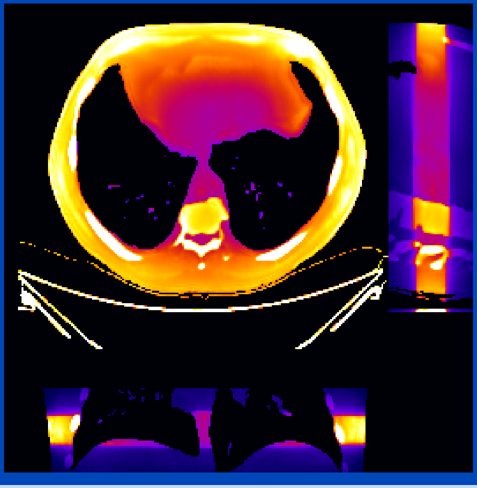

Relative error

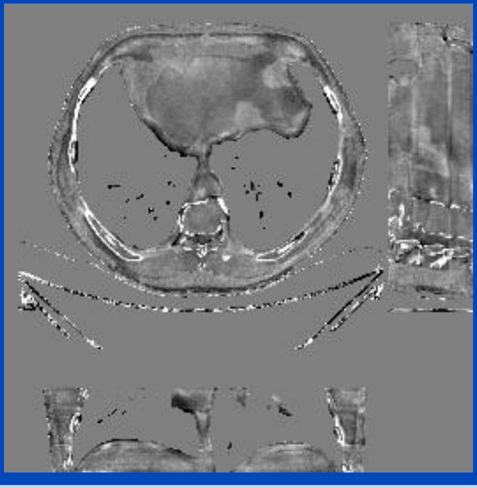

C = 0%
W = 40%

J. Maier, L. Klein, E. Eulig, S. Sawall, and M. Kachelrieß. Real-time estimation of patient-specific dose distributions for medical CT using the deep dose estimation. Med. Phys. 49(4):2259-2269, April 2022. *Best Paper within Machine Learning at ECR 2019!*

dkfz.

Results

Thorax, tube B, 120 kV, no bowtie

CT image

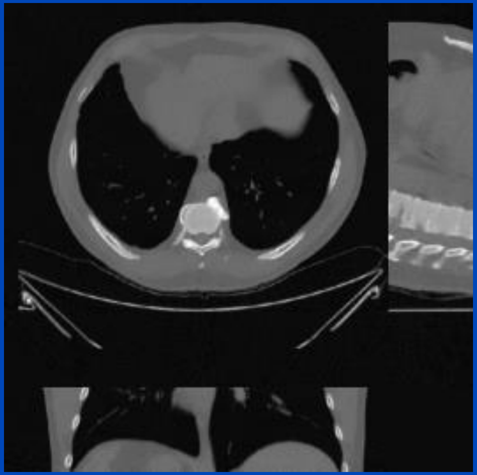

First order dose

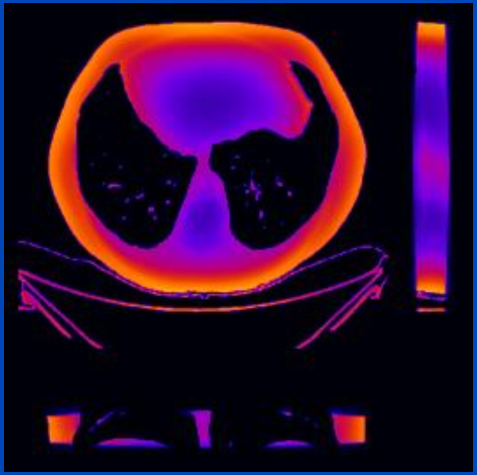

	MC	DDE
48 slices	1 h	0.25 s
whole body	20 h	5 s

MC uses 16 CPU kernels
DDE uses one Nvidia Quadro P600 GPU

DDE training took 74 h for 300 epochs, 1440 samples, 48 slices per sample

MC ground truth

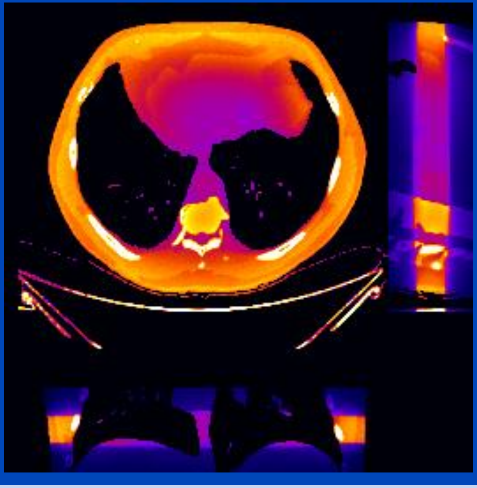

DDE

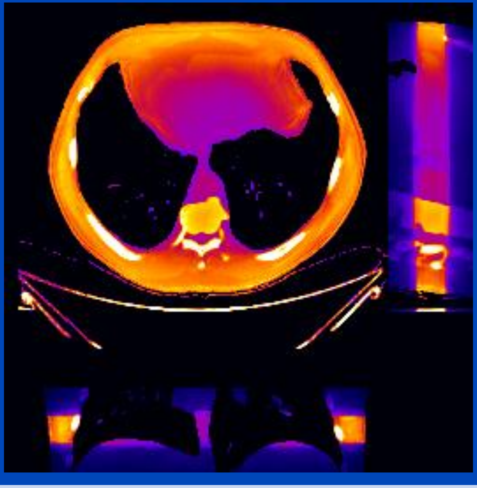

Relative error

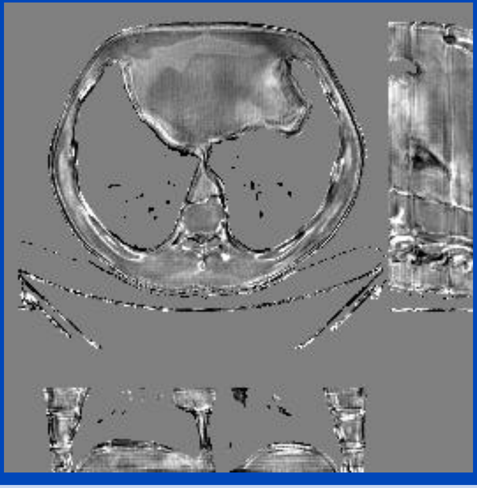

C = 0%
W = 40%

J. Maier, L. Klein, E. Eulig, S. Sawall, and M. Kachelrieß. Real-time estimation of patient-specific dose distributions for medical CT using the deep dose estimation. Med. Phys. 49(4):2259-2269, April 2022. *Best Paper within Machine Learning at ECR 2019!*

Conclusions on DDE

- DDE provides accurate dose predictions
  - for circle scans
  - for sequence scans
  - for partial scans (less than 360°)
  - for limited angle scans (less than 180°)
  - for spiral scans
  - for different tube voltages
  - for scans with and without bowtie filtration
  - for scans with tube current modulation
- In practice it may therefore be not necessary to perform separate training runs for these cases.
- Thus, accurate real-time patient dose estimation may become feasible with DDE.

J. Maier, L. Klein, E. Eulig, S. Sawall, and M. Kachelrieß. Real-time estimation of patient-specific dose distributions for medical CT using the deep dose estimation. Med. Phys. 49(4):2259-2269, April 2022. *Best Paper within Machine Learning at ECR 2019!*

Reconstruct from 1 or 2 Projections

- P. Henzler, V. Rasche, T. Ropinski, and T. Ritschel. Single-image Tomography: 3D Volumes from 2D X-Rays: 3D Volumes from 2D Cranial X-Rays. Computer Graphics Forum. 37(2):377-388, 2018.
  - *N*=1, mainly sculls in air but also mouse with soft tissue
  - modified U-Net without reducing the number of features in the decoder (2D -> 3D)
- Li Jiang, Shaoshuai Shi, Xiaojuan Qi, and Jiaya Jia. GAL: Geometric Adversarial Loss for Single-View 3D-Object Reconstruction. In: ECCV 2018 Lecture Notes in Computer Science 11212:820-834, 2018.
  - *N*=1, object shapes from photography
  - GAN-type network
- Yuan Xu, Hao Yan, Luo Ouyang, Jing Wang, Linghong Zhou, Laura Cervino, Steve B. Jiang, and Xun Jia. A Method for Volumetric Imaging in Radiotherapy using Single X-Ray Projection. Med. Phys. 42(5):2498-2509, 2015
  - *N*=1. Derives MVFs from an x-ray projection that are then applied to a 3D CBCT volume
  - Sparse learning
- Liyue Shen, Wei Zhao, and Lei Xing. Patient-Specific Reconstruction of Volumetric Computed Tomography Images from a Single Projection View via Deep Learning. Nat. Biomed. Eng. 3:880–888, 2019.
  - *N*=1. Training and validation in the same patient. Example 1: train on 6 phases of 4D CT and test on the remaining 4 phases. Example 2: train on 4D CT of day 1 and test on 4D CT of day 2.
    2D encoder CNN, 2D->3D FCN, 3D decoder CNN.
- Xingde Ying, Heng Guo, Kai Ma, Jian Wu, Zhengxin Weng, and Yefeng Zheng. X2CT-GAN: Reconstructing CT from Biplanar X-Rays with Generative Adversarial Networks. arXiv:1905.06902v1, May 2019
  - *N*=2. Thorax cases
  - GAN with U-Net-type generator whose skips are backprojections.
- Diogo F. Almeida, Patricio Astudillo, and Dirk Vandermeulen. 3D Image Volumes From 2D Digitally Reconstructed X-Rays: A Deep Learning Approach In Lower Limb CT-Scans. Med. Phys. 48:published online, 2021.
  - *N*=2. Lower limb DRRs.
  - Based on Henzler et al. (see above).

GT

CNN

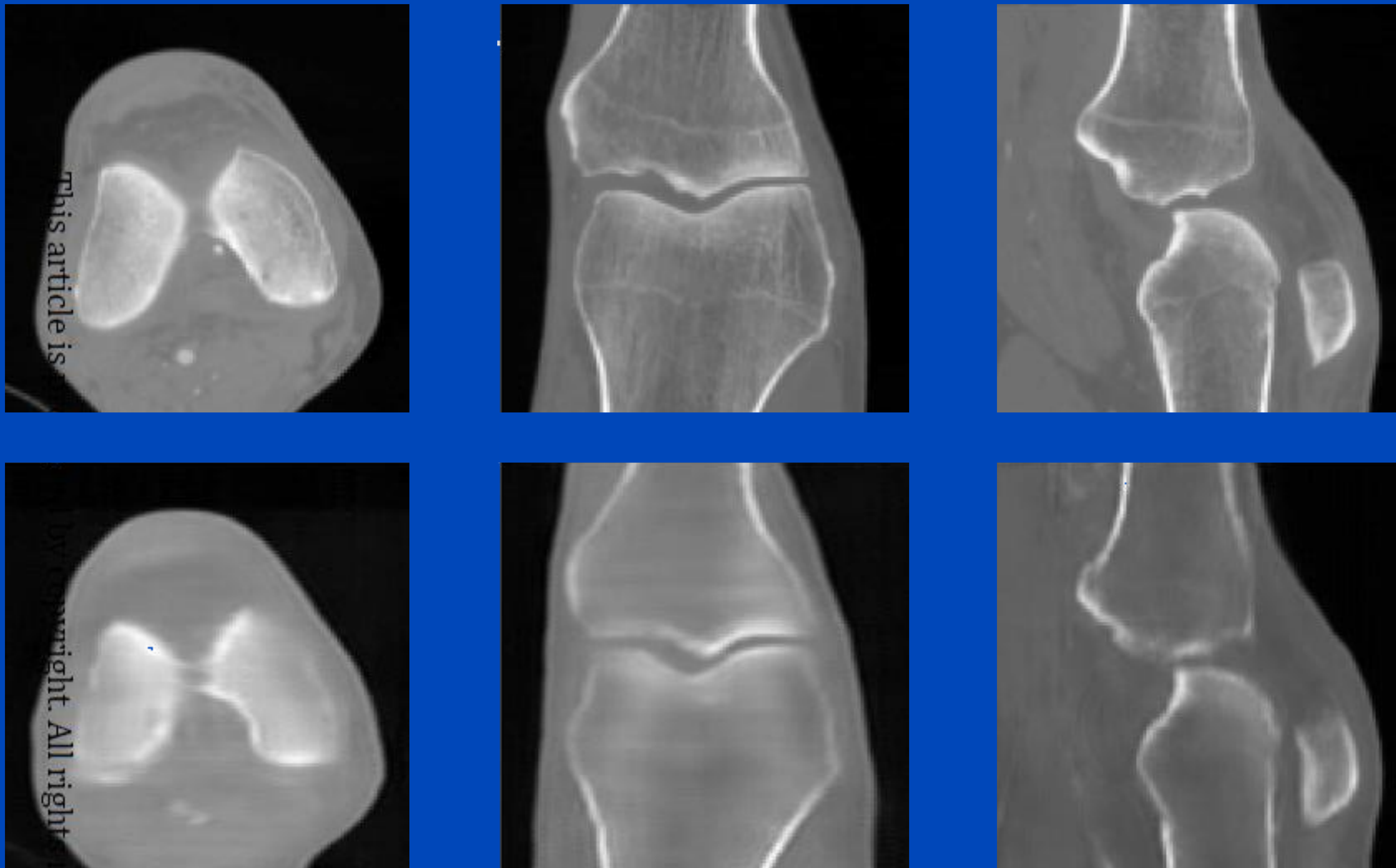

Almeida, Astudillo, and Vandermeulen. 3D Image Volumes From 2D Digitally Reconstructed X-Rays: A Deep Learning Approach In Lower Limb CT-Scans. Med. Phys. 48:published online, 2021.

Patient Risk-Minimizing Tube Current Modulation

1. Coarse reconstruction from two scout views

– E.g. X. Ying, et al. X2CT-GAN: Reconstructing CT from biplanar x-rays with generative adversarial networks. CVPR 2019.

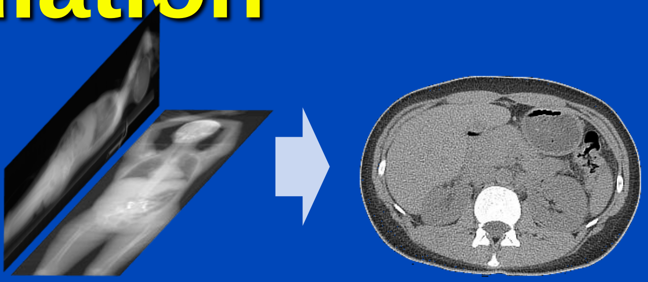

2. Segmentation of radiation-sensitive organs

– E.g. S. Chen, M. Kachelrieß et al., Automatic multi-organ segmentation in dual-energy CT (DECT) with dedicated 3D fully convolutional DECT networks. Med. Phys. 2019.

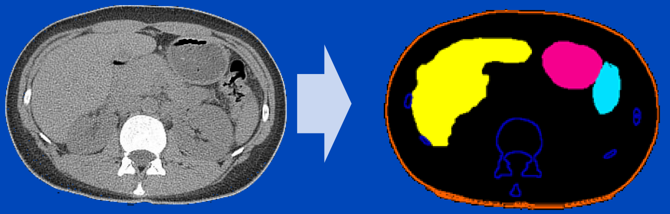

3. Calculation of the effective dose per view using the deep dose estimation (DDE)

– J. Maier, E. Eulig, S. Dorn, S. Sawall and M. Kachelrieß. Real-time patient-specific CT dose estimation using a deep convolutional neural network. IEEE Medical Imaging Conference Record, M-03-178: 3 pages, Nov. 2018.

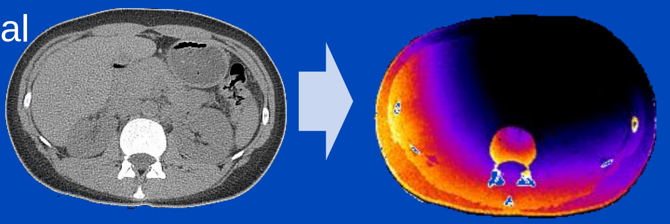

4. Determination of the tube current modulation curve that minimizes the radiation risk

– L. Klein, C. Liu, J. Steidel, L. Enzmann, M. Knaup, S. Sawall, A. Maier, M. Lell, J. Maier, and M. Kachelrieß. Patient-specific radiation risk-based tube current modulation for diagnostic CT. Med. Phys. 49: in press, 2022.

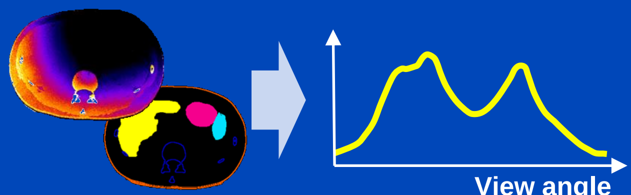

L. Klein, C. Liu, J. Steidel, L. Enzmann, M. Knaup, S. Sawall, A. Maier, M. Lell, J. Maier, and M. Kachelrieß. Patient-specific radiation risk-based tube current modulation for diagnostic CT. Med. Phys. 49: in press, 2022.

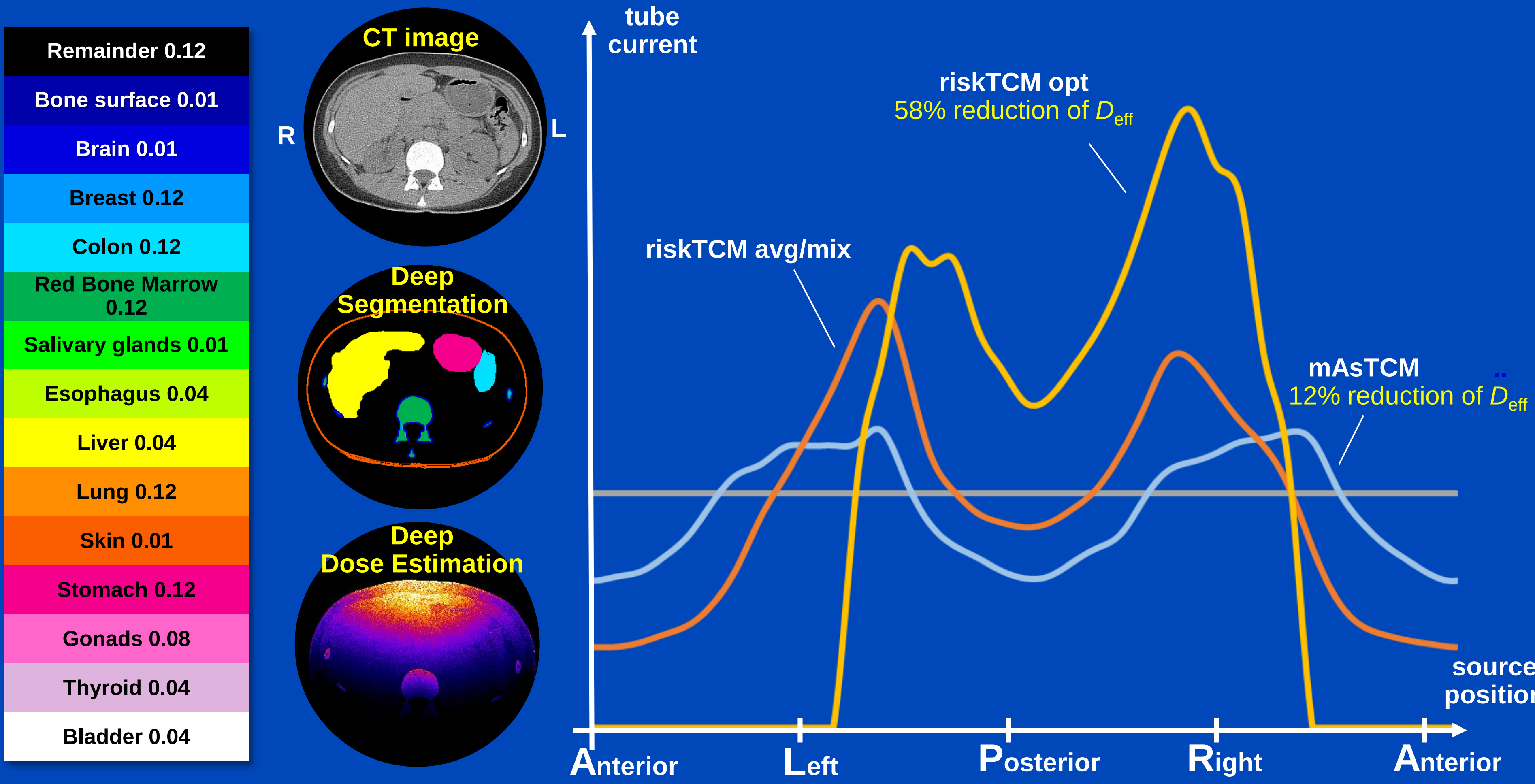

L. Klein, C. Liu, J. Steidel, L. Enzmann, M. Knaup, S. Sawall, A. Maier, M. Lell, J. Maier, and M. Kachelrieß.
Patient-specific radiation risk-based tube current modulation for diagnostic CT. Med. Phys. 49: in press, 2022.

Patient 03 - Neck

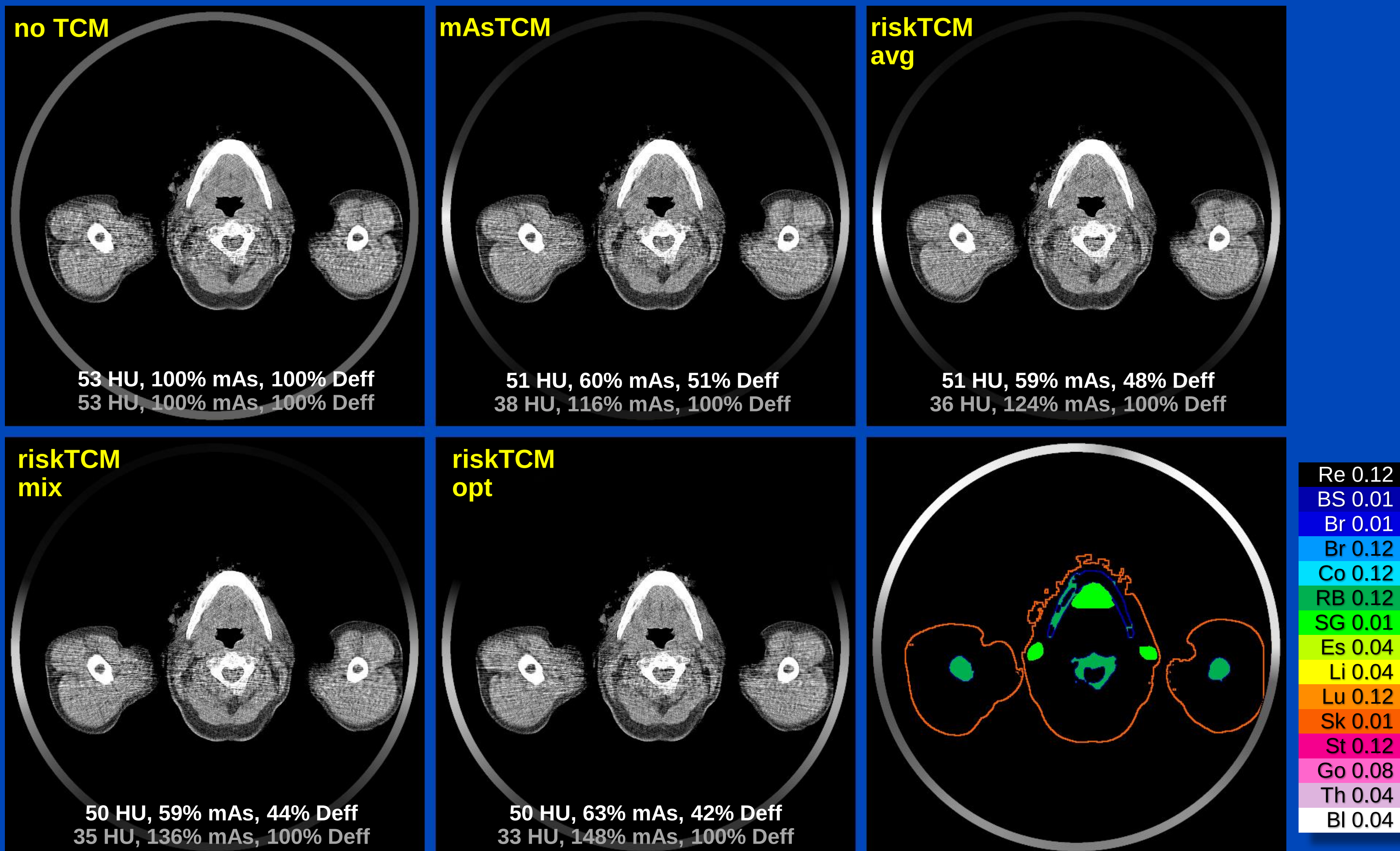

C = 25 HU, W = 400 HU

L. Klein, C. Liu, J. Steidel, L. Enzmann, M. Knaup, S. Sawall, A. Maier, M. Lell, J. Maier, and M. Kachelrieß. Patient-specific radiation risk-based tube current modulation for diagnostic CT. Med. Phys. 49: in press, 2022.

Patient 03 - Pelvis

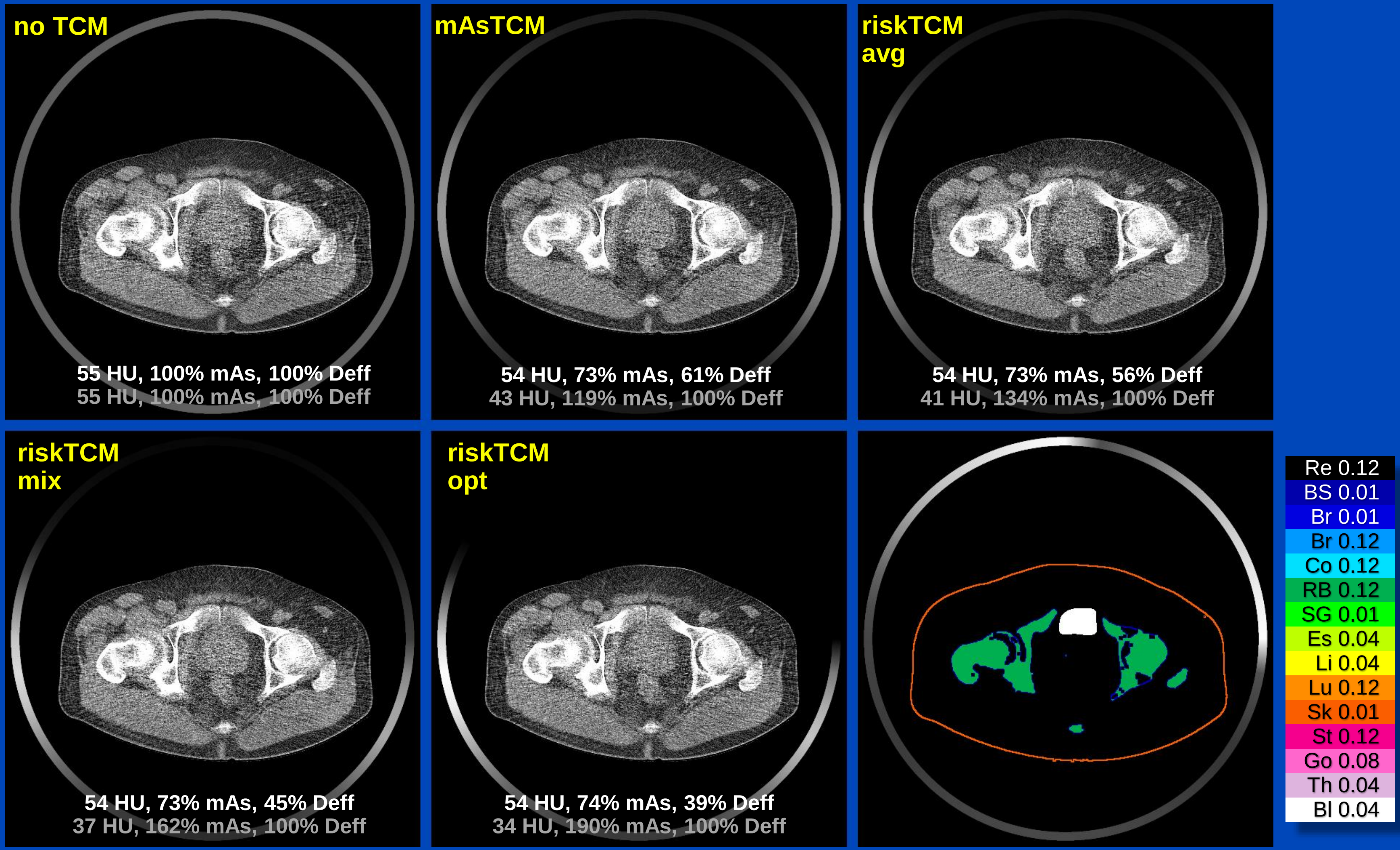

C = 25 HU, *W* = 400 HU

L. Klein, C. Liu, J. Steidel, L. Enzmann, M. Knaup, S. Sawall, A. Maier, M. Lell, J. Maier, and M. Kachelrieß.
Patient-specific radiation risk-based tube current modulation for diagnostic CT. Med. Phys. 49: in press, 2022.

Patient 04 - Abdomen

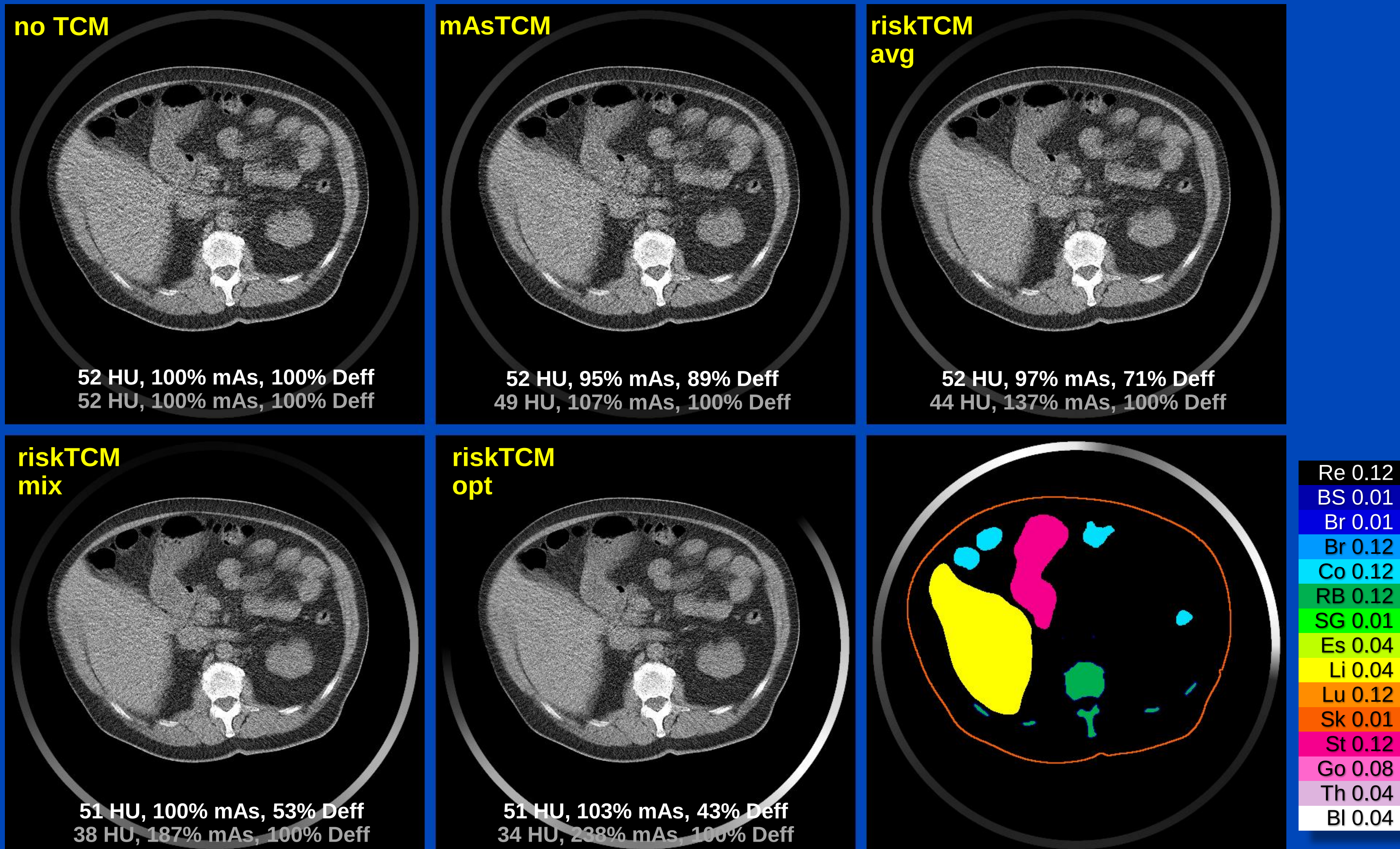

C = 25 HU, *W* = 400 HU

L. Klein, C. Liu, J. Steidel, L. Enzmann, M. Knaup, S. Sawall, A. Maier, M. Lell, J. Maier, and M. Kachelrieß.
Patient-specific radiation risk-based tube current modulation for diagnostic CT. Med. Phys. 49: in press, 2022.

Conclusions on RiskTCM

- Risk-specific TCM minimizes the patient risk.
- With D_{eff} as a risk model riskTCM can reduce risk by up to 50% and more, compared with the gold standard mAsTCM.
- Other risk models, in particular age-, weight- and sex-specific models, can be used with riskTCM as well.
- Note:
  - mAsTCM = good for the x-ray tube
  - riskTCM = good for the patient
  - detector flux equalizing TCM = good for the detector

riskTCM vs. Breast-Specific TCM

- osTCM mimics X-Care (Siemens Healthineers)
- Reduces the tube current to 25% for the anterior 120°
- Higher tube current for the remaining 240°

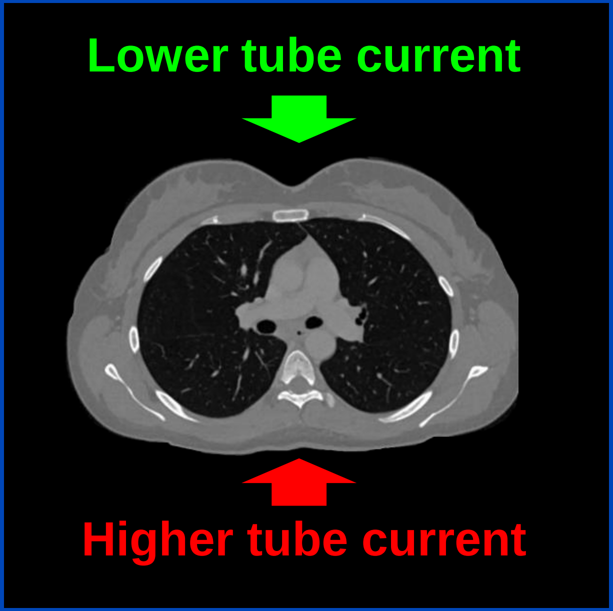

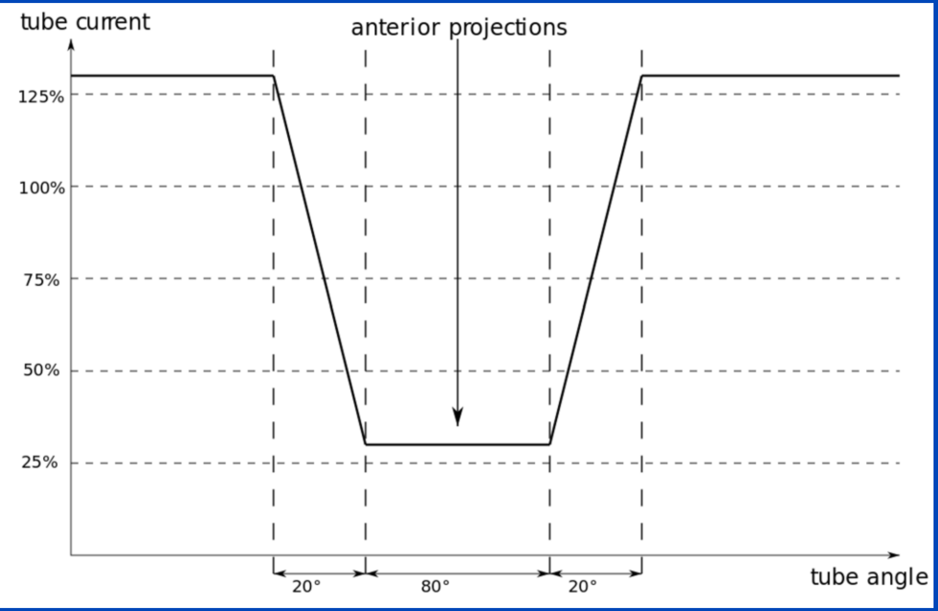

D. Ketelsen et al. Automated computed tomography dosesaving algorithm to protect radiosensitive tissues: estimation of radiation exposure and image quality considerations. Invest Radiol, 47(2):148–52, 2012

Results

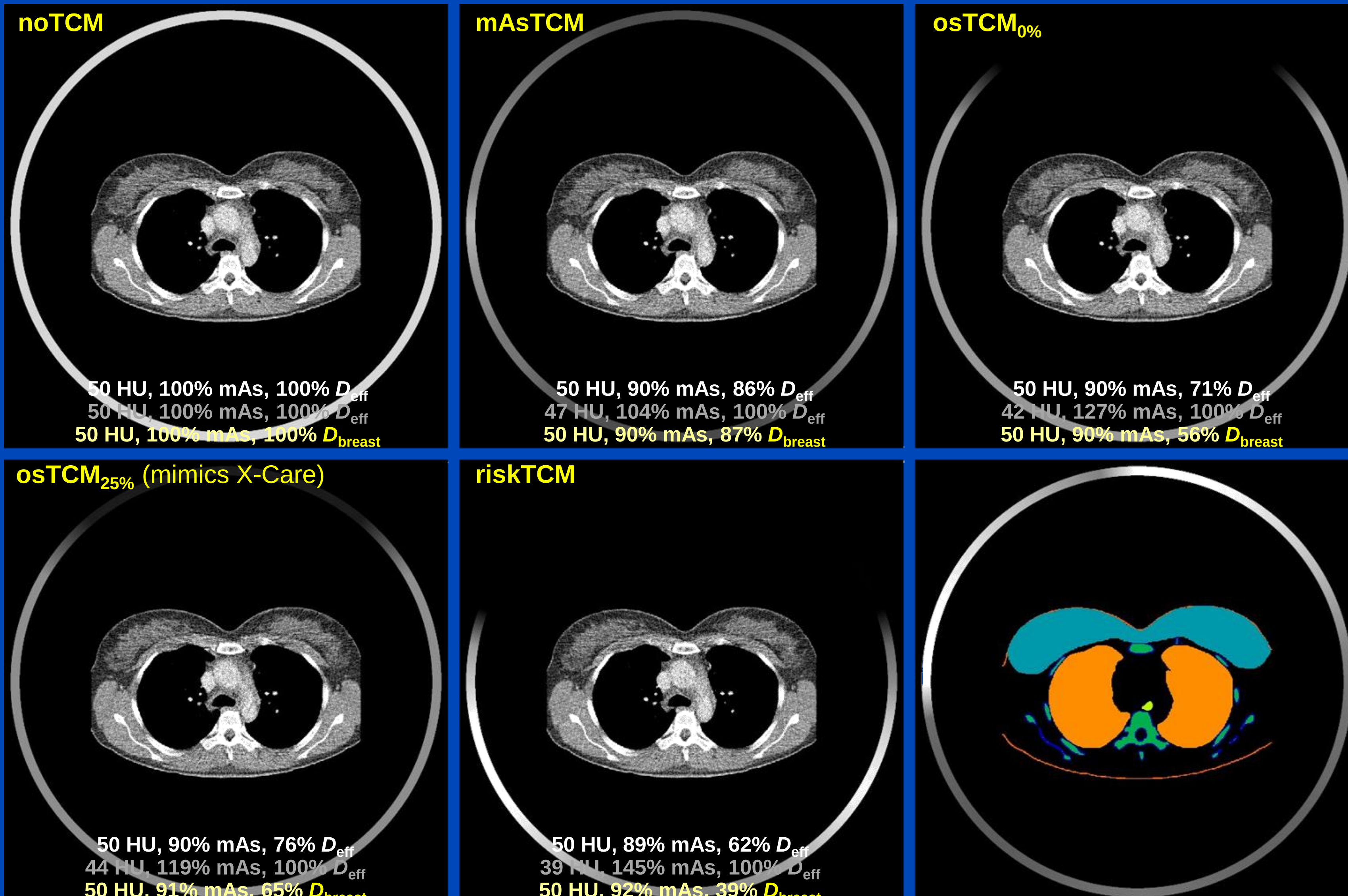

Data courtesy of Prof. Lell, Nürnberg. C = 25 HU, W = 400 HU

Conclusions on RiskTCM

- Risk-specific TCM minimizes the patient risk.
- With D_{eff} as a risk model riskTCM can reduce risk by up to 50% and more, compared with the gold standard mAsTCM.
- Other risk models, in particular age-, weight- and sex-specific models, can be used with riskTCM as well.
- Note:
  - mAsTCM = good for the x-ray tube
  - riskTCM = good for the patient
  - detector flux equalizing TCM = good for the detector
- **Compared with breast-specific TCM the riskTCM approach is 25% lower in dose.**

Deep Cardiac Motion Compensation

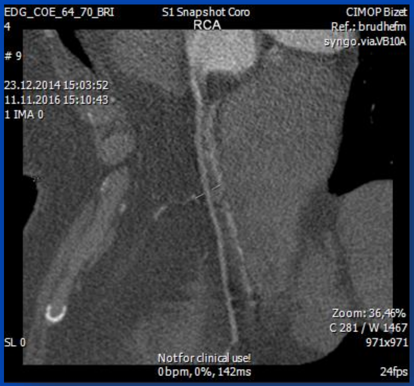

???

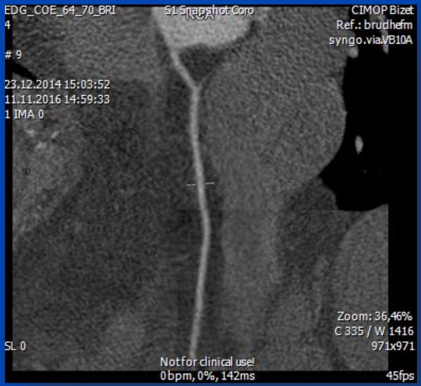

Motivation

- **Cardiac CT imaging is routinely used for the diagnosis of cardiovascular diseases, especially those related to coronary arteries.**
- **Imaging of coronary arteries places high demands on the spatial and temporal resolution of the CT reconstruction.**
- **Motion artifacts and image noise may impair the diagnostic value of the CT examination.**

CTCA image of the right coronary artery[1]

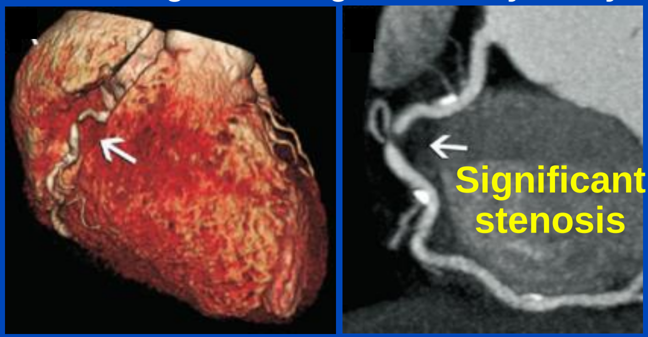

CTCA image of the left coronary artery[2]

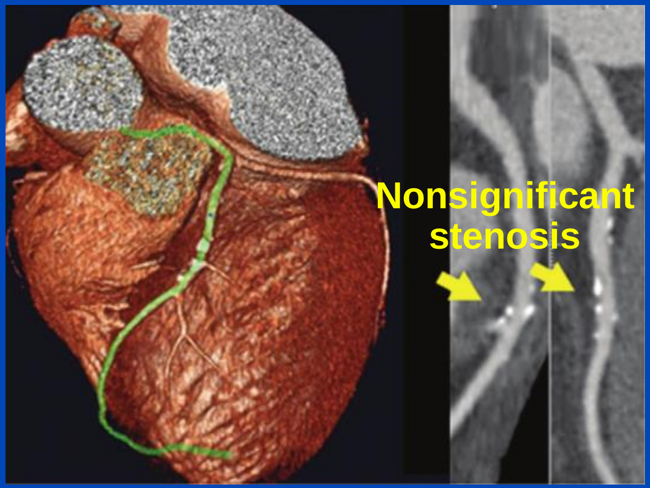

[1] W. B. Meijboom et al., “64-Slice Computed Tomography Coronary Angiography in Patients With High, Intermediate, or Low Pretest Probability of Significant Coronary Artery Disease”, J. Am. Coll. Cardiol. 50 (15): 1469–1475 (2007).
[2] R. Leta et al., “Ruling Out Coronary Artery Disease with Noninvasive Coronary Multidetector CT Angiography before Noncoronary Cardiovascular Surgery”, Heart 258 (2) (2011).

dkfz.

Motivation

C = 0 HU, *W* = 1200 HU

Motion artifacts

High noise levels

Table 3: Reason for FFR_{CT} Rejection in the ADVANCE Registry and Clinical Cohort *

Reason for Rejection	FFR_{CT} Rejected* ADVANCE Registry (n = 80)	Clinical Cohort (n = 892)
Inadequate image quality†		
Blooming	4 (5.0)	29 (3.0)
Clipped structure	4 (5.0)	39 (4.3)
Motion artifacts	63 (78.0)	729 (81.4)
Image noise	2 (2.5)	198 (22.1)
Inappropriate submission		
Stent or previous coronary artery bypass graft present	5 (6.2)	116 (13.0)
Cardiac hardware present	2 (2.5)	29 (3.2)

The rejection rate was 892 of 10416 cases submitted

*** G. Pontone et al., "Determinants of Rejection Rate for Coronary CT Angiography Fractional Flow Reserve Analysis", *Radiology*, *292*(3), 597–605 (2019)**

Motivation

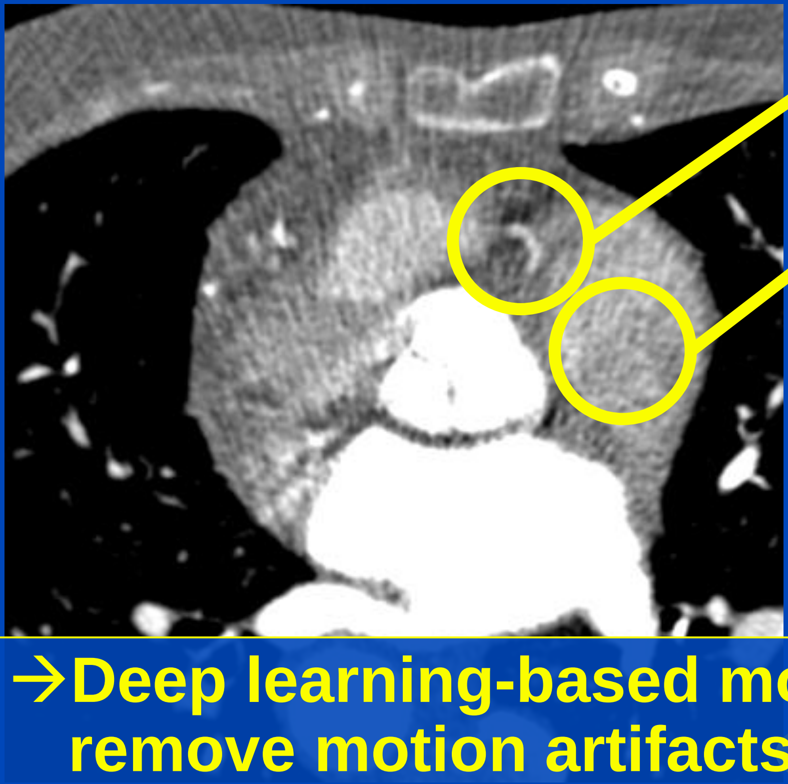

Motion artifacts

High noise levels

Table 3: Reason for FFR$_{CT}$ Rejection in the ADVANCE Registry and Clinical Cohort *

Reason for Rejection	FFR$_{CT}$ Rejected* ADVANCE Registry (n = 80)	FFR$_{CT}$ Rejected* Clinical Cohort (n = 892)
Inadequate image quality[†]		
Blooming	4 (5.0)	29 (3.0)
Clipped structure	4 (5.0)	39 (4.3)
Motion artifact	[illegible]	729 (81.4)
Image noise	2 (2.5)	198 (22.1)
Inappropriate submission		
Severe previous coronary artery bypass graft present	[illegible]	[illegible]
Cardiac hardware present	2 (2.5)	29 (3.2)

The rejection rate was 892 of 10 416 cases submitted

→Deep learning-based motion compensation to remove motion artifacts.

→Iterative reconstruction (Siemens ADMIRE) to reduce noise.

* G. Pontone et al., "Determinants of Rejection Rate for Coronary CT Angiography Fractional Flow Reserve Analysis", *Radiology*, *292*(3), 597–605 (2019)

dkfz.

Partial Angle-Based Motion Compensation (PAMoCo)

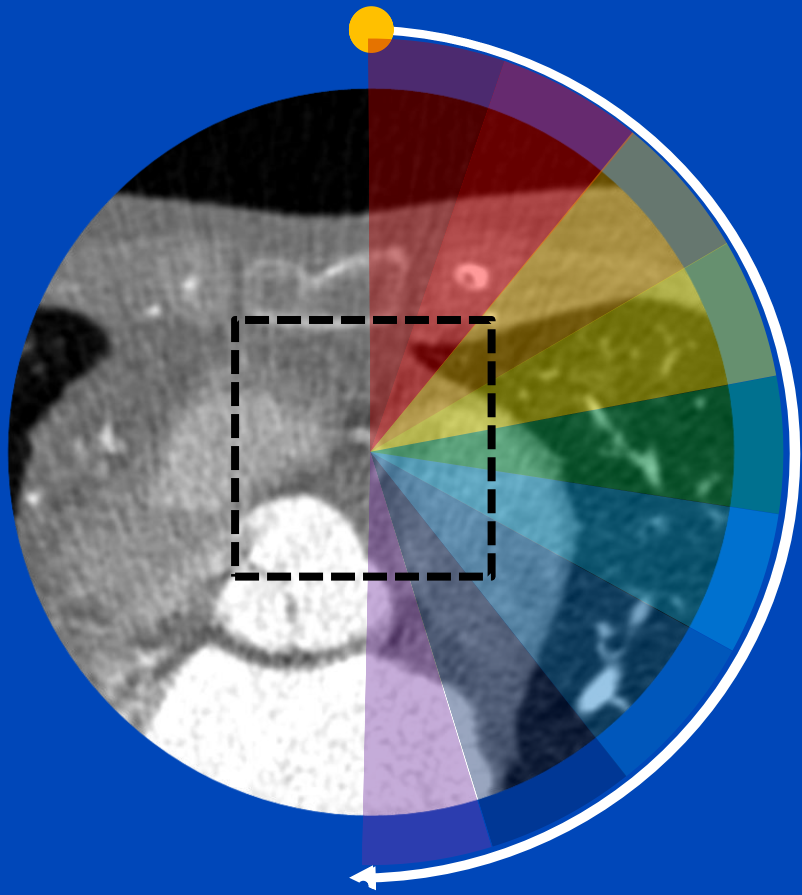

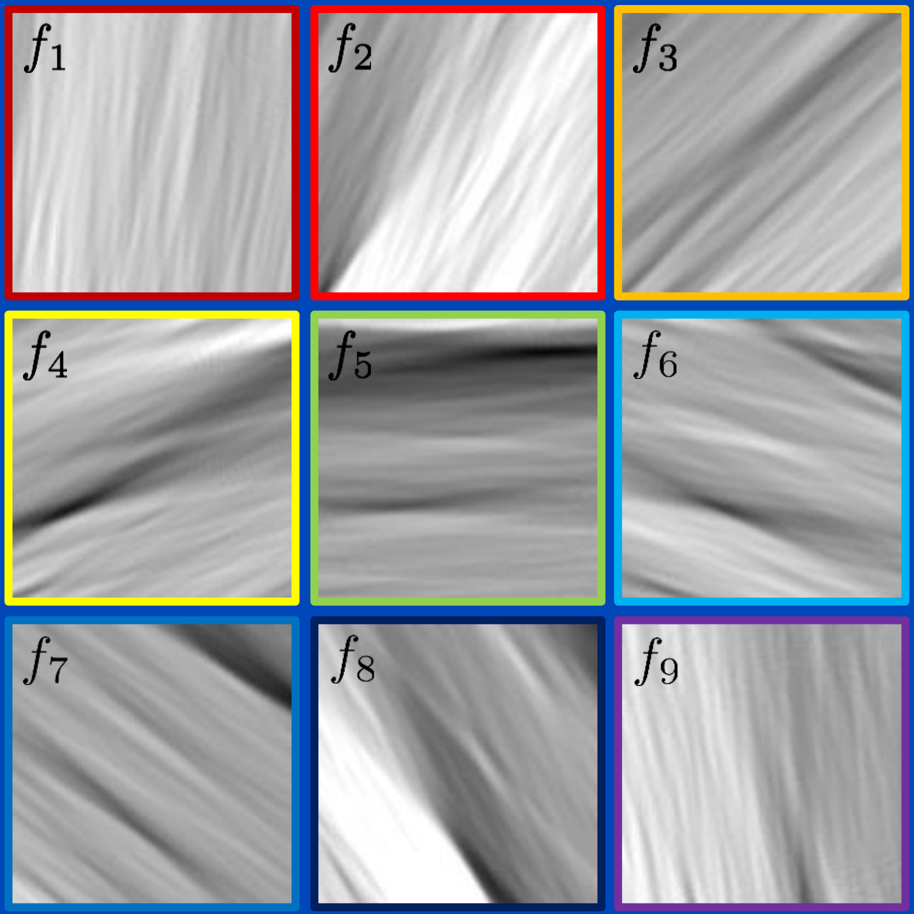

Animated rotation time = 100 × real rotation time

dkfz.

Partial Angle-Based Motion Compensation (PAMoCo)

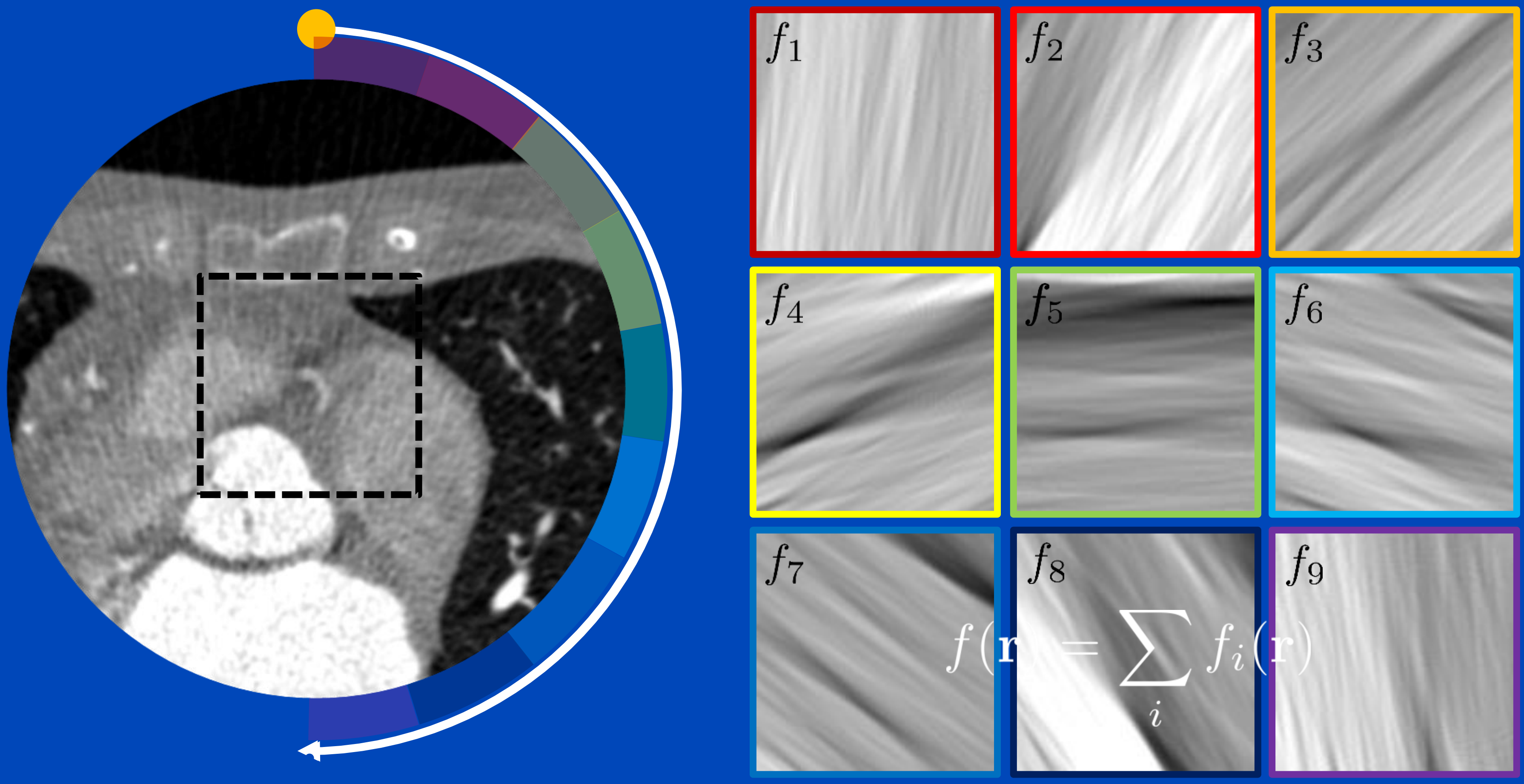

Partial Angle-Based Motion Compensation (PAMoCo)

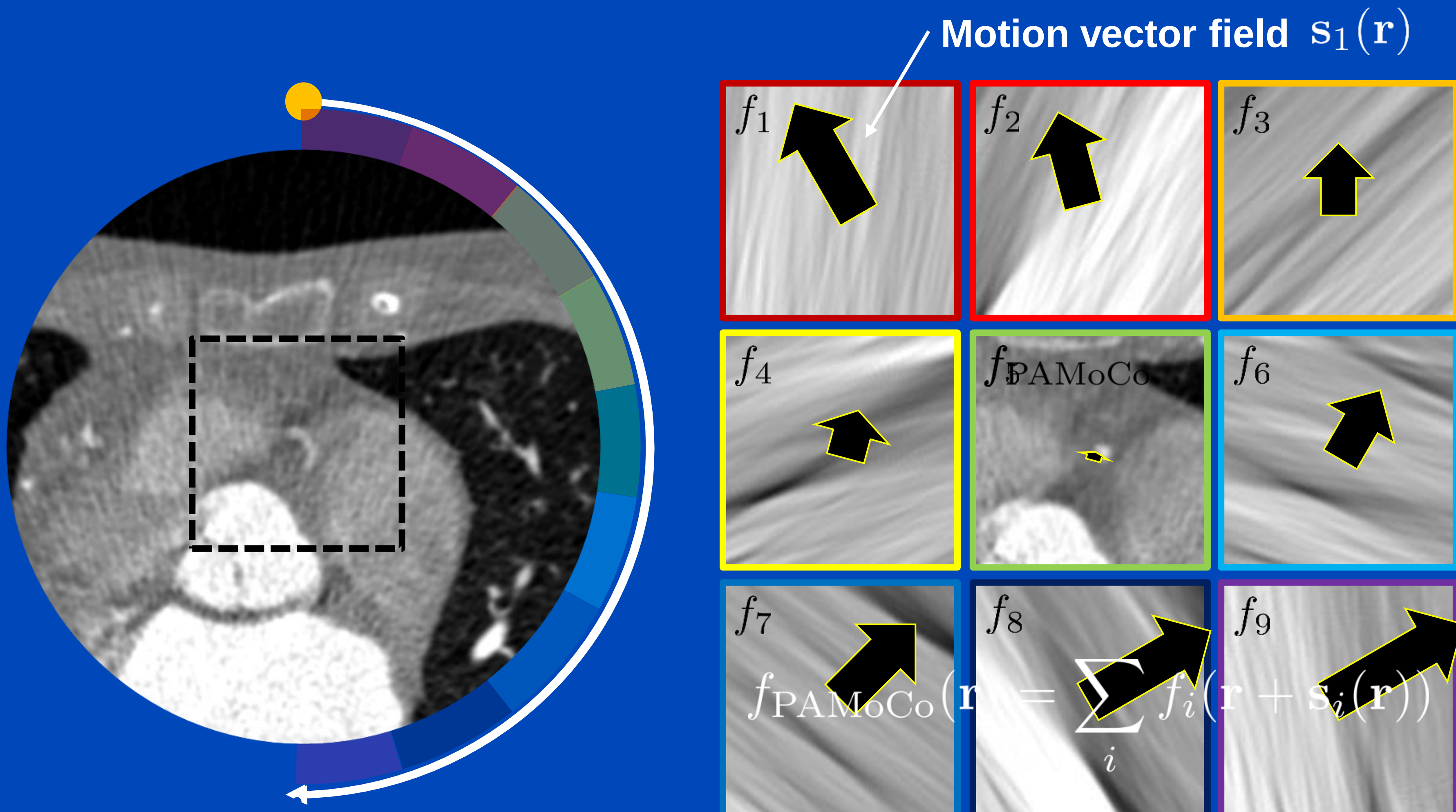

Apply motion vector fields (MVFs) to partial angle reconstructions

Partial Angle-Based Motion Compensation (PAMoCo)

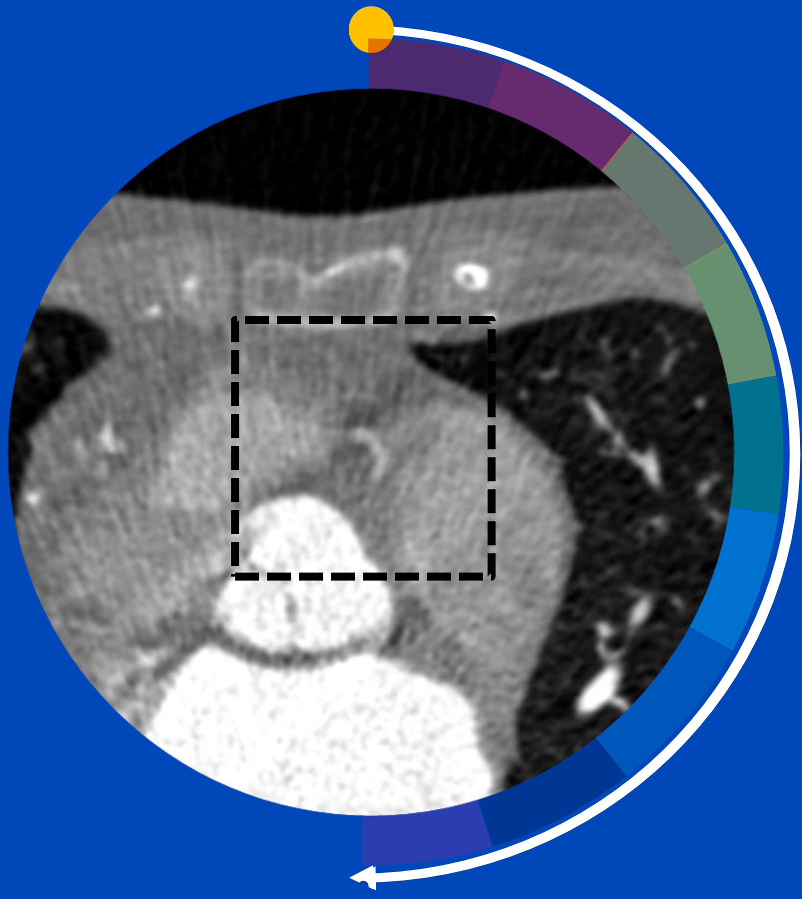

Prior work:

[1] S. Kim et al., "Cardiac motion correction based on partial angle reconstructed images in x-ray CT", Med. Phys. 42 (5): 2560–2571 (2015).

[2] J. Hahn et al., "Motion compensation in the region of the coronary arteries based on partial angle reconstructions from short-scan CT data", Med. Phys. 44 (11): 5795–5813 (2017).

[3] S. Kim et al., "Cardiac motion correction for helical CT scan with an ordinary pitch", IEEE TMI 37 (7): 1587–1596 (2018).

→ Limitation: Challenging / time-consuming optimization

Deep Partial Angle-Based Motion Compensation (Deep PAMoCo)

PARs centered around coronary artery

Neural network to predict parameters of a motion model

Reinsertion of patch into initial reconstruction

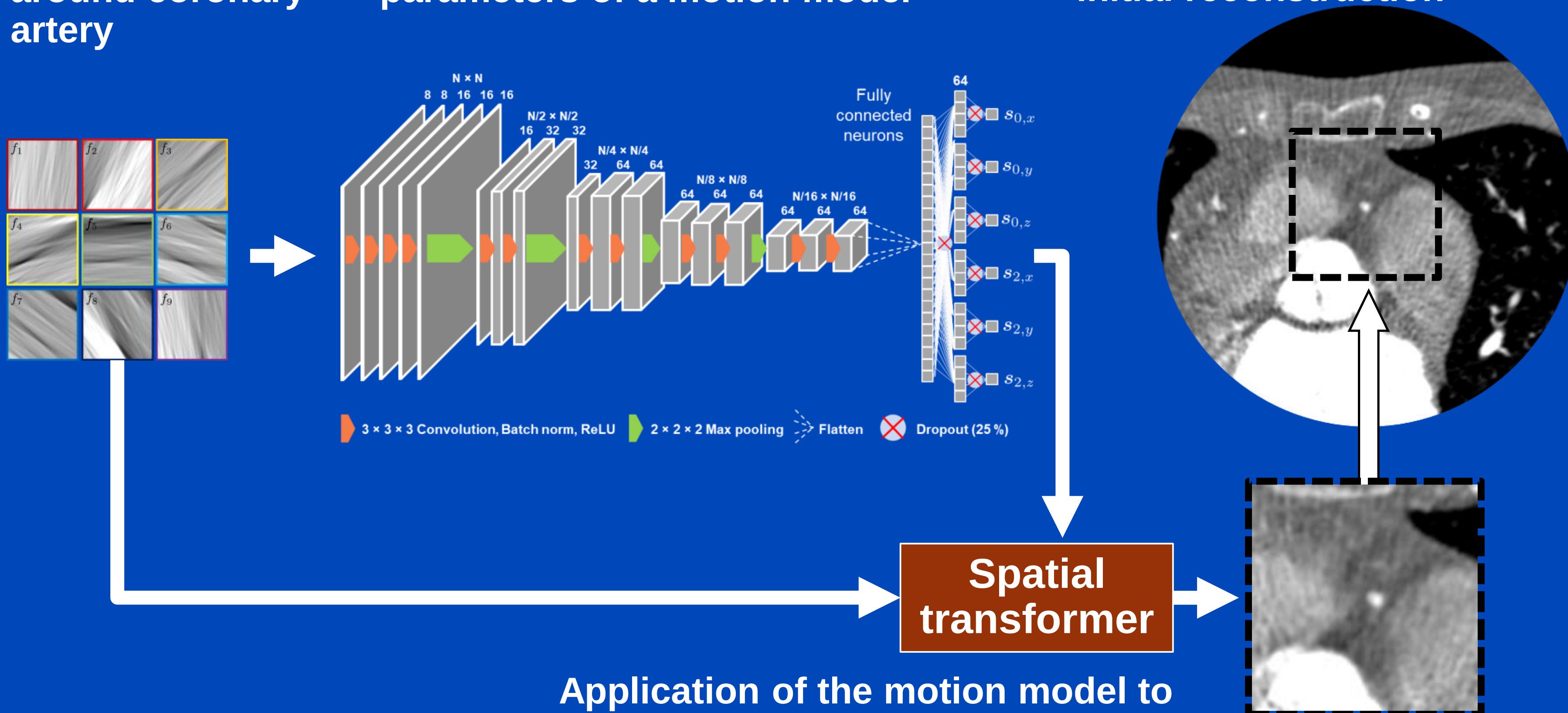

Application of the motion model to the PARs via a spatial transformer

Deep Partial Angle-Based Motion Compensation (Deep PAMoCo)

Motion model

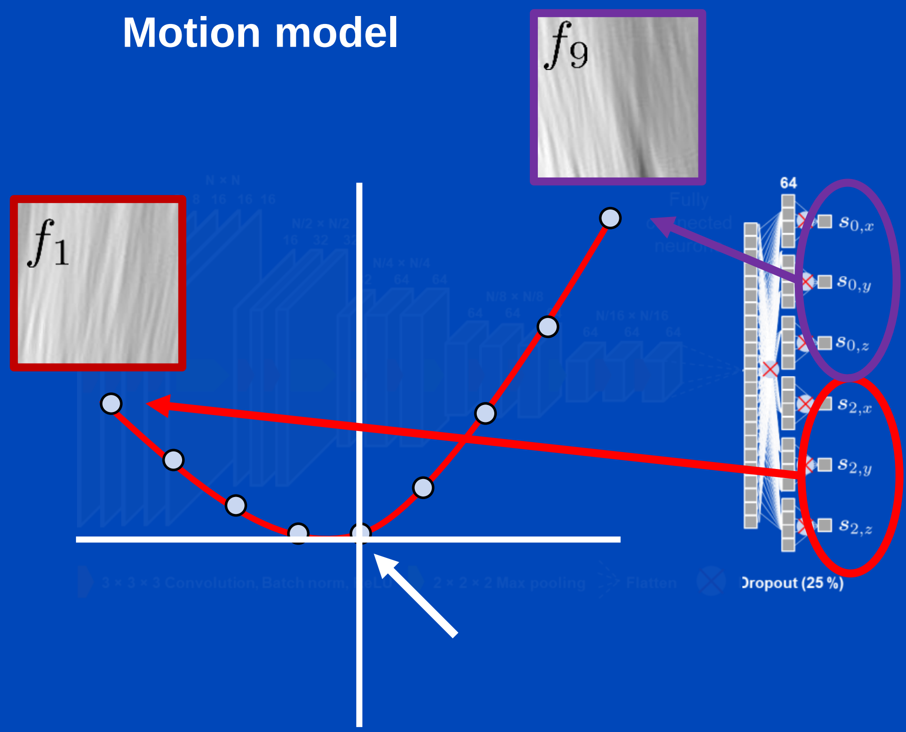

dkfz.

Training Data Generation

- Removal of coronary arteries from real CT reconstructions.
- Insertion of artificial coronary arteries with different shape, size, and contrast.
- Simulation of CT scans with coronary artery motion.

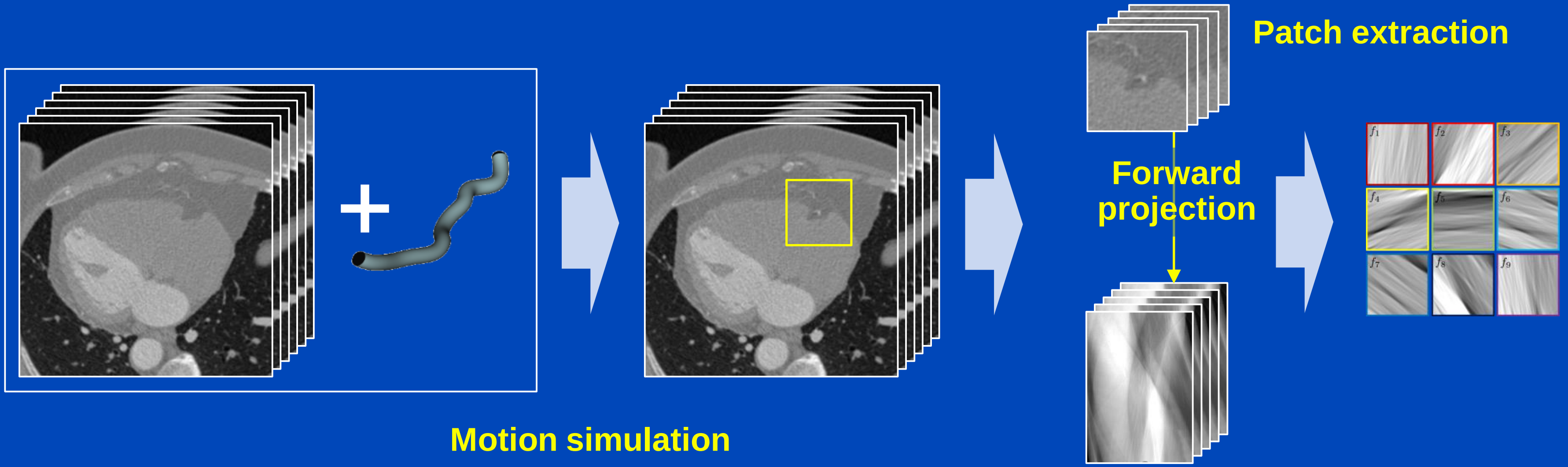

Results

Measurements, patient 1

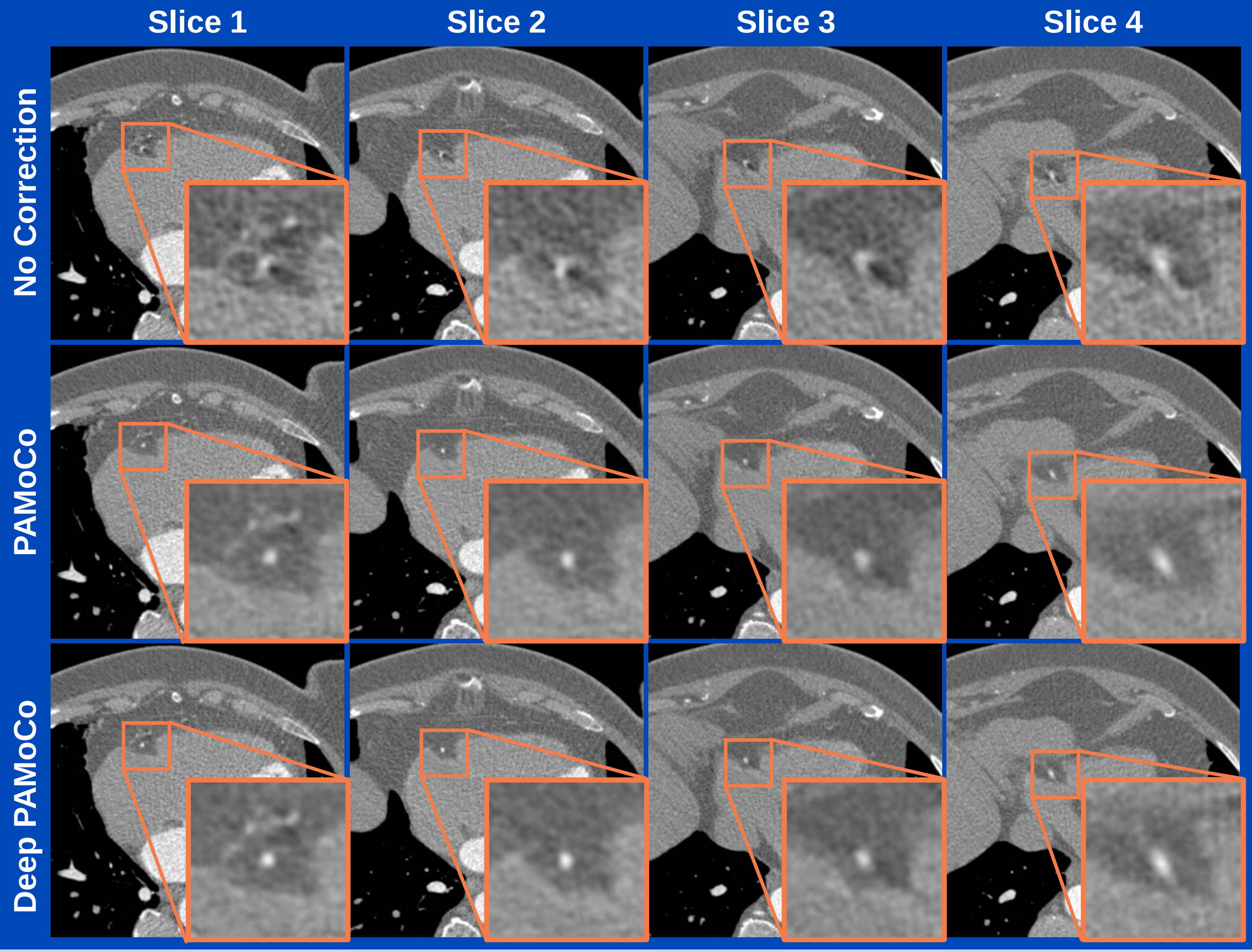

C = 1000 HU
W = 1000 HU

J. Maier, S. Lebedev, J. Erath, E. Eulig, S. Sawall, E. Fournié, K. Stierstorfer, M. Lell, and M. Kachelrieß. Deep learning-based coronary artery motion estimation and compensation for short-scan cardiac CT. Med. Phys. 48(7):3559-3571, July 2021.

Results

Measurements, patient 2

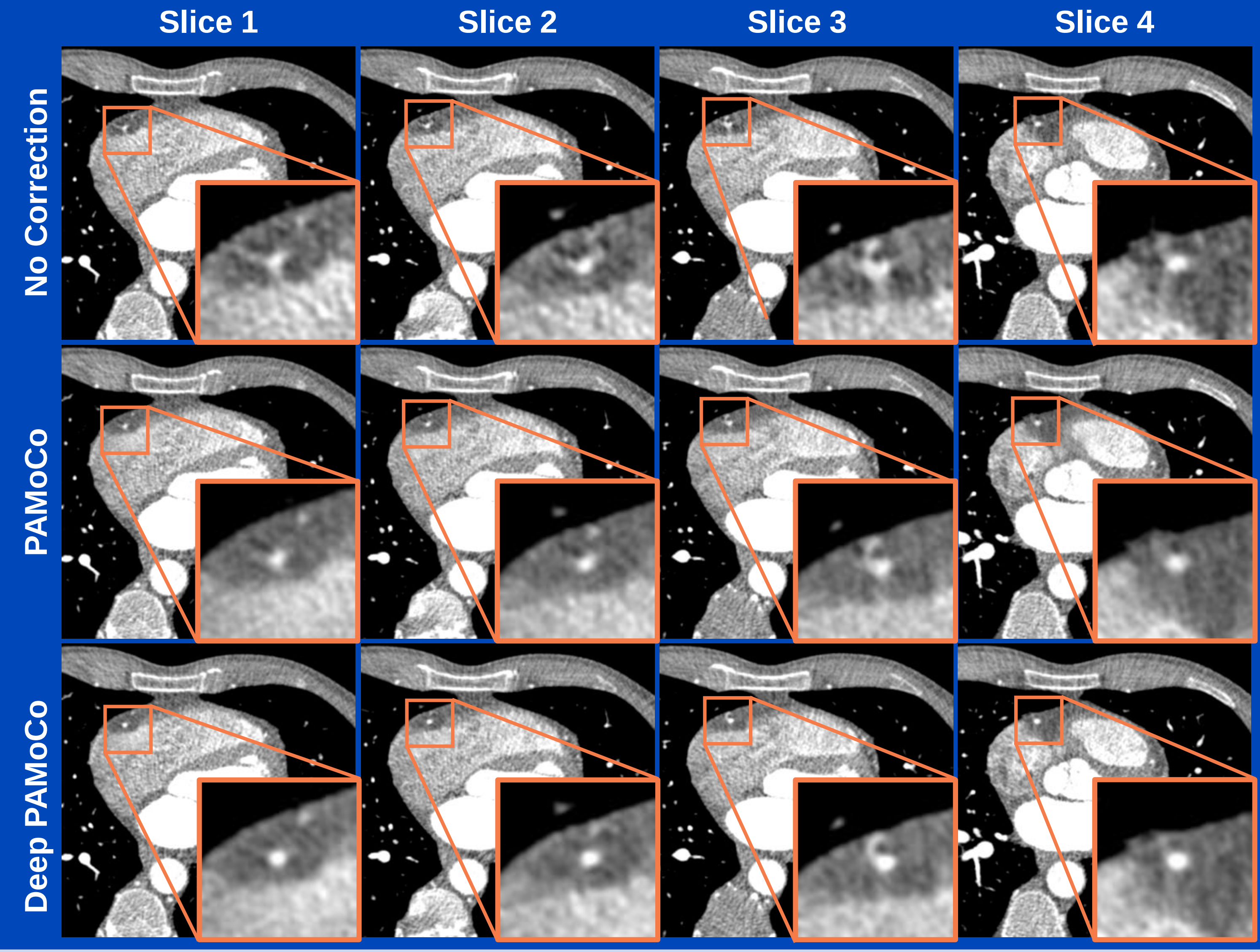

C = 1000 HU
W = 1000 HU

J. Maier, S. Lebedev, J. Erath, E. Eulig, S. Sawall, E. Fournié, K. Stierstorfer, M. Lell, and M. Kachelrieß. Deep learning-based coronary artery motion estimation and compensation for short-scan cardiac CT. Med. Phys. 48(7):3559-3571, July 2021.

Results

Measurements, patient 3

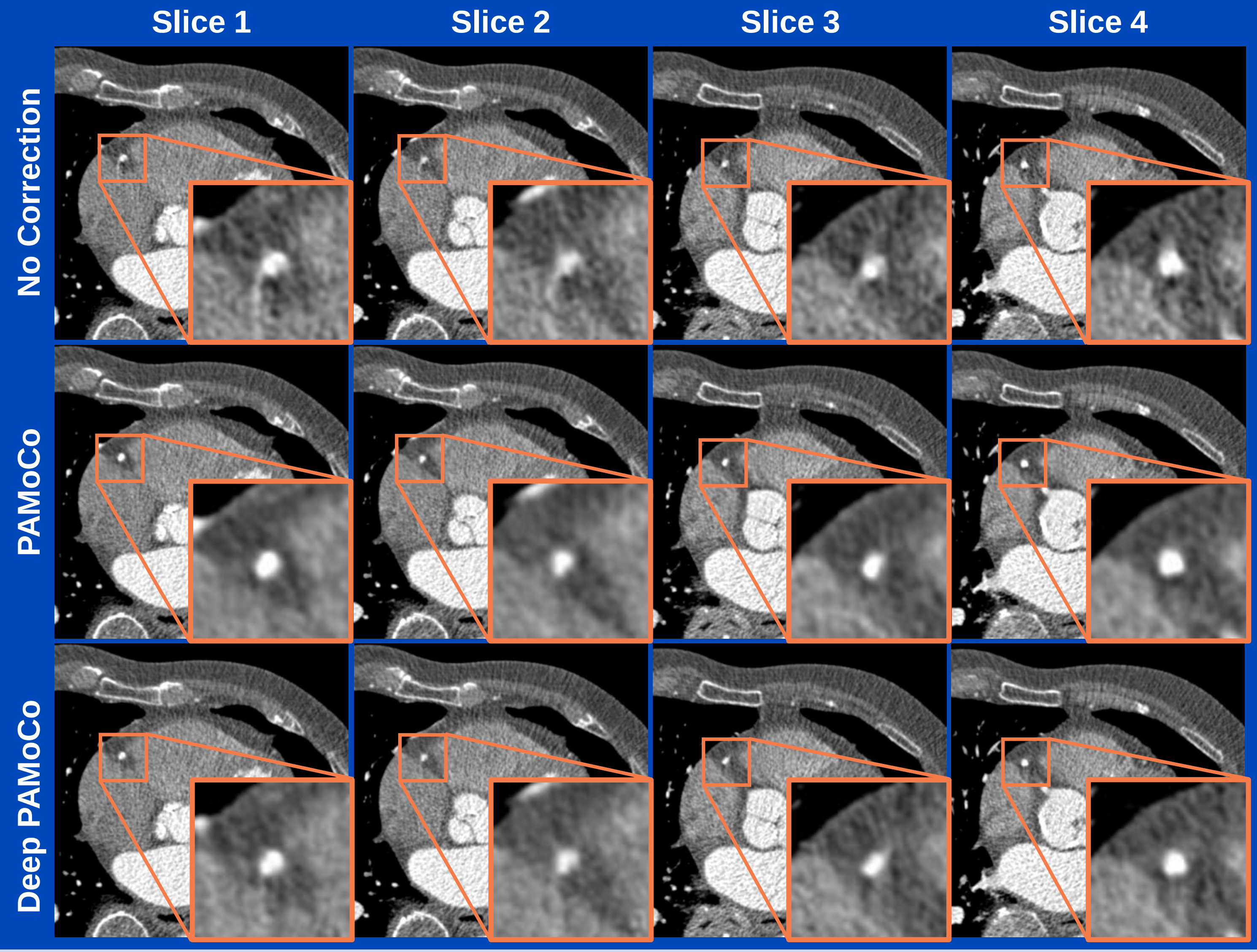

C = 1100 HU
W = 1000 HU

J. Maier, S. Lebedev, J. Erath, E. Eulig, S. Sawall, E. Fournié, K. Stierstorfer, M. Lell, and M. Kachelrieß. Deep learning-based coronary artery motion estimation and compensation for short-scan cardiac CT. Med. Phys. 48(7):3559-3571, July 2021.

Patient 5

Original

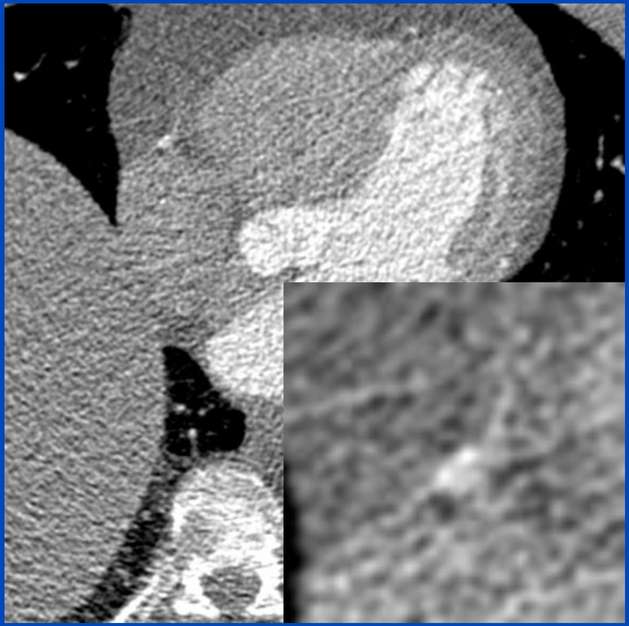

Deep PAMoCo

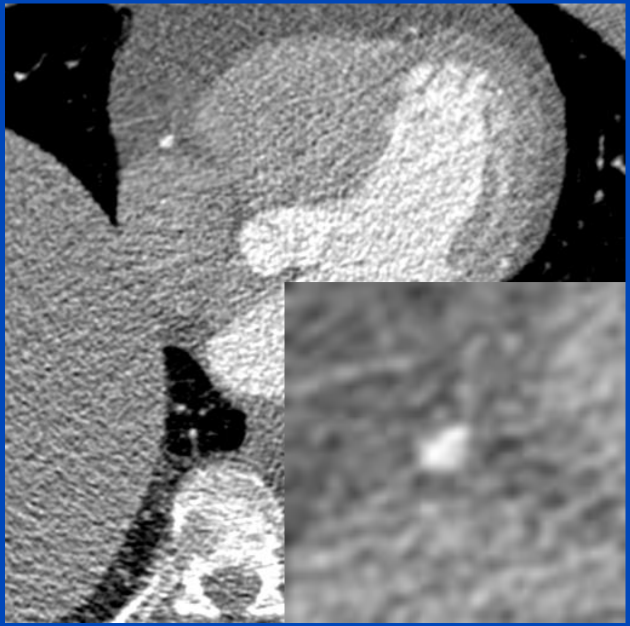

C = 0 HU, W = 1200 HU

J. Maier, S. Lebedev, J. Erath, E. Eulig, S. Sawall, E. Fournié, K. Stierstorfer, M. Lell, and M. Kachelrieß. Deep learning-based coronary artery motion estimation and compensation for short-scan cardiac CT. Med. Phys. 48(7):3559-3571, July 2021.

Patient 6

Original

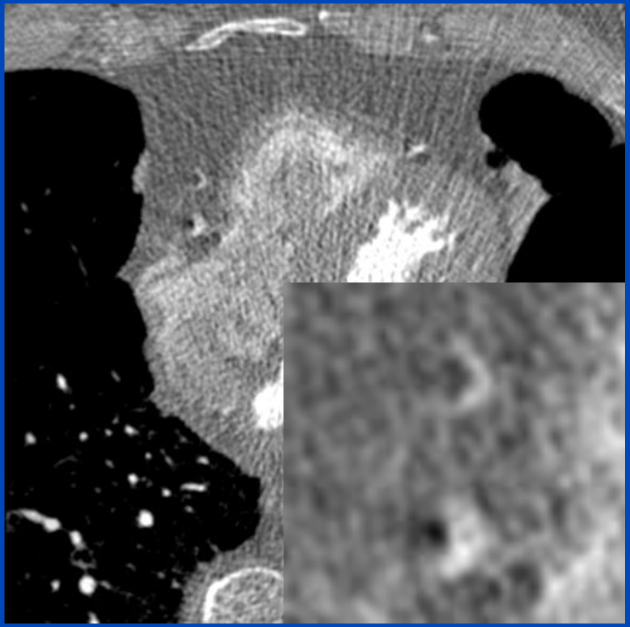

Deep PAMoCo

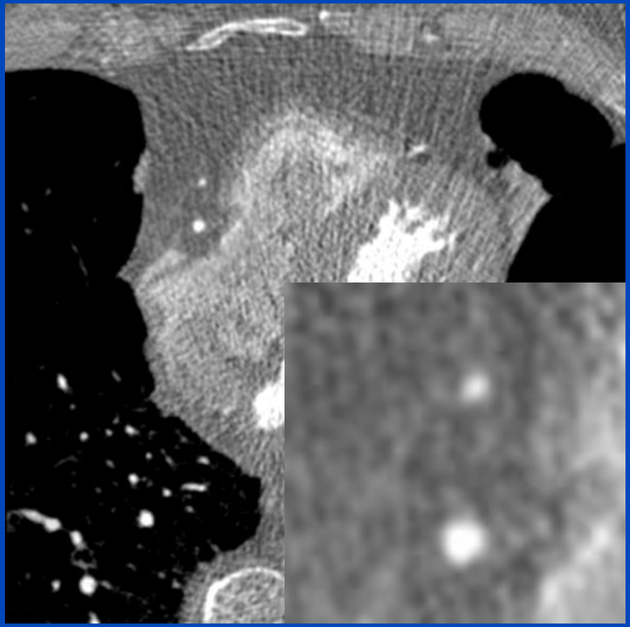

C = 0 HU, W = 1400 HU

Patient 7

Original

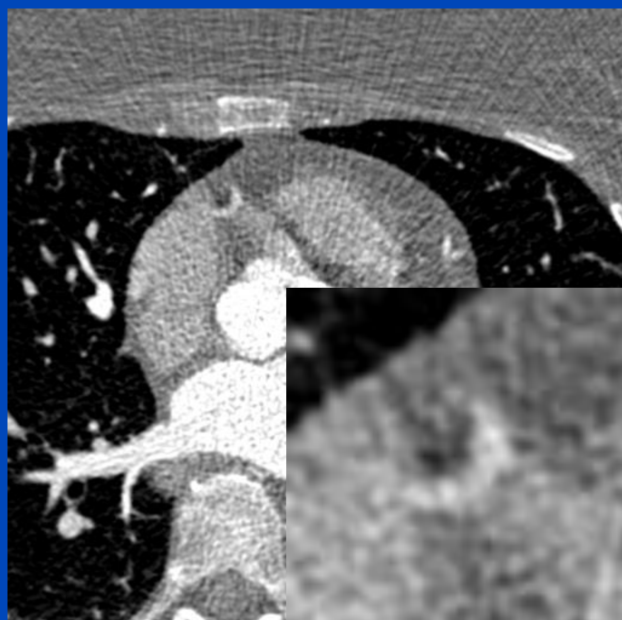

Deep PAMoCo

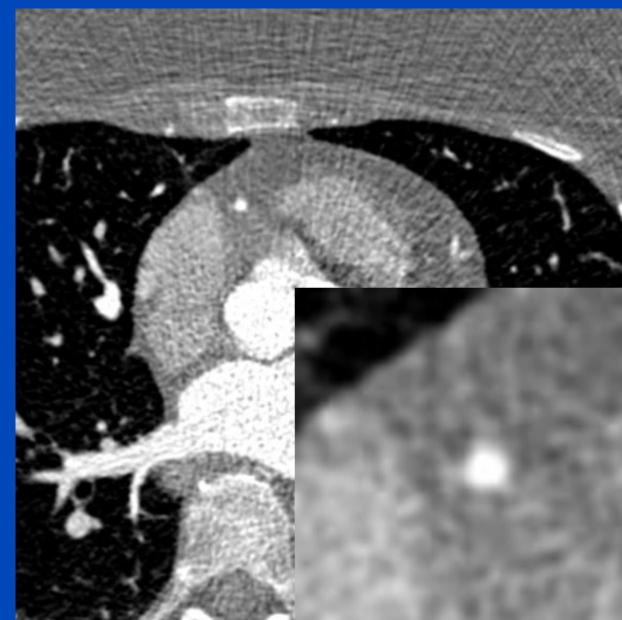

***C* = 0 HU, *W* = 1600 HU**

J. Maier, S. Lebedev, J. Erath, E. Eulig, S. Sawall, E. Fournié, K. Stierstorfer, M. Lell, and M. Kachelrieß. Deep learning-based coronary artery motion estimation and compensation for short-scan cardiac CT. Med. Phys. 48(7):3559-3571, July 2021.

Patient 8

Original

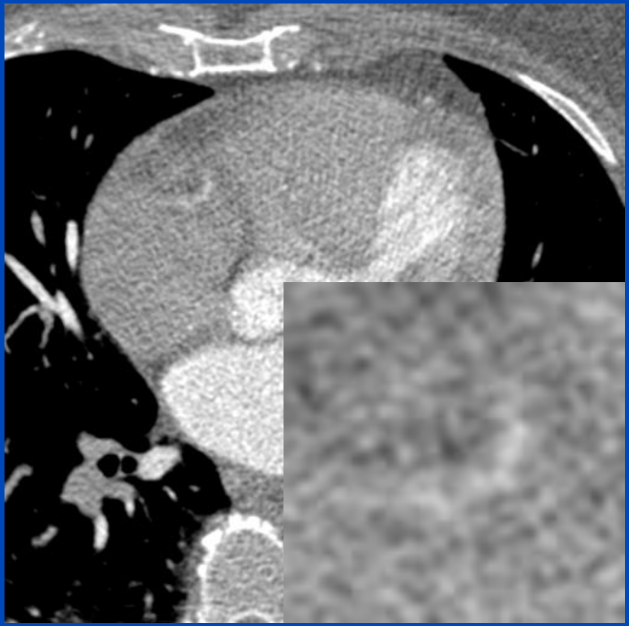

Deep PAMoCo

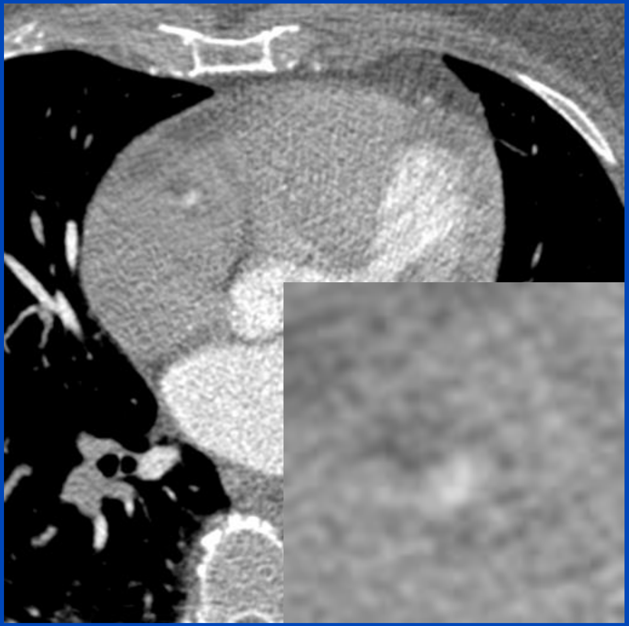

C = 0 HU, *W* = 1000 HU

J. Maier, S. Lebedev, J. Erath, E. Eulig, S. Sawall, E. Fournié, K. Stierstorfer, M. Lell, and M. Kachelrieß. Deep learning-based coronary artery motion estimation and compensation for short-scan cardiac CT. Med. Phys. 48(7):3559-3571, July 2021.

Results

Measurements at a Siemens Somatom AS, patient 1

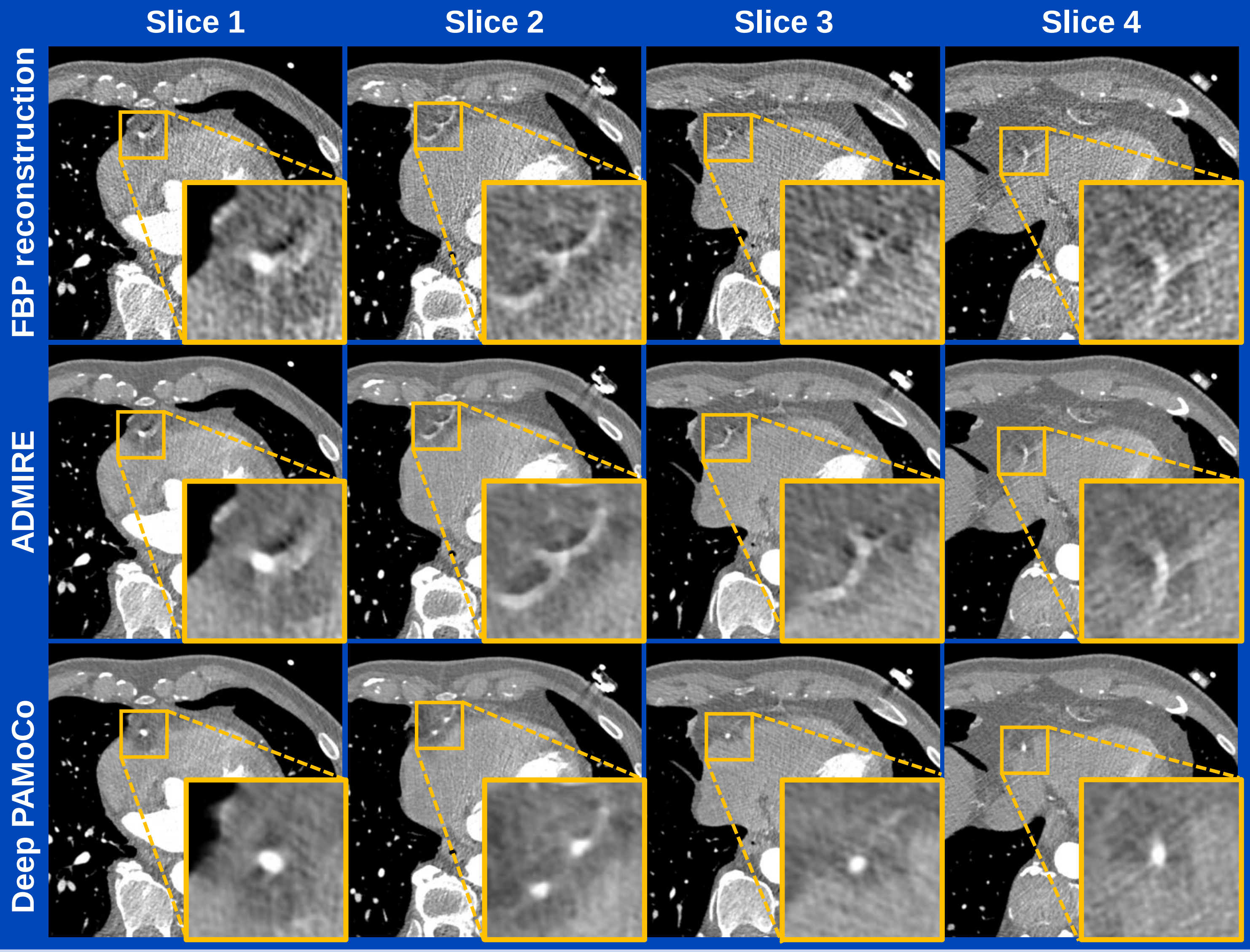

$C = 0$ HU, $W = 1200$ HU

Results

Measurements at a Siemens Somatom AS, patient 2

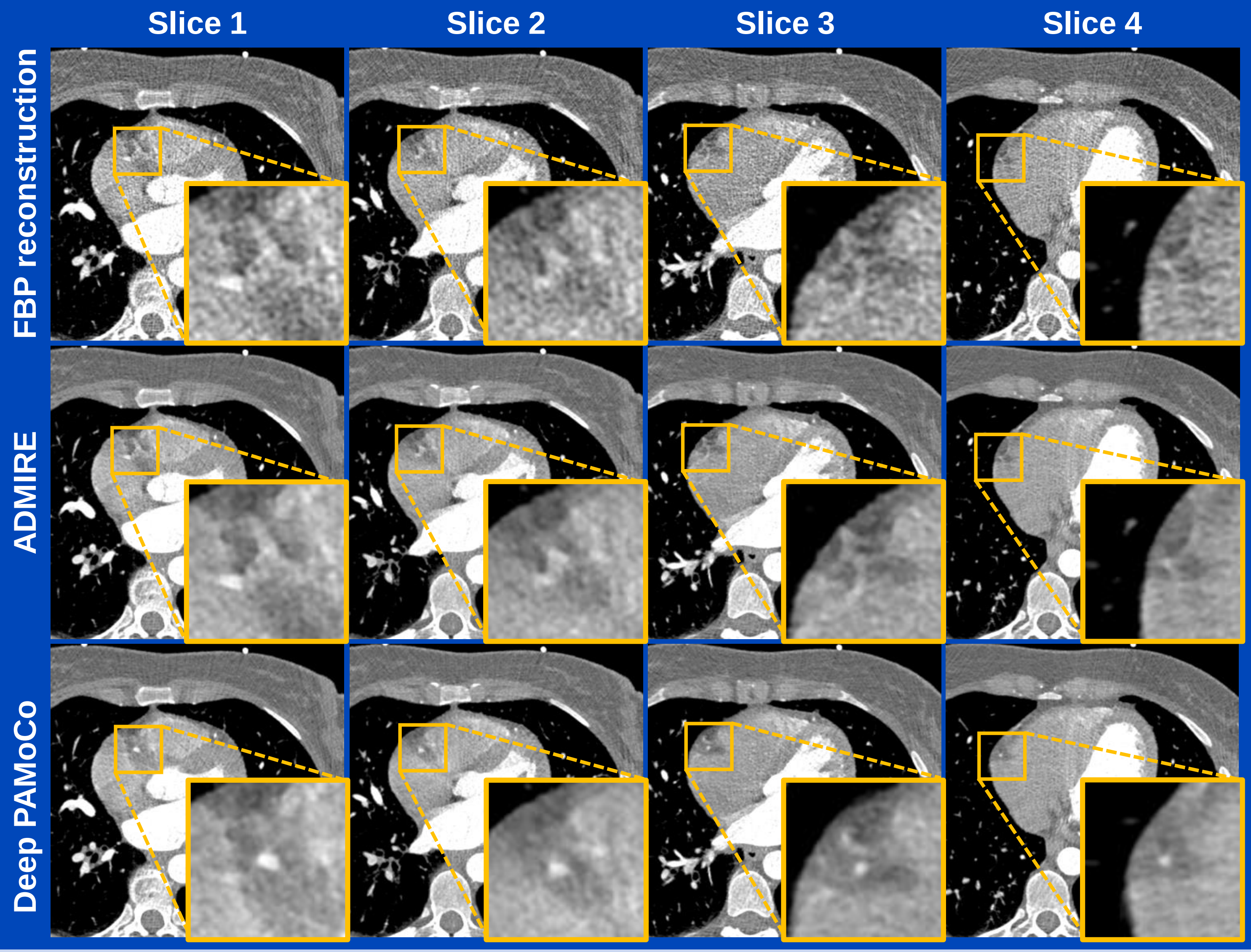

C = 0 HU, W = 1200 HU

Results

Measurements at a Siemens Somatom AS, patient 3

Slice 1 | Slice 2 | Slice 3 | Slice 4

FBP reconstruction
ADMIRE
Deep PAMoCo

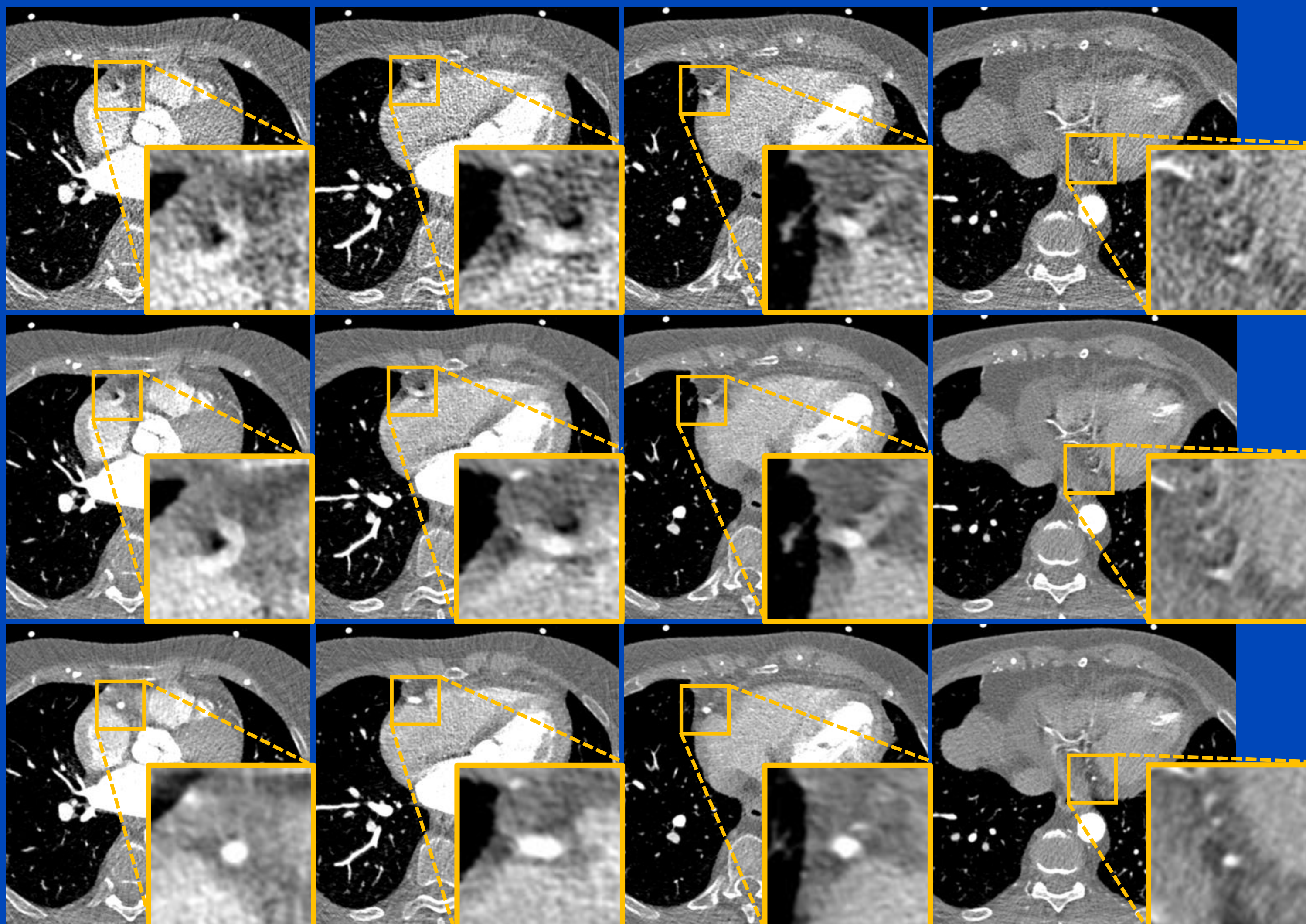

C = 0 HU, W = 1400 HU

dkfz.

Thank You!

This presentation will soon be available at www.dkfz.de/ct.

Job opportunities through DKFZ's international PhD or Postdoctoral Fellowship programs (marc.kachelriess@dkfz.de).

Parts of the reconstruction software were provided by RayConStruct® GmbH, Nürnberg, Germany.